Loughborough University

Thesis Access Form

Copy No 2 **Location**

Author VICENTE AZORIN PERIS.

Title OPTO-PHYSIOLOGICAL MODELLING OF PULSE OXIMETRY

Status of access ~~OPEN / RESTRICTED /~~ CONFIDENTIAL

Moratorium period: 2 years, ending 12 / 11 2010

Conditions of access proved by (CAPITALS): PROF. J. CHAMBERS

Director of Research (Signature) Jonathon Chambers

Department of ELECTRONIC & ELECTRICAL ENGINEERING

Author's Declaration: *I agree the following conditions:*

OPEN access work shall be made available (in the University and externally) and reproduced as necessary at the discretion of the University Librarian or Head of Department. It may also be copied by the British Library in microfilm or other form for supply to requesting libraries or individuals, subject to an indication of intended use for non-publishing purposes in the following form, placed on the copy and on any covering document or label.

*The statement itself shall apply to **ALL** copies:*

This copy has been supplied on the understanding that it is copyright material and that no quotation from the thesis may be published without proper acknowledgement.

Restricted/confidential work: All access and any photocopying shall be strictly subject to written permission from the University Head of Department and any external sponsor, if any.

Author's signature V. Azorin P. **Date** 12/05/09

Users declaration: for signature during any Moratorium period (Not Open work):
I undertake to uphold the above conditions:

Date	Name (CAPITALS)	Signature	Address

DEPARTMENT OF ELECTRONIC AND ELECTRICAL ENGINEERING
FACULTY OF ENGINEERING
LOUGHBOROUGH UNIVERSITY

OPTO-PHYSIOLOGICAL MODELLING OF PULSE OXIMETRY

BY

VICENTE AZORIN PERIS

A Doctoral Thesis
Submitted in partial fulfilment of the requirements for the award of
Doctor of Philoshophy of Loughborough University

October 2008

Supervisors: Dr. Sijung Hu & Professor Peter Smith
Department of Electronic and Electrical Engineering

For my mother and father

"I must study politics and war that my sons may have liberty to study mathematics and philosophy. My sons ought to study mathematics and philosophy, geography, natural history, naval architecture, navigation, commerce and agriculture in order to give their children a right to study painting, poetry, music, architecture, statuary, tapestry, and porcelain".

-- John Adams

CERTIFICATE OF ORIGINALITY

This is to certify that I, Vicente Azorin Peris, am responsible for the work submitted in this thesis, that the original work is my own except as specified in acknowledgements or in references, and that neither the thesis nor the original work contained therein has been submitted to this or any other institution for a higher degree.

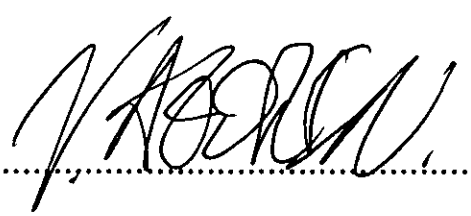

..... (Signed)

03/06/09 ..... (Date)

ABSTRACT

Since its conception decades ago, pulse oximetry—the non-invasive measurement of arterial blood oxygen saturation in real-time—has proven its worth by achieving and maintaining its rank as a compulsory standard of patient monitoring. However, the use of oversimplified models to describe and implement the technology has limited its applicability and has had its evolution at a near standstill for the past decade.

Currently available technology relies on empirical calibrations that consist of the correlation between simultaneous measurements from pulse oximeters and invasively acquired arterial blood samples from test subjects, mainly because the mathematical models underlying the technology are not sufficiently descriptive and accurate. Advances in knowledge of human tissue optical properties, computing power and sensing technology all contribute to a new realm of expansion for pulse oximetry modelling.

This research project aims to develop a methodology for improving opto-physiological models of pulse oximetry through the use of a validated Monte Carlo simulation platform for optical propagation in arbitrary geometries. The platform aims to arrive at a model that can predict the widest range of empirical outcomes while maintaining the highest possible level of accuracy. To this end, an empirical platform and a corresponding experimental protocol is developed towards an increasingly repeatable standard, thus providing an empirical output for validation of simulated data. Subsequently, the parameters and coefficients of the opto-physiological model at the core of the simulation platform are iterated until a high level of correlation is achieved in their outputs. This gives way to a new approach to the opto-physiological modelling of pulse oximetry.

ACKNOWLEDGMENTS

I want to express my love and appreciation for my parents, whose unwavering support during the past years has played a critical role in the completion of this research.

My sincere appreciation goes to all the members of the Photonics Engineering Group for their friendship and numerous enlightening discussions. It has been a privilege to be under the supervision of Dr. Sijung Hu, whose contributions have gone well beyond the scope of this work. I am immensely grateful for his undying support, patience and dedication throughout the duration of this research project. I am also grateful to Dr. Angelos Echiadis for his numerous contributions to this work and for countless lessons in engineering.

I would like to acknowledge the lasting support of my director of research, Dr. Sekharjit Datta. I also would like to thank Dr. Juanjo Perez and Dr. Jose Luis Gomez for their personal contributions during this work. I am grateful to Dr. Maria Sanchis and Paul Kayhan Piff for their love and support throughout the period of this project.

I acknowledge the full studentship support from the Department of Electronic and Electrical Engineering during the course of this project.

Finally, it gives me great pleasure to acknowledge my late supervisor, Professor Peter Smith. In the short time that I had the privilege of working with him, his example instilled in me an image of genuine respect and leadership, and his memory is one that I will always call upon for guidance.

TABLE OF CONTENTS

SECTION 2 METHODOLOGY

SECTION 1 INTRODUCTION

1 SUMMARY OF RESEARCH

Since its conception decades ago, pulse oximetry—the non-invasive measurement of arterial blood oxygen saturation in real-time—has proven its worth by achieving and maintaining its rank as a compulsory standard of patient monitoring. However, the use of oversimplified models to describe and implement the technology has limited its applicability and has had its evolution at a near standstill for some time. Currently available implementations of the technology rely on empirical calibrations that consist of the correlation between simultaneous measurements from pulse oximeters and invasively acquired arterial blood samples from test subjects, a process that would be unnecessary if the mathematical models underlying the technology were sufficiently descriptive and accurate. Advances in knowledge of human tissue optical properties, computing power and sensing technology all contribute to a new realm of expansion for pulse oximetry modelling.

1.1 BACKGROUND

Photoplethysmography (PPG) is an optical biomonitoring technique that non-invasively measures arterial pulsations *in-vivo*. Its ease of use and convenience make it an attractive area of research in the biomedical and clinical community. Among its applications, pulse oximetry—the determination of arterial oxygen saturation—is the most widespread thanks to its ability to alert the clinician of the presence of hypoxemia in real-time. Pulse oximetry has become a standard of patient monitoring during anaesthesia, in recovery rooms and under intensive care.

However, oximeters have a number of factors that lead to inaccurate readings and limit their applicability. As such, these are practable areas of research when attempting to increase the reliability and applicability of the technology. The success of solutions to engineering issues of pulse oximetry depends heavily on the validity of the assumptions used to correlate the PPG signals. The adverse effects of these issues are generally quantified according to the sensitivity and specificity of oximeters under the relevant scenarios, often overlooking the mechanisms leading to such inaccuracies due to the inherent complexity and variability of the physical mechanisms involved. With the increasing availability and accuracy of tissue optical properties in literature, the use of numerical solutions of light propagation in human tissue are providing increasingly valuable insights into such mechanisms.

This thesis presents an engineering platform that has been created to provide a more rigorous description and consequently, a more robust and applicable implementation of pulse oximetry. The platform consists of a software and a hardware element. The software element performs numerical simulations of optical propagation through 3D models of human measuring sites and subsequent analysis and extraction of parameters from its output data, and the hardware element consists of a series of light source and sensor arrangements that provide empirical data corresponding to the simulated output. The concept behind this platform is that, as the assumptions and parameters of the simulation approach those occurring in the corresponding real-life situation, the outputs of both elements of the platform increasingly correlate. As this occurs, the validity of such simulations and hence their ability to describe the real mechanisms tends towards the ideal theoretical case of a virtual model that can

emulate the real-life process with absolute precision, and thus elucidate the complex relations between the mechanisms involved.

1.2 AIMS AND OBJECTIVES

An accurate opto-physiological simulation should allow prediction of the response of a pulse oximeter under different circumstances, such as light source wavelengths, blood hematocrit, or geometrical properties of the measuring site. This would reduce the need for clinical studies for validation and calibration of novel implementations of pulse oximetry and could potentially bypass the limitations of these studies.

The aim of this research work is ***to provide a comprehensive description of the mechanisms involved in pulse oximetry, in order to yield opto-physiological models of pulse oximetry that are more accurate and descriptive than currently existing ones.***

From these aims, the following objectives are inferred in the context of this thesis:

1) ***To provide the background context of pulse oximetry, focusing on a biomedical engineering perspective of the technology.*** For photoplethysmography (PPG) and pulse oximetry, the principles of operation, applicability, engineering issues and limitations, along with common research areas and approaches to current limitations are recounted (**Chapter 2**).

2) ***To illustrate the central role of opto-physiological models and develop an improved model for pulse oximetry.*** Relevant concepts of optics and physiology, specifically those which pertain to human tissue optics and the circulatory system are examined and put into context. The strengths and weaknesses of the currently in use Beer-Lambert model for pulse oximetry and the mathematically rigorous Radiative Transport Theorem are detailed. Both models are analysed in order to develop a proprietary opto-physiological model for pulse oximetry (**Chapter 3**).

3) ***To present the technical details of the experimental setup and methodology that was developed and employed for this investigation.*** The structure and dataflow of the Monte Carlo (MC) simulation platform for light propagation through arbitrary geometries is detailed along with all output data processing algorithms. Specifications of all hardware and control software used for generation of empirical data is provided, specifically for the 1D photodiode sensor array and the 2D CMOS camera solutions. Additionally, all empirical data processing algorithms are detailed (**Chapter 4**).

4) ***To present the experimental results of the investigation and to analyse these results with respect to the applicability of the novel opto-physiological model.*** The protocols used for both simulation and validation experiments, specifically, the choice of tissue optical properties and assumptions for simulation and the choice of light sources and detection schemes for validation, are detailed. The results to all the experiments of this investigation, with emphasis on comparative results for simulation and validation experiments, are distilled and presented with an in-depth discussion of their accuracy and significance (**Chapter 5**).

5) ***To elucidate the research trajectories and recommendations that the results and engineering issues encountered in this investigation justifies.*** The experimental results are discussed in-depth, and suggestions are made for future work with respect to the Monte Carlo simulation and empirical validation elements of the platform, as well as potential experiments relevant to the research (**Chapter 6**).

1.3 RELEVANT PUBLICATIONS

The following articles related to this work have been published:

Azorin-Peris V, Hu S, Smith PR, "A Monte Carlo model for the optical modelling of pulse oximetry", Progress in biomedical optics and imaging, Vol. 8, 23, 2007.

Azorin-Peris V, Hu S, "Validation of a Monte Carlo platform for the optical modelling of pulse oximetry", J. Phys.: Conf. Ser., 85, 012027, 2007.

Other publications related to work carried out in relevant areas of research are listed below:

Xin S, Hu, S, Crabtree V, Zheng J, Azorin-Peris V, Echiadis A, Smith PR, "Investigation of blood pulse PPG signal regulation on toe effect of body posture and lower limb height", Journal of Zheijiang University – Science A, Vol 8, 6, 916-920, 2007.

Chouliaras, V., Hu., S., Azorin-Peris, V., Echiadis, A., Summers, R., Zheng, J., King, I., "Real-time VLSI architecture for bio-medical monitoring", Pro. ITAB 2008, Shenzhen, China, 2008.

Zheng, J., Hu., S., Azorin-Peris, V., Echiadis, A., Chouliaras, V., Summers, R., "Remote simultaneous dual wavelength imaging photoplethysmography: a further step towards 3-D mapping of skin blood microcirculation", Appl. Phys. Lett. 0003-6951, Proc. of SPIE Vol. 6850 68500S-1, BiOS, Photonics West, San Jose, USA 2008

A patent is currently being prepared with Loughborough University IP Office

Azorin-Peris, V., Hu, S., " Opto-physiological Modelling"

2 RESEARCH IN PULSE OXIMETRY

Photoplethysmography (PPG) is an optical biomonitoring technique that non-invasively measures arterial blood volume changes *in-vivo*. Among its applications, pulse oximetry—the determination of arterial oxygen saturation—is the most widespread thanks to its ability to alert clinicians of the presence of hypoxemia in real-time. Pulse oximetry has become a standard of patient monitoring during anaesthesia, in recovery rooms and under intensive care. However, oximeters have a number of factors that lead to inaccurate readings and limit their applicability. As such, these are potential areas of research when attempting to increase the reliability and applicability of the technology.

2.1 PHOTOPLETHYSMOGRAPHY AND PULSE OXIMETRY

Oxygen is a vital element in the metabolism of cells in living organisms, and its delivery is the primary task of the cardiovascular system. The capacity to assess the performance of the cardiovascular system in terms of oxygen delivery is invaluable to clinicians, and pulse oximetry is the available tool for this assessment.

Pulse oximetry is an application of a technology called Photoplethysmography (PPG), which is an electro-optic technique used to measure the volume changes that occur in the human body due to the pulsatile nature of the circulatory system. PPG was introduced almost simultaneously by Hertzman in the United States and Matthes and Hauss in Germany in 1938[1] but Hertzman was the first to use the term 'photoplethysmograph'[2] and is a pioneer in this area, having published several early papers on the utility of this technique. Pulse oximeters were first developed around the same time[3,4], most of which were intended for military use[5,6], but none of these proved to be of any practical use. It was not until 1972 that Takuo Aoyagi conceived the principle on which the first practical pulse oximeter was based[7].

The human body cannot survive for more than a few minutes without oxygen intake, as opposed to the days or weeks that it can survive without water or food intake. The capacity to provide real-time knowledge of arterial oxygen saturation makes pulse oximetry effective at giving an early warning for hypoxia[8], which is the most common cause of morbidity and mortality during and after anaesthesia[9]. By virtue of this ability, it has become a standard of patient monitoring during anaesthesia, in recovery rooms and under intensive care[10] and has stood its ground as the single most important advance in patient monitoring since its arrival three decades ago.

2.2 PRINCIPLES OF PHOTOPLETHYSMOGRAPHY

Photoplethysmography is the core technology on which pulse oximetry is based. In order to understand the principles of photoplethysmography, a basic knowledge of the human circulatory system and of the optical properties of human tissue is required.

2.2.1 Background Physiology

The main functions of the human circulatory system are to deliver oxygen and nutrients to all the cells in the body and to remove waste products from the cells, although it is also responsible for the transportation of hormones and for regulation of body temperature, and it plays a part in the immune system of the body. The human circulatory system is essentially composed of the lungs, the heart, and the venous and arterial trees. The closed path of blood circulation is as follows: the heart pumps blood out of the right ventricle into the lungs via the pulmonary arteries. In the lungs, carbon dioxide is released from the blood and replaced by oxygen. Oxygenated blood from the lungs gathers in the left atrium of the heart and passes to the left ventricle. The left ventricle pumps this blood out to the whole body via the arteries. After the oxygen in the blood is released into the tissue and organs of the body and carbon dioxide is collected, the blood returns to the right atrium via the veins, where it passes into the right ventricle and the cycle repeats. Blood circulation as described above covers two beats of the heart; during systole, the heart pumps blood both to the body and to the lungs, and during diastole, both ventricles fill with blood as shown in Figure 1.1.

The arteries are the thick walled vessels that withstand the highest pressures and largest pressure oscillations in the vascular tree. Arteries branch into arterioles and then into capillaries, thus reducing blood pressure, pressure oscillation and velocity due to an increase in corresponding cross-sectional area in the capillaries, as detailed in Figure 1.3. Blood leaving the capillaries converges into venules and then veins. The latter are large, thin walled vessels, where blood travels with the aid of gravitational pressure. Another effect exists, called anastomosis[11], in which arterial blood is shunted directly to the venous system without traversing capillaries. PPG measures changes in blood volume, therefore the pulsatile nature of arterial blood flow is inherently important to the technology.

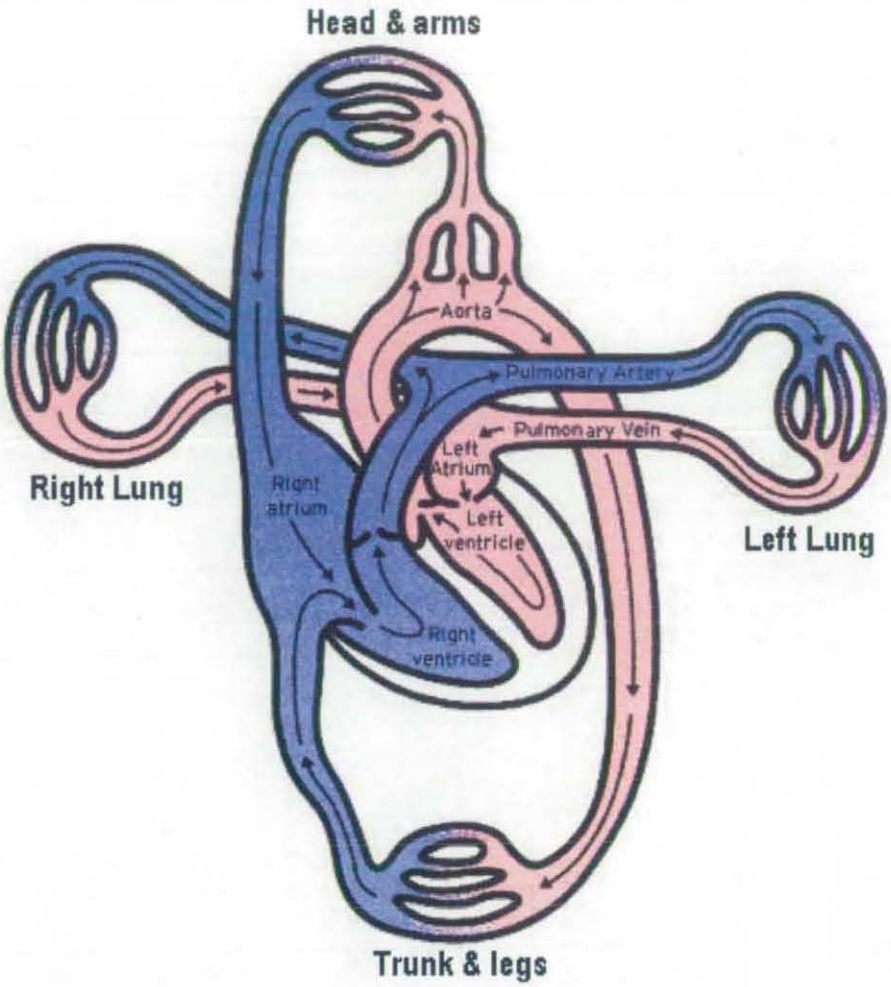

Figure 1.1 – Simplified diagram of circulatory system (image courtesy of www.hearttransplant.co.uk).

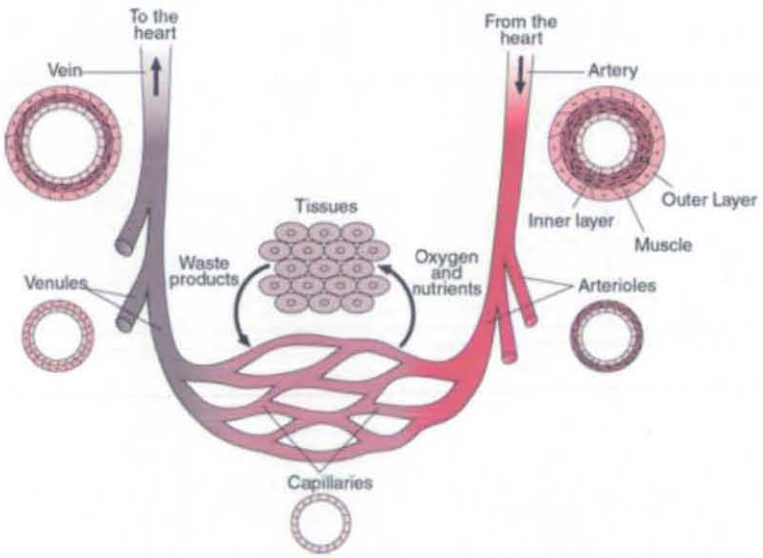

Figure 1.2 – Structure of the vascular tree, with relative vessel wall thicknesses and capillary-tissue fluid exchange (image courtesy of www.merck.com).

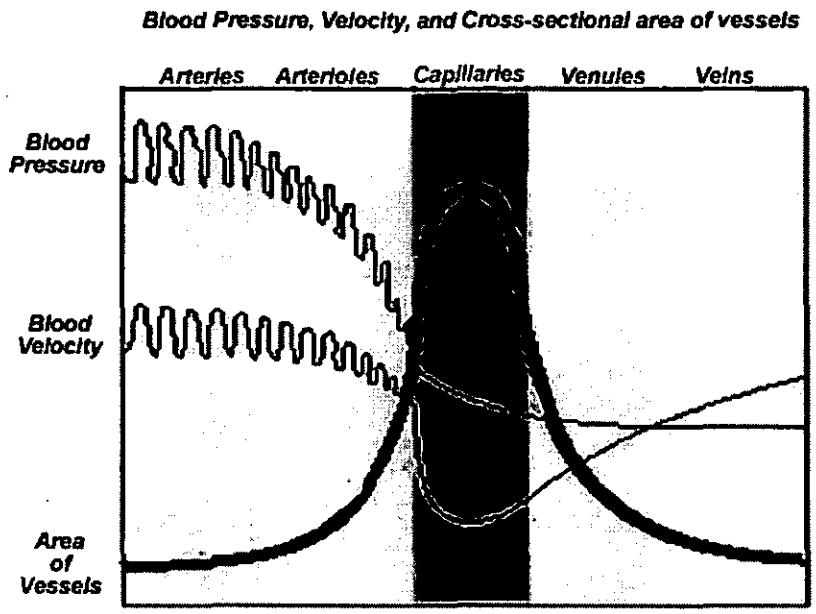

Figure 1.3 – Comparative cross-sectional analysis of scales in the cardiovascular tree (image courtesy of www.coolschool.ca).

An exchange of oxygen, nutrients and waste products takes place between the blood and adjacent tissues as the blood traverses the capillaries, where its reduced speed allows this to occur effectively. All cells in the body require this exchange; therefore, all tissue in the human body is perfused with blood.

Out of all the organs of the body that are fed by the cardiovascular system, skin has a high relevance in non-invasive monitoring techniques as its surface is the site onto which sensing probes are placed. Consequently, its anatomical and physiological characteristics always play a role in these technologies. Human skin is essentially divided into three layers, namely, epidermis, dermis and subcutaneous fat. The epidermis is the outermost layer, in which the skin pigment melanin is produced by cells called melanocytes. This pigment is responsible for the protection of the skin against harmful radiation by means of absorption. The dermis houses blood vessels which are largely categorised as two vascular beds, namely the superficial and deep vascular plexa. Subcutaneous tissue is a layer of fat which houses lager blood vessels, nerves and connective tissue and it plays a big role in the regulation of skin and body temperature. A simplified diagram of the skin can be seen in Figure 1.4.

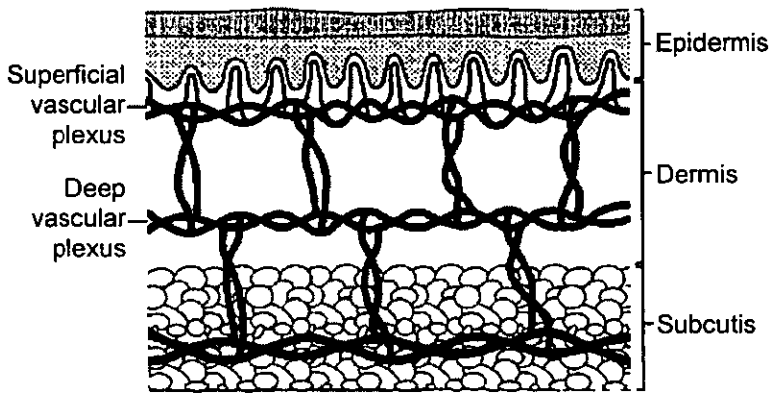

Figure 1.4 – Structure of the vascular tree, with relative vessel wall thicknesses and capillary-tissue fluid exchange (image courtesy of herkules.oulu.fi).

2.2.2 Tissue Optics

As an optical bio-monitoring technique, PPG requires a light source and detector to function and relies on the optical properties of biological tissue. It can be performed in transmission mode, where the light source and detector are facing each other and are usually placed on opposite sides of the tissue under inspection, and in reflection mode, where the light source and detector are facing the same direction and are usually adjacent. Transmission mode only works in well perfused areas where trans-illumination of the tissue bed is possible, such as the fingers, lips, or earlobes. Reflection mode relies on backscattered light returning to the skin surface, which allows it to be used anywhere in the body but limits the quality of detected signals.

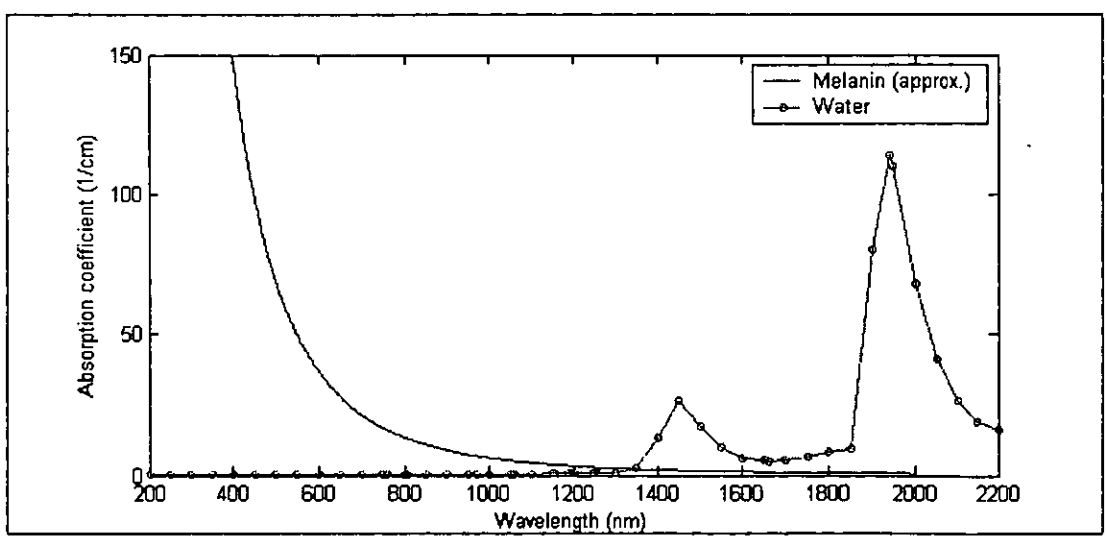

Figure 1.5 - Absorption spectra of water[12] and melanin[13].

Ideally for PPG, human blood would absorb greatly and all other tissue would absorb weakly as this would allow for accurate monitoring of blood volume changes with low light source intensity. Human tissue is mainly composed of water, and human skin contains the pigment melanin. It can be seen from Figure 1.5 that light is increasingly absorbed by melanin towards the ultra-violet band and greatly absorbed by water in the microwave band. This limits practical wavelengths of a PPG light source roughly to the visible spectrum[14].

Wavelength selection in PPG is limited by tissue absorption, but the technique itself is only made possible by the dynamic optical properties of arterial blood. The arteries expand and tissues fill with blood during systole, thus increasing the amount of blood that absorbs light. Assuming that the absorption characteristics of skin, bone and tissue remain constant, the resultant dynamic portion of the detected PPG signal can be solely attributed to pulsatile arterial blood, shown in Figure 1.6, and any quasi-static portions of the signal can be attributed to changes in non-pulsatile arterial and venous blood due to breathing or otherwise. PPG works under this premise[15].

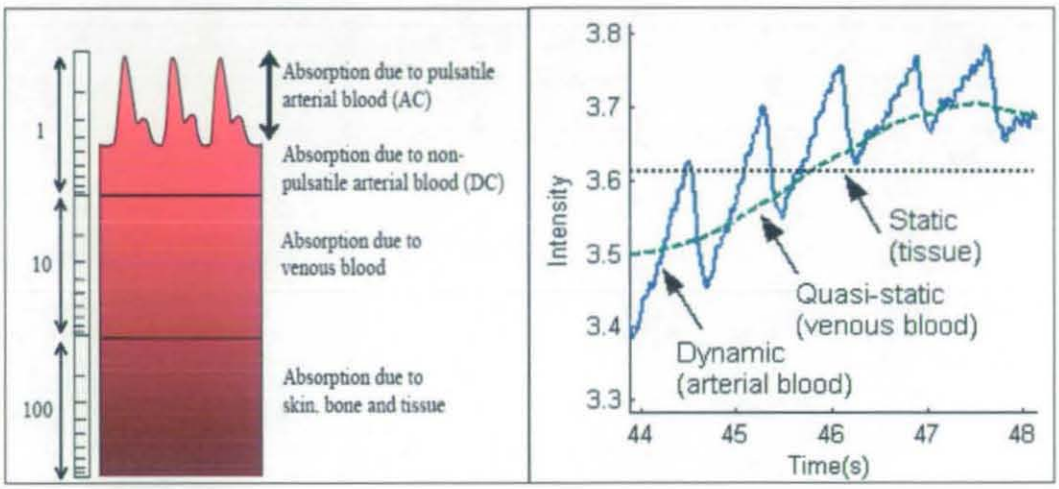

Figure 1.6 – Relative absorptions of blood and tissue (left), and components of a raw PPG signal (right).

2.3 PRINCIPLES OF PULSE OXIMETRY

Oxygen saturation (SaO_2) can be theoretically understood as the percentage of total haemoglobin in the blood that is oxyhaemoglobin:

$$SaO_2 = HbO_2 / (HbO_2 + Hb) * 100 \qquad [2.1]$$

Pulse oximetry is the use of PPG for *in vivo* monitoring of oxygen saturation in haemoglobin. It uses PPG signals at two different wavelengths to deduce the ratio of oxygenated to reduced haemoglobin in the blood. The fundamental principle of this process can be understood when the relative absorptions of deoxyhaemoglobin and oxyhaemoglobin as shown in Figure 1.7 are considered. Red light (600-700nm) is known to be absorbed greatly by reduced haemoglobin and poorly by oxyhaemoglobin. There exists an isobestic point at wavelengths of about 800 nm, where both species of haemoglobin absorb in equal quantities, and oxyhaemoglobin absorbs more light than reduced haemoglobin as the infrared band is approached (850-950nm). The ratio of absorptions due to arterial blood at two wavelengths carefully selected from either side of the isobestic point can thus be linked to a corresponding level of blood oxygen saturation. Conventionally selected wavelengths are in the 660 and 900 nm bands[16], where a contrast in relative absorptions between the haemoglobins can be appreciated.

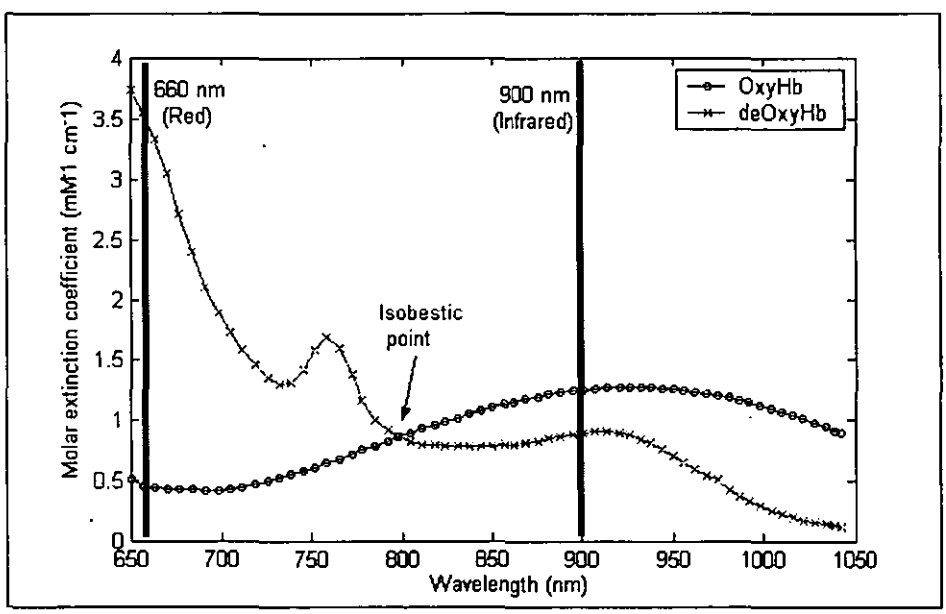

Figure 1.7 – Relative absorptions of blood and tissue[17].

2.3.1 The Beer-Lambert Model

The human tissue bed is composed of tissue, bone, blood vessels, fluids, skin and blood. It is far from being optically homogeneous and thus exhibits significant scattering of light. Some early attempts at practical pulse oximetry were based solely on Beer-Lambert's law[18], which relates light transmitted through a homogeneous medium of a known optical path length and absorbance to the concentration of the medium. Nevertheless, Beer-Lambert's Law of light absorption is successfully used to provide a model that aids physical understanding of pulse oximetry by assuming homogeneity of the human tissue bed[19]. The law may be written as the equation:

$$I = I_0 \exp(-\mu_{eff}(\lambda) r) \qquad [2.2]$$

where I is the amount of light that gets transmitted from a collimated and monochromatic light source of intensity I_0, through a solution of a component with an effective absorbance μ_{eff} and a path length r. Thus, if path length is constant, light transmitted through a solution will decay exponentially as a function of concentration.

2.3.2 Practical Pulse Oximetry

Pulse oximetry can be implemented in several ways, as the process involved can be modified in many ways to adjust its mode of operation. This section describes the practical implementation used in this investigation, which demonstrates the fundamental process involved in modern pulse oximeters. The device discerns two signals, $I(t,\lambda_1)$ and $I(t,\lambda_2)$, which can be described as,

$$\begin{aligned} I(t,\lambda_1) &= A\mu_{total}(t,\lambda_1) \\ I(t,\lambda_2) &= B\mu_{total}(t,\lambda_2) \end{aligned} \qquad [2.3]$$

where A and B are constants proportional to the red and infrared light source intensities and μ_{total} is the wavelength dependent and time-varying absorption coefficient of the whole tissue bed. These signals are separated into their static (DC) and dynamic (AC) components by means of analogue filters:

$$I(t,\lambda_1) = A\mu_{tissue}(\lambda_1) + A\mu_{blood}(\lambda_1)d(t)$$
$$I(t,\lambda_2) = B\mu_{tissue}(\lambda_2) + B\mu_{blood}(\lambda_2)d(t) \quad [2.4]$$

The peak-to-peak separations of the AC components are determined and smoothed, yielding a pair of quasi-static signals $\beta_{pp}(t,\lambda_1)$, $\beta_{pp}(t,\lambda_2)$, which take the place of the AC components in subsequent steps.

$$I(t,\lambda_1) = A\mu_{tissue}(\lambda_1) + A\beta_{pp}(t,\lambda_1)$$
$$I(t,\lambda_2) = B\mu_{tissue}(\lambda_2) + B\beta_{pp}(t,\lambda_2) \quad [2.5]$$

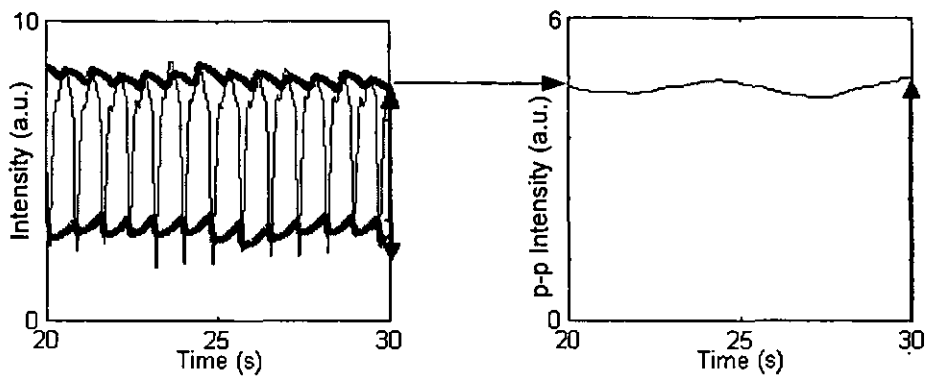

Figure 1.8 – Positive and negative envelope detection on AC PPG signal (left) and determination of peak-to-peak AC signal intensity (right).

By taking the ratio of the dynamic to the static components of each signal, any dependence of the absorption coefficients on light source intensity is removed. The ratio of the normalised signals is then taken, giving the *ratio of ratios*, *R*:

$$R(t) = \frac{\left(\frac{\beta_{pp}(t,\lambda_1)}{\mu_{tissue}(\lambda_1)}\right)}{\left(\frac{\beta_{pp}(t,\lambda_2)}{\mu_{tissue}(\lambda_2)}\right)} \quad [2.6]$$

The resultant value of *R(t)* (continuous monitoring) is then correlated with a corresponding value of oxygen saturation from a set of empirically derived constants.

2.3.3 Calibration

All of the above absorption coefficients, and consequently the peak-to-peak absorptions in equation 2.6 are subject-specific, that is, they will vary from person to person. However, the robustness of the ratio of ratios can be demonstrated through analysis of the equation from the perspective of the Beer-Lambert model for pulse oximetry. Assuming that the light sources for each wavelength provide an identical trans-illumination of the tissue bed, differences in absorptions between wavelengths can only be due to the wavelength dependence of the specific absorbances of the components in the tissue bed. A change in tissue density or tissue (static) optical path length will proportionally change the light transmitted through the tissue bed, thus proportionally changing both static and dynamic components of R. A change in pulsatile arterial flexion will proportionally change the difference in the absorption of blood from systole to diastole, thus proportionally changing the dynamic components of R. R will therefore maintain its value from subject to subject as long as the specific absorption spectra of their tissue composition are sufficiently similar. Under these conditions, R can only change due to a change in the dynamic components with respect to each other, brought about by a change in the proportion of oxygenated to reduced haemoglobin in the blood.

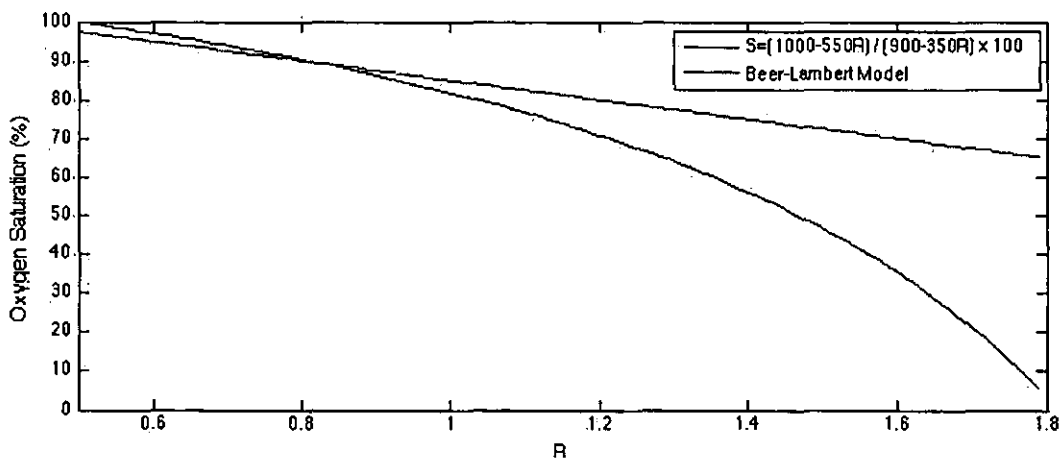

Fig. 1.9 – Empirical calibration (bilinear) vs. Beer-Lambert model (using absorbances from [17]).

In practice, manufacturers of pulse oximeters perform an empirical pre-calibration[20,21], whereby oxygen saturation measurements taken directly from blood are correlated with pulse oximeter readings using the variations of the relationship

$$SaO_2 = A - B * R \qquad [2.7]$$

where A and B are the empirically derived constants that define the relationship between the ratio of ratios R and SaO_2. These constants essentially represent a set of values for the static and dynamic absorption coefficients of Equation 2.4, which means that a separate calibration is necessary with any change in light source specifications or source-detector arrangement.

2.4 CURRENT RESEARCH IN PULSE OXIMETRY

The principle of operation for current pulse oximeters is commonly described using the Beer-Lambert model, where the measuring site is treated as a blood-filled cuvette with no scattering effects and the light sources are assumed to be monochromatic. The highly scattering nature of human tissue clearly contradicts these assumptions. However, the widespread use of this model illustrates the common simplification process inherent in the area.

The success of solutions to engineering issues of pulse oximetry depends heavily on the validity of the assumptions used to correlate the PPG signals. The adverse effects of these issues are generally quantified according to the sensitivity and specificity of oximeters under the relevant scenarios, often overlooking the mechanisms leading to such inaccuracies due to the inherent complexity and variability of the physical mechanisms involved. With the increasing availability and accuracy of tissue optical properties in literature, the use of numerical solutions of light propagation in human tissue are providing increasingly valuable insights into such mechanisms.

2.4.1 Limitations of Pulse Oximetry

The ideal pulse oximeter would be a device that could make an accurate measurement of oxygen saturation in any specific part of the body and for any subject regardless of physiology, state of health, and condition under which the measurement is made. The

numerous limitations that exist in current pulse oximeters imply numerous areas of research. The most obvious of these arises from the need to calibrate devices with test subjects breathing a range of air mixtures to yield lower oxygen saturations. Apart from the limitation posed by the need to calibrate, safety regulations enforce a minimum oxygen saturation that a subject can be exposed to, thus impeding calibration for low saturation values[22].

Signal distortion is known to be the main cause of false alarm conditions, especially in the case of neonates[23]. Pulse oximeters are prone to artefact (signal distortion) caused by ambient light and motion of the subject[24]. Ambient artefact is not a problem in theory since additional sampling periods can be used for ambient subtraction, although some cases have been reported in which the severity of ambient light was an issue[25]. Motion artefact however, is a prevalent problem as the majority of low SpO_2 alarms generated by the pulse oximeter are false[26] and some potential applications of the technology are not possible due to the severity of its effects[27]. Although motion artefact can be easily detected through signal processing[28], commercial pulse oximeters tend to ignore artefact ridden portions of signals to a greater or lesser extent[29], thus making a compromise between accuracy of the device in the detection of hypoxemia and likelihood of false alarm conditions[26].

Most commercially available pulse oximeters use only two wavelengths, an arrangement that would be sufficient if only haemoglobin and oxyhaemoglobin were present in the blood. The presence of other species of haemoglobin such as carboxyhaemoglobin and methaemoglobin in the blood has been proven to lead to measurement errors[30]. Heavy skin pigmentation is also known to be the source of inaccuracies. Any such assumption that aims to normalise the anatomy for a greater simplicity of implementation is an approximation and can thus lead to errors.

It is through a theoretical understanding of the limitations of pulse oximetry that possible ways to overcome these are elucidated. Current research aims to improve the accuracy, robustness and applicability of pulse oximetry in accordance to its known limitations.

2.4.2 Research in Pulse Oximetry

As a highly technical area of research, pulse oximetry requires an in-depth understanding of the array of theoretical principles involved. *In-vitro* and *ex-vivo* research consists of simulating conditions found in pulse oximetry through the use of synthetic physical models or excised tissue samples and performing empirical measurements on these. The aim of this type of investigation is to acquire knowledge regarding the properties of relevant aspects, such as the optical properties of tissue[31,32], or physiological phenomena[33]. In contrast, *in-vivo* experiments consist of empirical measurements performed directly on live subjects for comparison with other experimental results[34]. Extensive signal processing-based research has been performed for the purpose of finding ways to extract relevant information from PPG signals. This kind of research helps not only in determining what properties of the circulatory system are discernible from these signals[35,36], but can also lead to simpler[37,38] and more robust[39] implementations of pulse oximetry. Clinical research in pulse oximetry consists of determining the performance and applicability of a system with a novel probe[40,41], electronic system[42] or signal processing methodology[43] by means of statistical comparisons with the gold standard device of that system, and it is the final step required to validate a practical pulse oximeter.

The development of a pulse oximetry system initially requires the creation of descriptive mathematical models which incorporate knowledge of the factors involved, such as tissue optical properties, observed physiological phenomena, or engineering issues[24] through the use of first principles. In essence, the difficulty of resolving the limitations to pulse oximetry lies in the models underlying solutions to these. Testing of such mathematical models often consists of developing a geometric model based on knowledge of the properties of relevant tissues, and simulating the light-tissue interaction using numerical solutions to analytical expressions[16], or through the use of Monte Carlo simulations[44]. As stated in previous sections, the Beer-Lambert model that is often used to make assumptions in pulse oximetry leads to treatment of blood and tissue bed as homogeneous, when in fact they cause vaguely defined scattering. Other investigations explore the use of diffusion-based models[45,46], which exhibit a marked increase in both accuracy and complexity. Models that are numerically resolved using Monte Carlo simulation are renowned for

their computational cost but allow for virtually any level of desired complexity[47]. Such a model can then be implemented in hardware by prototyping a pulse oximeter whose probes and electronic systems treat the relevant physiological signals in accordance to the model.

2.4.3 Research Direction

This research project consists of the development of a proprietary opto-physiological model of pulse oximetry, its application through the use of Monte Carlo ray tracing on a multi-layered model of arbitrary geometry, and validation via subsequent correlation with corresponding empirical measurements.

The platform presented in this project can model virtually any set of conditions and effects depending on the settings used in simulation and the construction of the empirical measurement platform. It is possible to define a measure in the assessment of validation achieved in such a platform. For lower degrees of validation, the platform would provide qualitative information with respect to the arrangement being scrutinised. This would include information such as combinations of light source and sensor positions at which the quality of captured signals is optimum and qualitative differences in the response when using different light sources and detectors.

In contrast, higher degrees of validation would mean that the platform can make quantitative predictions of the signals to be expected from the equivalent physical arrangement. For instance, the signals expected from arbitrary measuring sites, the effects of motion artefact to these output signals, and the response to different degrees of perfusion and oxygenation could all be predicted, given a sufficient degree of validation.

This research project is directed towards developing a methodology to achieve progressively higher degrees of validation for a novel model of pulse oximetry technology.

This chapter has provided a background for photoplethysmography and pulse oximetry, specifically their principles of operation, applicability, engineering issues and limitations. Additionally, common research areas and approaches to the known limitations of these techniques have been recounted. Finally, a general description of the direction and approach of this research project has been provided.

SECTION 2 METHODOLOGY

3 ENGINEERING MODEL

The objective of this chapter is to arrive at an opto-physiological model of the human finger that is practicable both in simulation and in empirical validation. This inevitably requires a degree of simplification brought about by a series of assumptions pertaining to the macroscopic interaction of light with human tissue. The objective of this chapter is to arrive at an opto-physiological model of the human finger that is suitable both in simulation and in empirical validation. This inevitably requires a degree of simplification brought about by a series of assumptions pertaining to the macroscopic interaction of light with human tissue. The chapter explains the optical and physiological phenomena that govern diffuse optical bio-monitoring techniques, revisits some of the relevant engineering models used for *in-vivo* optical propagation, and describes the model relevant to this investigation.

3.1 PRINCIPLES OF TISSUE OPTICS

Optical bio-monitoring modalities can be described in general terms as systems that modify a specific light intensity, where the transfer function is determined by a number of anatomical and physiological parameters. In practice, the immensity of data that would accurately define a measuring site, the inherently dynamic nature of such a site and the variability found between different sites and subjects, place such modalities in a balance between accuracy and applicability. Consequently, a model for such a system requires a significant degree of simplification. A number of optical phenomena govern the behaviour of light propagating through an optically dense medium such as human skin. These are considered at a macroscopic scale and are explained in the context of their relative contributions to the effective output intensity in trans-illuminated tissue.

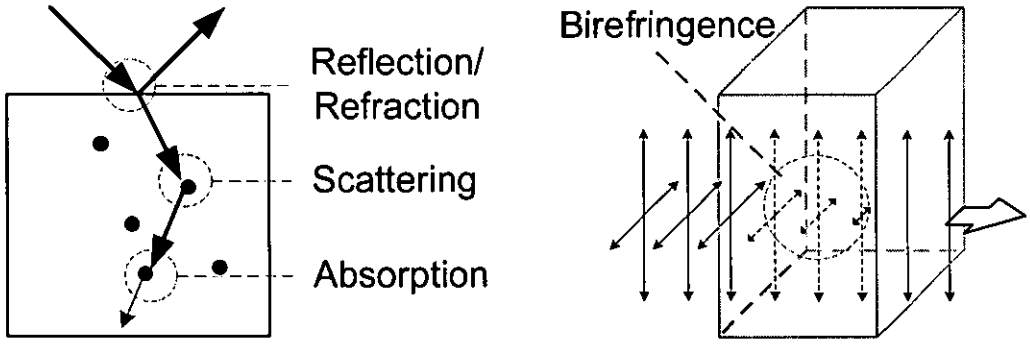

Figure 3.1 - Optical phenomena affecting studies in tissue optics

3.1.1 Refraction

Refraction occurs under any circumstance where propagating light encounters a change in refractive index. Surface effects due to index mismatched macroscopic boundaries such as those between skin layers are one such occurrence. Churmakov et. al.[48] concluded that the spatial photon sensitivity profile under normal conditions was nearly identical to that achieved when disregarding total internal reflection at the boundary between a highly scattering and absorbing medium and vacuum, thus proving the relative insignificance of this effect. Furthermore, the refractive indices of tissue types at a macroscopic scale are typically close to 1.4 with little variation,

yielding inter-tissue boundary effects which are disregarded in most photon transport models[49].

3.1.2 Scattering

Refractive index mismatches within tissues also exist at a microscopic scale, where collagen fibres, blood vessels, cell membranes and organelles etc. submit light to refractive effects[49]. In practice, most models approximate these effects through the use of the experimentally determined scattering coefficient μ_s and the anisotropy factor g to describe tissue types at a macroscopic scale. Here, μ_s (mm^{-1}) is the mean path length between scattering events and g is the mean cosine angle of deflection upon scattering. Numerous studies employing simplified optical models for skin have yielded reliable results employing isotropic scattering[50]. The diffusion of light through a medium has a direct effect on its irradiance distribution, thus making scattering a dominant effect in such studies.

3.1.3 Absorption

Absorption is an effect that is explained at an atomic scale as the conversion of photons into thermal energy upon collision with atoms. More specifically, this effect is most likely to occur when the energy of a photon (determined by its frequency) coincides with one of the excited states of the atom it is colliding with. Its direct relationship to the effective transmission of light through a medium makes this a key effect in the present study.

Blood is responsible for most of the fluid exchange taking place in the human body, and as such, represents its dynamic nature in terms of tissue optics. The applicability of PPG relies on the relative differences in the absorption of light from different haemoglobin species in the blood, which include oxyhaemoglobin, carboxyhaemoglobin, methaemoglobin and deoxyhaemoglobin. Cardiovascular pulsations lead to an oscillation in tissue absorption due to a variation in blood perfusion and optical path length. Consequently, the quality of PPG signals relies on the fact that blood is a high absorber in relation to other tissues. Relevant effects

include those due to the presence of drugs and dyes[14], or those due to red blood cells changing their shape and orientation with the physiologically induced changes in blood flow velocity[51].

3.1.4 Birefringence

Birefringence is the property of a material whose refractive index is a function of both the polarisation and the orientation of incident light, and it is commonly found in biological tissues due to their fibrous nature at a microscopic scale. Standard photosensitive devices are generally assumed to have negligible polarisation sensitivity when detecting normally incident radiation, but they do present increasing sensitivity as the angle of incidence is increased[52]. However, when using a randomly polarised light source, the nonlinearity of a detector under randomly incident light originating from a randomly polarised light source such as a LED can be considered negligible. Evidence also suggests that light incident on tissue rapidly becomes depolarised[53], effectively rendering coherent light sources such as resonant cavity LEDs and lasers equivalent to standard LEDs in the absence of polarisation optics, given that the incident intensity distributions on the probed tissue are equivalent.

In general terms, polarisation-sensitive detection methods make use of polarising materials to measure the effects of birefringence on the transmission of light in a sample. For instance, polarisation-sensitive optical coherence tomography can provide additional structural information on biological tissue, which its polarisation-insensitive counterpart cannot[54]. It is reasonable to disregard polarisation as a contributing effect in light propagation studies that do not specifically seek characterisation of birefringence effects.

3.2 MATHEMATICAL MODELS

In this section we introduce mathematical models used to describe the propagation of light through human tissue. It is possible to describe the propagation of light in tissue from the wave perspective by using multiple scattering electromagnetic theory[55]. Tissue can be considered a random medium whose permittivity, $\epsilon(r)$, fluctuates with respect to position in 3D space. However, the lack of information pertaining to the permittivity of human tissue and the lack of readily applied models means that this formulation finds little applicability in tissue optics[56]. The remaining models rely on the photon perspective of light, where the rigorous mathematical description provided by the Radiative Transport Theorem (RTT) contrasts with the simplistic Beer-Lambert model.

3.2.1 Radiative Transport Theorem

The following formulation of the radiative transport equation considers monochromatic light and disregards polarisation[57].

$$\frac{\partial I(\mathbf{r},\mathbf{s})}{\partial s} = -\mu_t I(\mathbf{r},\mathbf{s}) + \frac{\mu_s}{4\pi}\int_{4\pi} I(\mathbf{r},\mathbf{s}')f(\mathbf{s},\mathbf{s}')\mathrm{d}\Omega' \qquad [3.1]$$

The first term represents the net change in energy due to energy flow, where $I(\mathbf{r},\mathbf{s})$ is the radiance at a position $\mathbf{r}$ in direction $\mathbf{s}$. The second term represents the radiance lost due to absorption and scattering, where $\mu_t = \mu_s + \mu_a$, μ_s is the scattering coefficient and μ_a is the absorption coefficient. The last term represents the gain in radiance due to scattered light incident from all directions, where $f(\mathbf{s},\mathbf{s}')$ is the phase function that describes anisotropic scattering and $\mathrm{d}\Omega'$ is the solid angle. An anisotropy factor g represents the mean cosine of the scattering angle ($\mathbf{s}\cdot\mathbf{s}'$) and is used to describe the scattering anisotropy of a medium, where $g=0$ represents isotropic scattering and $g \rightarrow 1$ as scattering becomes more forward peaked. The diffusion approximation, also known as the P_1 approximation[58], assumes isotropic scattering through all media by using the transport scattering coefficient $\mu_s' = \mu_s(1-g)$.

3.2.2 Beer-Lambert Model for PPG

The Beer-Lambert model of PPG is used to describe the attenuation of light through a blood-filled medium and is usually expressed as

$$I = I_0 \exp\left(-\mu_{eff}(\lambda) r\right), \qquad [3.2]$$

where I_0 is the source intensity, I is the transmitted intensity, μ_{eff} is the effective absorbance and r is the optical path length. Under this formulation of the Beer Lambert law, μ_{eff} is assumed to have a static and a dynamic component:

$$\mu_{eff}(\lambda) r = \mu_{blood}(\lambda) d(t) + \mu_{tissue}(\lambda) r, \qquad [3.3]$$

where μ_{blood} and μ_{tissue} are effective absorbances for arterial blood and tissue—including non-pulsatile venous blood—respectively, $d(t)$ is the dynamic path length through the pulsating blood, and r is the constant path length through all other anatomical components. The dynamic absorbance component is further decomposed to take into account the oxygenation of the arterial blood:

$$\mu_{blood}(\lambda) = S\mu_{HbO_2}(\lambda) + (1-S)\mu_{Hb}(\lambda), \qquad [3.4]$$

where S is the arterial oxygen saturation, μ_{HbO2} is the absorbance due to oxyhaemoglobin, and μ_{Hb} is the absorbance due to deoxyhaemoglobin. A coefficient that is commonly used in pulse oximetry is the ratio of ratios R, which is defined as the ratio of the absorbance of blood at two illuminating wavelengths[14]:

$$R = \frac{\mu_{blood}(\lambda_1)}{\mu_{blood}(\lambda_2)} = \frac{S\mu_{HbO_2}(\lambda_1) + (1-S)\mu_{Hb}(\lambda_1)}{S\mu_{HbO_2}(\lambda_2) + (1-S)\mu_{Hb}(\lambda_2)}. \qquad [3.5]$$

Thus, the clinically significant oxygen saturation S can be determined from R and the effective absorbance of oxyhaemoglobin and deoxyhaemoglobin at the two wavelengths:

$$S = \frac{R\mu_{Hb}(\lambda_2) - \mu_{Hb}(\lambda_1)}{R\left(\mu_{Hb}(\lambda_2) - \mu_{HbO_2}(\lambda_2)\right) - \left(\mu_{Hb}(\lambda_1) - \mu_{HbO_2}(\lambda_1)\right)}. \quad [3.6]$$

The process of empirical calibration required in current practical pulse oximetry modalities as detailed in chapter 2, illustrates the inherent inaccuracy of this mathematical model.

3.3 PROPRIETARY OPTO-PHYSIOLOGICAL MODEL

A linear increase in the accuracy of a model for light propagation in *in-vivo* human tissue results in an exponential increase in its complexity. The high computational cost of numerical solutions to the radiative transport equation (RTE) is a clear illustration of this. On the other hand, the Beer-Lambert model for PPG is clearly oversimplified, as it disregards scattering effects. In this section we consider the set of simplifying assumptions that can be made in order to find a more optimum level of complexity for a novel opto-physiological model.

3.3.1 Numerical Radiation Transfer Equation

The model developed for this investigation relies on the output of Monte Carlo (MC) simulations as a numerical solution to the RTE. The following assumptions determine how MC ray-tracing and subsequent post-processing is performed:

- Time varying physiological components lead to changes in absorption but not to changes in scattering or tissue geometry.
- The diffusion (P_1) approximation provides a sufficiently rigorous description of optical scattering in all tissue of the arbitrary model.
- Differences between indices of refraction of relevant tissues are considered negligible; surface effects such as reflection and refraction are not considered, with one exception:
- Volumetric optical properties of bone are disregarded by using surface absorption and reflection.

The first assumption entails the use of time-varying absorption coefficients. The second involves the approximation of anisotropic scattering as isotropic, where the diffusion approximation can be applied numerically by converting μ_s and g to μ_s' through the relation $\mu_s' = \mu_s(1-g)$. For the third assumption, the only macroscopic index mismatch that is considered in the model is that found in the outermost surface of the measuring site. Finally, the contribution of bone to the numerical solution of RTE is approximated by disregarding its volumetric optical response through the use of surface optical properties, namely absorption and reflection.

3.3.2 Revised Beer-Lambert Formulation

The Beer-Lambert Law assumes a homogeneous non-scattering medium, where a detector is placed in transmission mode. In such a case, the detected irradiance will depend on the perpendicular alignment between light source and sensor and the path length, for a given source beam profile. However, this is not the case in tissue optics, where scattering results in the diffusion of transmitted intensity, which in turn modifies the effective irradiance at a detector in transmission mode. Equation 3.2 therefore employs arbitrary coefficients of absorbance which effectively represent a combination of absorption, scattering and geometric contributions of tissues to the attenuation of the signal. As such, these do not bear the fundamental physical significance of absorption and reduced scattering coefficients μ_a and μ_s', which represent mean number of absorption and isotropic scattering events per unit distance travelled, and are commonly used in more rigorous numerical solutions of tissue optics such as those based on the radiation transfer equation.

Light travelling through highly scattering tissue undergoes diffusion and on average travels a distance proportionally greater than the source-detector separation according to the degree of scattering in the medium. The PPG formulation of the Beer-Lambert law can therefore be modified to include a more descriptive characterisation of light-tissue interaction that is in line with standard tissue optics data found in the literature:

$$I = I_0 \exp\left(-\left(\mu_a(\lambda,t) + \mu_s'(\lambda)\varsigma\right)r\gamma\right), \qquad [3.7]$$

where $\mu_a(\lambda,t)$ is the time varying absorption coefficient, μ_s' is the reduced scattering coefficient, ς is the coefficient of effective attenuation due to scattering, r is the optical path length, and γ is a spatial coefficient that is dependent on sensor alignment and geometric factors of the medium. Here it is assumed that, out of the properties of scattering, absorption and geometric deformation, physiological pulsations only cause a significant variation in the absorption properties of the medium.

3.3.2.1 Mean Path Length

A more elegant and physically significant approach to the inclusion of scattering effects in definitions of attenuation has been proposed by Delpy et al.[59,60] Assuming that the absorption is proportionally increased according to the effective path length increase due to scattering, it is possible to model the attenuation as a factor of μ_a and the mean optical path length L:

$$I = I_0 \exp\left(-\mu_a(\lambda) L\right). \qquad \textbf{[3.8]}$$

We define the mean optical path length L as follows:

$$L = (F + G)\mu_s'(\lambda), \qquad \textbf{[3.9]}$$

where F is a factor that accounts for light source position, coherence and polarisation, and G is a geometrical factor that accounts for the morphology of a specific medium in relation to the full set of media and the light source position. Equation 3.8 can only hold true if all light exiting the scattering medium is accounted for, thus requiring the use of an all-inclusive mean path length. Consequently, an intensity term I_{diff} and a differential path length term l can be included to relate all-inclusive values to sensor-dependent ones:

$$I_{det} = \left(I_0 - I_{diff}\right)\exp\left(-\mu_a(\lambda) lL\right) \qquad \textbf{[3.10]}$$

Here, I_{diff} is the inbound energy that is eventually lost to non-detection and l is the mean path length factor, where $L_{det} = lL$ is the empirically significant mean path length of detected photon packets.

3.3.2.2 Optical Density

It is useful to work with Beer-Lambert equations in terms of the ratiometric attenuation or optical density (OD). Equation 3.8 yields the all-inclusive attenuation:

$$OD_{eff} = \log\left(\frac{I}{I_0}\right) = -\mu_a(\lambda)L. \qquad [3.11]$$

Equation 3.10 yields the sensor-dependent attenuation

$$OD_{det} = \log\left(\frac{I}{I_0 - I_{diff}}\right) = \log\left(\frac{I}{I_0}\right) - \log\left(1 - \frac{I_{diff}}{I_0}\right). \qquad [3.12]$$

This formulation leads to the definition of γ:

$$\gamma = \log\left(1 - \frac{I_{diff}}{I_0}\right). \qquad [3.13]$$

Finally, equation 3.12 can be rewritten as

$$OD_{det} = OD_{eff} - \gamma = -\mu_a(\lambda)L_{det}. \qquad [3.14]$$

In the above equations, OD_{eff} is the effective attenuation when taking into account energy not falling within the detector, OD_{det} is the attenuation of detected light, and γ can clearly be defined as the sensor-dependent attenuation due to undetected photon packets. In terms of optical density, the attenuation of light through a set of media $m_1, m_2, \ldots, m_n$ is simply $I_0\exp(OD_1+OD_2+\ldots+OD_n)$.

3.3.2.3 Time-Variant Absorption

The time varying nature of a PPG signal is known to be due to the periodic oscillation in perfusion of blood vessels at every scale. Since it is not possible to create a model that accurately distinguishes between tissues and their blood vessels, it is a necessary step to assume tissue homogeneity. Consequently, changes in tissue perfusion have to be modelled as a homogeneous change in the optical properties of the tissue. We can use a coefficient to represent the variation in absorption with respect to a static absorption and develop a complete description of μ_a:

$$\mu_a(\lambda,t) = \mu_{a(static)}(\lambda)\left(1+\sigma\rho(\omega t)\right). \qquad [3.15]$$

Here, $\mu_{a(static)}(\lambda)$ is the mean absorption coefficient, $\rho(\omega t)$ is the function of a normalised PPG waveform and σ is the coefficient of pulsatility, where σ ranges from 0 for $\mu_a = \mu_{a(static)}$ to 1 for μ_a oscillating between 0 and $2\mu_{a(static)}$. It follows that $\Delta\mu_a = \sigma\mu_{a(static)}$, therefore we can rewrite Equation 3.11 to define the attenuation change:

$$\Delta OD_{eff} = \log\left(\frac{\Delta I}{I_0}\right) = \sigma\mu_a(\lambda)L. \qquad [3.16]$$

It follows that the dynamic attenuation oscillates between $OD_{eff} \pm \Delta OD_{eff}$, thus:

$$OD_{eff}(t) = OD_{eff} + \Delta OD_{eff}\rho(\omega t). \qquad [3.17]$$

3.3.3 Resultant Opto-Physiological Model

The description of our model requires that we consider a set of steady-state radiation transport data $R=\{I_{in}(n), I_{out}(n), L_{sys}(n)\}$ where a given light source $T=\{\lambda\}$ radiates at a given position of a composite medium $M=\{m(n)\}$ composed of $n+1$ optical media. Under this definition, $I_{in}(n)$ and $I_{out}(n)$ are the intensities of all light entering and exiting $m(n)$ respectively, and $L_{sys}(n)$ is the mean path length of all rays traversing the same medium. Every component of M has a set of coefficients that determine the behaviour of light propagating within; $m(n)=\{\mu_s'(n), \mu_a(n,t), \sigma(n)\}$. Medium $m(0)$ is a

special case since it represents the ambient medium ($\mu_s'(0)=0$, $\mu_a(0,t)=0$, $\sigma=0$), where $I_{out}(0)$ is the total initial intensity exiting from the light source in $m(0)$ into $m(1)$ with a negligible mean path length ($L_{sys}(0)=0$), and $I_{in}(0)$ is the total detectable intensity exiting the outermost scattering medium $m(1)$.

One such set of data $\{R,T,M\}$ will heretofore be referred to as a system. This treatment of a system is compatible with numerical RTT data generated through MC simulation.

3.3.3.1 Complete System Description

Every medium experiences a mean path length $L_{sys}(n)$ that translates to a mean optical density according to the absorption coefficient of the medium:

$$OD_{eff}(n,t) = \log\left(\frac{I_{out}(n)}{I_{in}(n)}\right) = \left(\sigma(n)\rho(\omega t)-1\right)\mu_a(n)L_{sys}(n). \qquad [3.18]$$

This yields a system attenuation defined as:

$$OD_{sys}(t) = \log\left(\frac{I_{in}(0)}{I_{out}(0)}\right) = \sum_{i=1}^{n}\left(\left(\sigma(i)\rho(\omega t)-1\right)\mu_a(i)L_{sys}(i)\right), \qquad [3.19]$$

where $I_{out}(0)$ is the light source intensity and $I_{in}(0)$ is the total detectable intensity. In the above definitions, $L_{sys}(n)$ accounts for all photon packets traversing medium m_n and is thus affected by the entire geometrical description of the system.

3.3.3.2 Sensor-Dependent Description

The outermost layer (epidermis) is of particular importance as its outer surface corresponds to the area on which a sensor can be placed. It is useful to approximate it as the surface of a cylinder (x,θ) when considering sensor placement, where x is the longitudinal axis of the finger, and θ is the position along its circumference. Given that the circumference of the finger at x is known, a rectangular sensing area $S_s=\{w,h\}$ can be mapped onto the outermost surface of the composite medium.

An additional set of ratiometric coefficients $C_s=\{\gamma(n,x,\theta,s),l(n,x,\theta,s)\}$ can now be defined for each sensing area S_s, where γ is the ratio of detected to total light entering and exiting a layer n of the composite medium M, and l is the ratio of detected to system mean path length for layer n, both of which are with respect to detector position and dimensions. When using a sensing area of static dimensions, the sensor-dependent attenuation can be written as

$$OD_{det}(t,x,\theta)=\sum_{i=1}^{n}\left(\left(\sigma(i)\rho(\omega t)-1\right)\mu_a(i)L_{det}(i,x,\theta)\right), \qquad \textbf{[3.20]}$$

where x and θ denote a specific position of the sensing area, and the sensor-dependent mean path length is $L_{det}(i,x,\theta)=l(i,x,\theta)L_{sys}(i)$.

3.3.4 Empirical Equivalence

Assuming a constant light source intensity, the static and peak dynamic components $I_{DC}(\lambda,x,\theta)$ and $I_{ACpeak}(\lambda,x,\theta)$ of a PPG waveform $I_{AC}(t,\lambda,x,\theta)$ as detected from a sensor located at (x,θ), are available empirically by filtering and subsequent separation of the latter. It is common practice to assume that the intensity variation in a PPG signal is solely due to the pulsation of arterial blood[14]. Under this assumption, the empirical definition of the clinically significant ratio of ratios R for wavelengths λ_1 and λ_2 is

$$R(\lambda_1,\lambda_2)=\frac{I_{AC\,peak}(\lambda_1)/I_{DC}(\lambda_1)}{I_{AC\,peak}(\lambda_2)/I_{DC}(\lambda_2)}. \qquad \textbf{[3.21]}$$

In order to equate the sensor dependent description of the opto-physiological model, Equation 3.20 is decomposed into analogous static and peak dynamic attenuations OD_{DC} and OD_{AC}:

$$OD_{DC}(x,\theta)=\sum_{i=1}^{n}\left(-\mu_a(i)L_{det}(i,x,\theta)\right), \qquad \textbf{[3.22]}$$

$$OD_{AC}(t,x,\theta)=\sum_{i=1}^{n}\left(\sigma(i)\rho(\omega t)\mu_a(i)L_{det}(i,x,\theta)\right). \qquad [3.23]$$

Conversion into static and peak dynamic intensities I_{DC} and I_{ACpeak} requires that these be made exponential:

$$I_{DC}(\lambda,x,\theta)=I_0\exp\left(\sum_{i=1}^{n}\left(-\mu_a(\lambda,i)L_{det}(\lambda,i,x,\theta)\right)\right), \qquad [3.24]$$

$$I_{ACpeak}(\lambda,x,\theta)=I_0\exp\left(\sum_{i=1}^{n}\left(\sigma(\lambda,i)\mu_a(\lambda,i)L_{det}(\lambda,i,x,\theta)\right)\right). \qquad [3.25]$$

Using Equations 3.24 and 3.25, the peak dynamic intensity is normalised with respect to the corresponding DC intensity, thus yielding a characterisation that is independent of the light source:

$$\frac{I_{ACpeak}}{I_{DC}}(\lambda,x,\theta)=\exp\left(\sum_{i=1}^{n}\left(\left(1+\sigma(\lambda,i)\right)\mu_a(\lambda,i)L_{det}(\lambda,i,x,\theta)\right)\right) \qquad [3.26]$$

A new equation for R can now be derived:

$$R(\lambda_1,\lambda_2)=\frac{\exp\left(\sum_{i=1}^{n}\left(\left(1+\sigma(\lambda_1,i)\right)\mu_a(\lambda_1,i)L_{det}(\lambda_1,i,x,\theta)\right)\right)}{\exp\left(\sum_{i=1}^{n}\left(\left(1+\sigma(\lambda_2,i)\right)\mu_a(\lambda_2,i)L_{det}(\lambda_2,i,x,\theta)\right)\right)} \qquad [3.27]$$

Finally, knowledge of the effective absorbances at the two relevant wavelengths allows us to determine oxygen saturation S through Equation 3.6.

3.3.5 Applicability of the Opto-Physiological Model

3.3.5.1 Optimum Sensor Placement

When normalised, the peak dynamic intensities essentially represent the signal-to-noise ratio at the measuring site with respect to the corresponding wavelength. Assuming a high degree of symmetry in the circumferential response of a human finger, pairs of optimum sensor placement locations Θ_1 and Θ_2 can be defined with respect to longitudinal position:

$$\Theta_1(x) = \max\left\{\sum_{i=1}^{2}\frac{I_{ACpeak}}{I_{DC}}\left(\lambda(i), x, \theta[0,\pi)\right)\right\} \quad \textbf{[3.28]}$$

$$\Theta_2(x) = \max\left\{\sum_{i=1}^{2}\frac{I_{ACpeak}}{I_{DC}}\left(\lambda(i), x, \theta[\pi,2\pi)\right)\right\} \quad \textbf{[3.29]}$$

3.3.5.2 Sensor Motion Artefact

It is possible to predict the PPG signal that results from a predefined motion of the sensor. To achieve this, x and y motions of the sensor are mapped to the longitudinal and circumferential axes of the cylindrical model of the finger, and optical coupling between the sensor and sensing site is represented as motion in the z axis, where the latter is modelled as a change in sensor window size:

$$I_{AC}(t) = I_0 \exp\left(\sum_{i=1}^{n}\left(\left(\sigma(i)\rho(\omega t)-1\right)\mu_a(i)L_{det}\left(i, x(t), \theta(t), s(t)\right)\right)\right) \quad \textbf{[3.30]}$$

This formulation assumes a static geometry with respect to time.

This chapter has summarised the concepts of optics and physiology that are relevant to this research project, specifically those pertaining to human tissue optics and the circulatory system. Two mathematical models commonly used in opto-physiological modelling have been presented; the simplistic Beet-Lambert model for photoplethysmography and the rigorous Radiative Transport Theorem. The proprietary theoretical model used in this project have been derived from the aforementioned models and its applicability has been detailed.

4. SIMULATION AND EMPIRICAL VALIDATION OF OPTO-PHYSIOLOGICAL MODEL

The experimental platform of this research consists of an empirical setup and a virtual simulation environment for a standard arrangement of transmission-mode pulse oximetry. The platform aims to provide a detailed description of the physical mechanisms involved in the empirical setup by mirroring the latter in a virtual environment. The correlation between the limited amount of data available empirically and its corresponding numerically computed data determines the validity of the vast amounts of relevant information available from the virtual environment. Having established the degree of correlation between these outputs, the statistical analysis of the full set of simulated data is used to derive an improved opto-physiological model for the mechanisms of pulse oximetry.

4.1 EXPERIMENTAL PLATFORM OVERVIEW

The complete experimental platform created in this research consists of a hardware setup used for measurement of transmitted light distributions under a standard arrangement of transmission-mode pulse oximetry, and a virtual environment that emulates this setup by modelling its elements and simulating the physical and physiological phenomena involved in its operation.

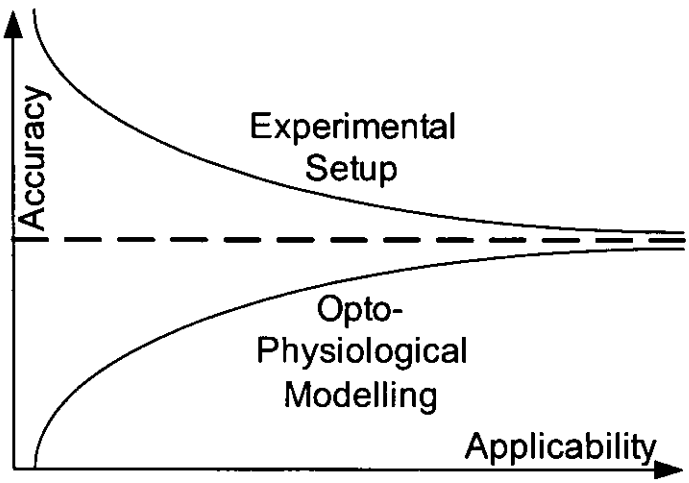

Figure 4.1 - Graphical representation of the aim towards applicability in this research.

Figure 4.1 illustrates the trade-off between accuracy and applicability that is inherent in the process. A highly accurate description of the physical system would include anatomical details down to a sub-microscopic scale, making it impractical to model. Conversely, an oversimplified model of the real-life system would, for example, disregard scattering effects within human tissue, thus tending to invalidate it as a representation of the system. The platform aims to arrive at a model that is able to predict the widest range of empirical outcomes while maintaining the highest possible level of accuracy. This requires an optimum extraction of useful data from as small a set of empirical results as possible.

The objectives of this experiment are:

- To develop the empirical validation platform and protocol towards an increasingly repeatable standard.

- To adjust the parameters and coefficients of the opto-physiological model at the core of the simulation platform towards making the latter correlate with validation in terms of their outputs.

Once an adequate correlation is reached between the two sides, the simulation environment defined by the parameters and coefficients established in the second objective can be used to accurately predict the outcome of a range of relevant practical systems.

4.2 MONTE CARLO SIMULATION ENVIRONMENT

A platform was developed for MC ray tracing of complex tissue geometries. The platform utilises three commercially available software packages (3D Studio MAX, OptiCAD, MATLAB), and can be sectioned into several phases of operation, namely model preparation, simulation, interfacing and post-processing, as shown in Figure 4.2. A 3D anatomical model of a male adult finger was used to numerically resolve the RTT equation for the case of a single LED light source at 633nm and 850nm, placed near the standard position found in commercial probes.

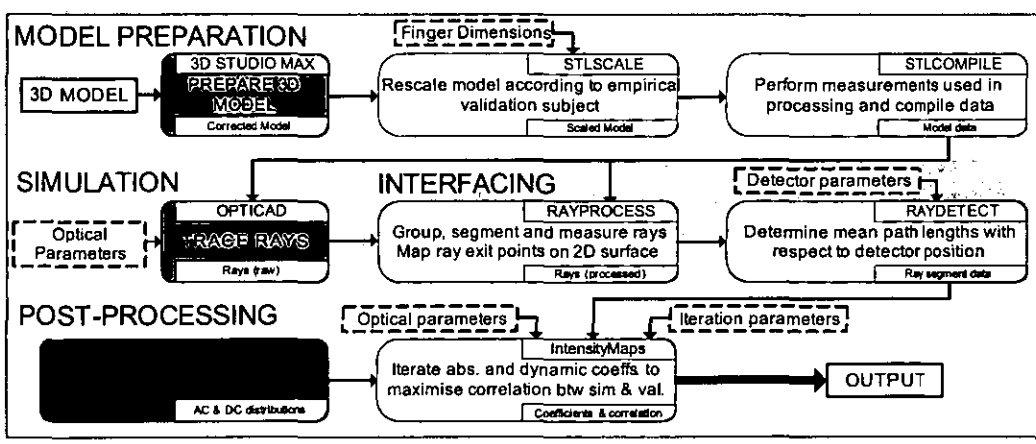

Figure 4.2 - Block diagram of MC raytracing platform where MATLAB functions are labeled in blue blocks and steps involving other software platforms are labeled in red blocks.

The main process of MC ray tracing was performed by OptiCAD (Opticad Corporation, USA), which outputs the coordinates of traced ray vertices onto a file. Post-processing was performed in MATLAB (Mathworks Co., USA) through the use of custom algorithms specific to the outputs of the previous phases. OptiCAD was selected by virtue of its being one of the only available software platforms capable of performing Monte Carlo simulations of optical propagation in arbitrary geometries. Similarly, MATLAB was chosen as a highly efficient development language for data processing algorithms.

4.2.1 Model Preparation

Figure 4.3 shows the accurate 3D anatomical model (Zygote Media Group, USA) of a male adult finger composed of bones, tendons, nerves, arteries, veins and outer skin that was purchased and employed as the base model for this investigation. 3D Studio MAX v.9.0 (Autodesk, USA) was employed to make modifications to the base model in order to make it compatible with the raytracing software.

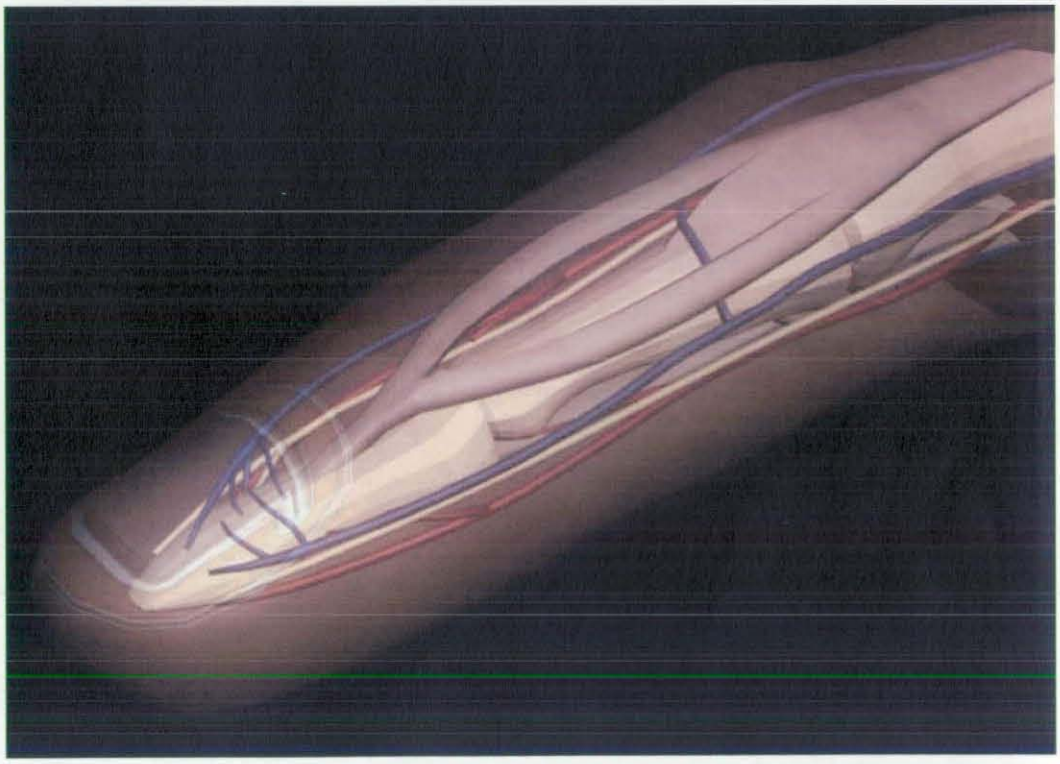

Figure 4.3 - 3D finger model used for Monte Carlo Simulations.

The first phase of model preparation consisted of the following steps:

- Correction of overlaps between objects in the model
- Creation of five-layer skin in accordance to the skin model described by Tuchin et al.[49]
- Creation of subcutaneous fat as a filler between the skin layers and all other internals.
- Rotation of the model: lengthwise alignment to the x axis with top of model pointing in the +z direction.
- Translation of the model for minimum x, y and z extents of model to be just above zero.
- Generation of separate stereolithography STL files for each of the objects in the model.

The second phase comprises scaling of the model in accordance to the dimensions of the subject. MATLAB function *STLscale* does this by measuring the outermost layer of the model (epidermis), determining 3D scaling factors from comparison of subject and model phalange measurements, and scaling each layer of the model with these factors. Finally, *STLcompile* is in charge of sequentially reading the files for each model layer, performing calculations to be used during data processing, and compiling all data into a structure. A block diagram of these can be seen in Figure 4.5.

4.2.2 Monte Carlo Simulation Settings

Simulations were configured in accordance to a series of simplifying assumptions. Internal reflection and refraction between boundaries were disregarded, with the exception of that between epidermis and air, for reasons explained in the previous chapter. The contribution of bone structures was simplified by disregarding their volumetric optical properties and only taking into account surface reflectance. The diffusion approximation of the radiative transport theory, also known as the P_1 approximation[58], was used for all volumetric optical parameters in the simulation in order to reduce the ray tracing time by a factor of approximately five, and rays were traced using spatial and angular Sobol sampling[62] to increase the convergence rate of

the data. The representation of light in terms of photon packets with an associated weight intrinsically allows us to disregard quantum effects.

Energy threshold for traced ray setting is set very low (0.001% of ray's incident energy) to ensure that all rays exit the model. This ensures that all rays are 'detectable' even though their energy might be negligible, thus resulting in a homogeneous output that can be processed more reliably.

All ray traces were performed using a 1mm diameter spherical light source with a lambertian intensity distribution whose half widths were capped according to the specifications of the LEDs used in validation. This approach was used as an approximation to both standard and resonant cavity LEDs to simplify the procedure. Reflection and refraction at interfaces resulting from refractive index mismatches are neglected. Apart from yielding an intrinsic reduction in ray tracing times, this ensured minimisation of inaccuracies due to the inherently difficult task of modeling the microscopic textures of interfaces, which would otherwise pose a significant level of complexity in contrast to their minor contribution to the output (reflection reference).

OptiCAD treats the imported components of the 3D model as solids and allows the volumetric optical properties (absorption coefficient μ_a, scattering coefficient μ_s, and anisotropy factor g) of each to be defined. Transport scattering coefficients μ_s' at 633 nm, derived from $\mu_s' = \mu_s(1-g)$, are used for all media in the model to significantly reduce raytracing time. Only the surface optical properties of bone were considered, namely its diffuse reflectance and transmission. MC simulation results from OptiCAD were utilised solely for the ray paths as determined by the scattering coefficients. Absorption coefficients were resolved in post-processing (see section 4.3.4). The reduced scattering coefficients and ranges of absorption coefficients used in this simulation were all determined from Tuchin's review of tissue optical properties in literature and can be found in the following chapter. The OptiCAD user interface can be inferred in Appendix III.

4.2.3 Data Processing

Several algorithms were made into functions for the processing and analysis of output data from OptiCAD, all of which have been optimised in terms of speed, memory usage and data pipelining capability. Pipelining was achieved by subdivision of raw data into files containing full subsets of rays, and subsequent generation of files for processed data. All coding was performed using MATLAB 2007a.

4.2.3.1 Data Structures

	Item	Row Format	Description
V	*.verts*	$[x_1\ y_1\ z_1]$	Cartesian coordinates of each vertex
	.lengths	$[l_1]$	Length of segment between each vertex pair
	.powers	$[p_1]$	Power of ray upon reaching each vertex
S	*.flags*	$[f_1]$	Layer containing each segment
	.lengths	$[l_1]$	Path length of each segment
	.groups	$[s_1\ e_1]$	Start and end vertices of each segment
R	*.rayends*	$[x_1\ y_1\ z_1]$	Cartesian coordinates of last vertex of each ray
	.flats	$[x_1\ d_1]$	Cylindrical coordinates of last vertex of each ray
	.vgroups	$[s_1\ e_1]$	Pointers to first and last vertices of each ray
	.sgroups	$[s_1\ e_1]$	Pointers to first and last segments of each ray
D	*.rays*	$\{r_1 \ldots\}\ \{\ldots\}$	Lists of detected rays within each detector pos.
G	*.DET*	$\{L_1\ L_2\ \ldots\}\ \ldots$	Sum of lengths of segments by layer and detector
	.SYS	$[L_1\ \ldots\ L_2]$	Sum of lengths of all segments by layer
	.DETnrays	$[n_{1,1}\ n_{2,1}\ \ldots]$	Total ray count for each detector position
	.SYSnrays	N	Total system ray count
	.MPL	$\{l_1\ l_2\ \ldots\}\ \{\ldots\}$	Mean path lengths of each layer at each detector
	.OD	$[o_{1,1}\ o_{2,1}\ \ldots]$	Sums of optical densities of rays within detector
	.DOD	$[d_{1,1}\ d_{2,1}\ \ldots]$	Sums of dynamic ODs of rays within detector

Table 4.1 - Contents and row format of data structures passed between processing functions

Data passed between functions are subdivided into files, each of which contains a complete number of rays. Each of these files contain structures (*V,R,S,D,G*) which

group relevant ray data in terms of the vertex, ray, segment, detector and global domains. The components of the vertex structure (*V*) are all as long as the sum total of vertices for all stored rays. In the context of simulation, a ray segment refers to the portion of a ray within a single layer of the model. Thus, the components of the segment structure (*S*) are all as long as sum total of segments for all stored rays. Similarly, the length of ray structure (*R*) components is equal to the number of rays stored in the file. The detector structure (*D*) consists of 2-D arrays of data where each element corresponds to a virtual detector position. Finally, the global data structure (*G*) contains data pertaining to the complete set of MC data, such as the wavelength of the light source and any data produced from the complete set of data files. The structure of these is shown in Table 4.1, where the format of a single row of data is shown.

4.2.3.2 Interfacing Functions

Several functions, namely *Ray2Mat*, *RayProces*, and *RayDetect*, serve as the interface between the raw simulation data as output by OptiCAD and the iterative analysis phase, where the data are manipulated in order to produce significant results and conclusions.

Raw data from MC ray traces consists of datasets *V.verts* and *V.powers*. The *Ray2Mat* function reads raw OptiCAD ray trace data, splits it into full subsets of rays, and compresses the data into multiple files ready to read by subsequent algorithms. The *RayProcess* function delimits rays with respect to vertices and segments, labels ray segments by layer, measures segment path lengths, and converts 3D Cartesian coordinates of ray exit points (detectable) into 2D cylindrical coordinates for surface mapping. An additional raw dataset *V.num* enumerates ray vertices and is used to delimit rays within the raw data, after which it is discarded. Segments are delimited through the use of *V.powers*, where the vertices *v* at which *V.powers*(*v*)-*V.powers*(*v*-*1*)=0 are the boundary vertices. This effect was due to the finite separation that OptiCAD required between layers of the model, which results in the generation of short ray sub-segments connecting model layers during ray tracing.

The process of labelling segments according to the layer of the model within which they reside proved to be a reverse engineering feat since OptiCAD did not provide

this information upfront. The ability to use *V.powers* as a means of delimiting segments proved to be a crucial step in the process. Subsequent steps consisted of an intersection analysis between all boundary vertices and the model facets which are closest to these.

The process consisted of the following steps:

- Selection of boundary and adjacent vertices
- Definition of cubes for each model facet in which each side was larger than the facet extents according to the maximum *V.lengths*.
- Selection of vertices within each cube
- Rotation of each facet together with each vertex within the corresponding cube so as to align the facet normal to the y axis
- Redefinition of cube to fit facet in the x and z dimensions and to be defined in the y dimension according to $y_{cube}=y_{facet} \pm \max(V.lengths)$.
- Selection of subset of vertices within redefined cube
- Intersection analysis of sub-segments and facet for determination of segment-layer relationship.
- Storage of segment labels as *S.flags*.

This level of complexity was necessary in order to reduce the significant data processing time required to complete the process.

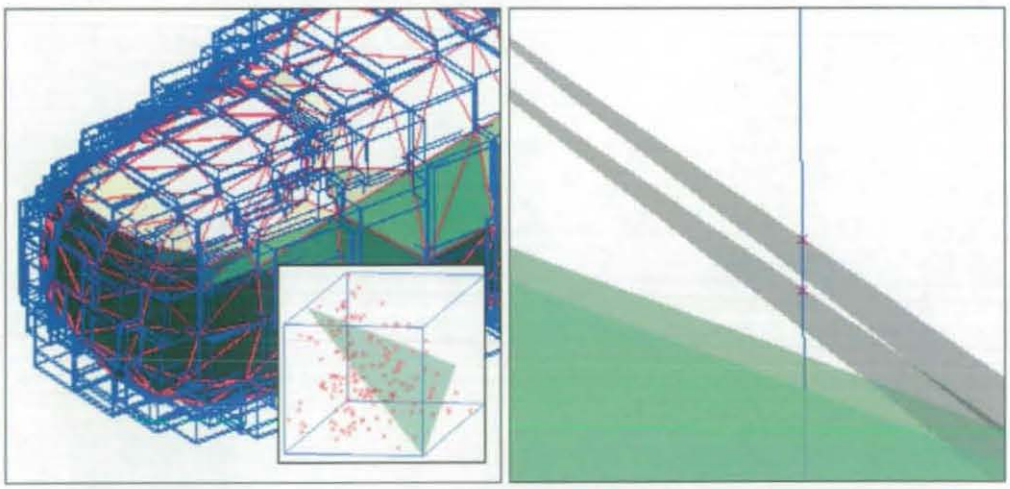

Figure 4.4 - Illustration of the process of labelling ray segments, showing process optimisation by means of grouping of vertices according to face extents (left) and ray inter-layer segments where ray power output of OptiCAD remains constant (right).

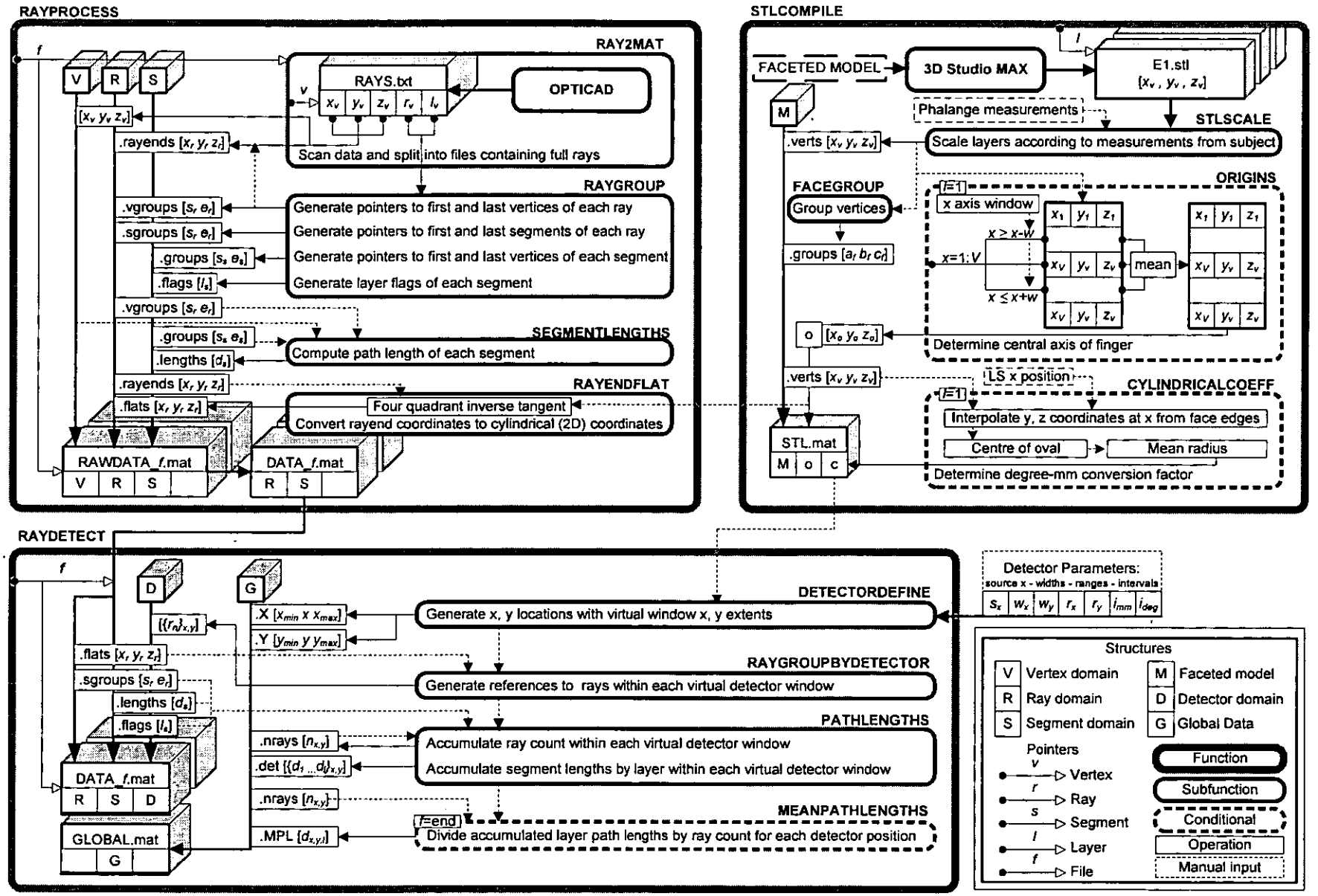

Figure 4.5 - Block diagram of interfacing and model preparation functions.

Segment lengths are determined in two steps: In the vertex domain,

$$V.lengths(v) = \left| V.verts(v) - V.verts(v-1) \right|. \qquad \textbf{[4.1]}$$

where v is the vertex pointer. In the segment domain:

$$S.lengths(s) = \sum_{i=S.vgroups(s,1)}^{S.vgroups(s,2)} V.lengths(i), \qquad \textbf{[4.2]}$$

where s is the segment pointer.

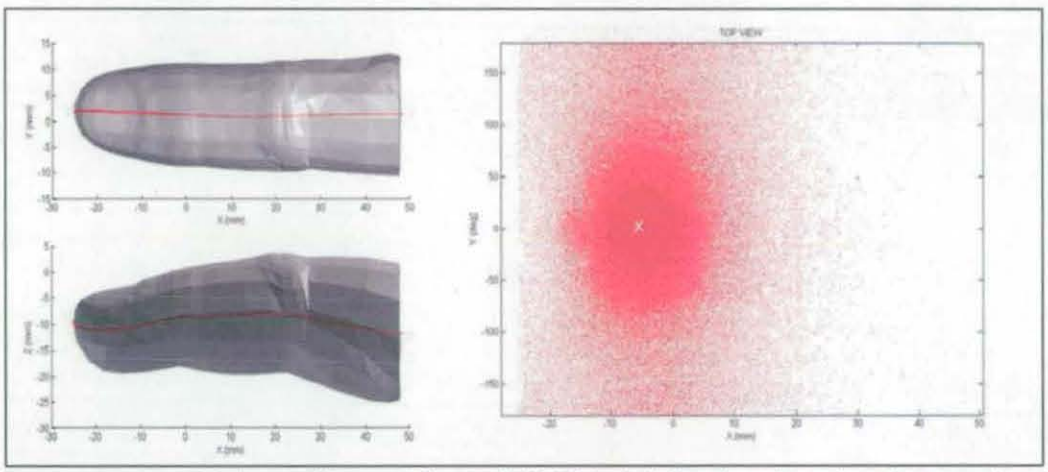

Figure 4.6 - Outer skin layer with central finger axis highlighted (left) and resultant plot after conversion of transmitted ray coordinates (right), where the light source position is marked by an x.

3D Cartesian coordinates of ray ends are converted to cylindrical coordinates by using the previously determined central axis of the finger model and applying a four quadrant inverse tangent on the vertices as demonstrated in Figure 4.6.

RayDetect is used to define the shape and extents of motion of a virtual detector, and to generate maps of mean path lengths for all defined detector positions. Intensity maps resulting from mean path length outputs were confirmed by performing an equivalent ray-by-ray analysis, which yielded perfect correlation. This process is the final stage in the interfacing process, and as such consists of defining detector characteristics that will coincide with those used in validation data processing. These are detailed in the following section.

Mean path lengths are determined as follows: First, path lengths are accumulated for every layer at every detector position as

$$D.DET(l,x,y) = \sum_{i=s(1)}^{s(n)} S.lengths \qquad [4.3]$$

Where s_{sel} contains pointers to all segments within layer l for all ray ends within position (x,y):

$$s_{sel} = \left(\bigcup_{r \in D.rays(x,y)} \{R.sgroups(r,1) : R.sgroups(r,2)\} \right) \bigcap S.flags = l, \qquad [4.4]$$

and n is the number of elements in s_{sel}. It follows that

$$G.MPL_{x,y}(l) = G.DET_{x,y}(l) / G.DETnrays(x,y), \qquad [4.5]$$

where x and y are detector surface coordinates and l is the layer.

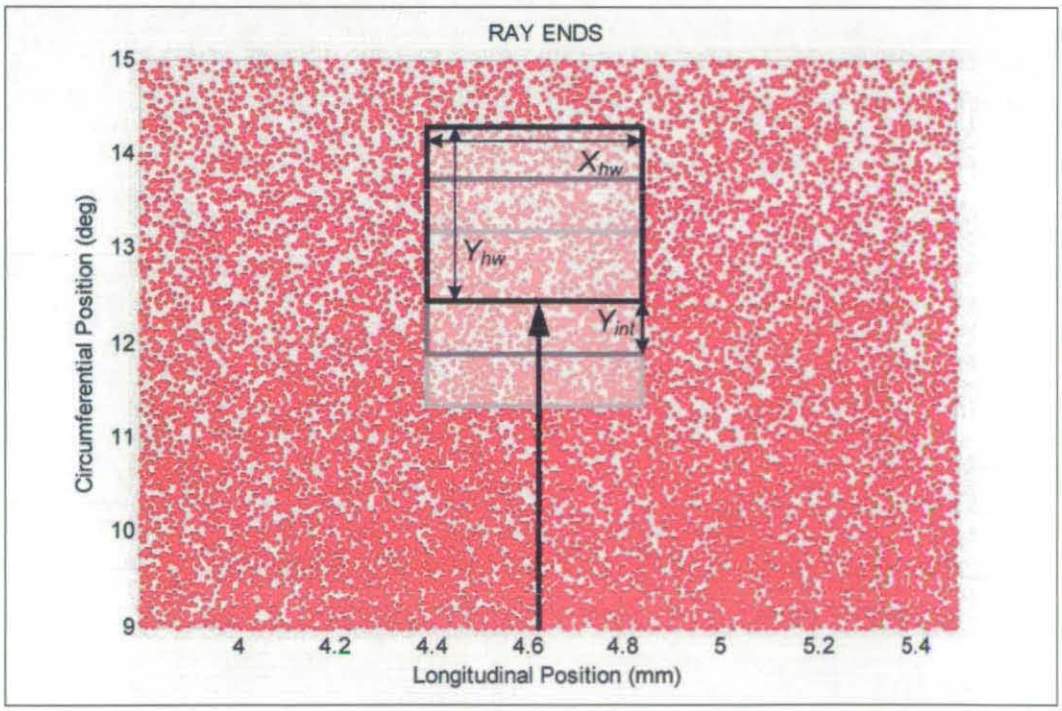

Figure 4.7 - Illustration of virtual detection of traced rays.

Mean path length data are solely dependent on the scattering coefficients defined during MC simulation. These data represent the characteristics of the ray cloud generated during MC simulation; therefore it cannot be iterated in post-processing. Consequently, mean path length data serves as the fully processed core data to be used for construction of intensity distributions according to arbitrary absorption coefficients.

4.3 EMPIRICAL VALIDATION PLATFORM

A hardware platform that is able to record intensity responses around a finger was developed for validation of the opto-physiological model. These responses serve as reference intensity distributions for comparison with those provided by the MC simulation platform. This is achieved in two steps. First, light intensity distributions are constructed from *in-vivo* PPG measurements taken from a series of points on the surface of a test subject's finger by means of a sensing hardware setup. These distributions are then correlated with the corresponding MC output data, which are distilled from the complete system output according to the spatial locations of empirical measurements.

4.3.1 Sensing Hardware

It was determined that limiting MC output and empirical measurements to the circumference of the finger in which the light source is located is the ideal approach to validation based on its inherent simplicity and robustness. In terms of simplicity, it is straightforward to define the circumference of a finger and to constrain the motion of measuring equipment accordingly, and in terms of robustness, it is safe to assume that a finger shows minimal physical variation along its longitudinal axis, thus minimising the effect of potential mismatches in source and detector locations between simulation and validation. The requirement for such a platform therefore became the ability to record PPG signals from arbitrary positions along the circumference of a finger. To this end, two hardware solutions were developed, one employing a photodiode array, and another employing CCD/CMOS cameras.

Physical limitations in the experimental setup dictated that empirical measurement, and indeed all analysis within the scope of this research project, be limited to transmission-mode from around 90° to 270°, where the 0° mark corresponds to the light source position.

4.3.1.1 Hardware Solution 1: Photodiode Array

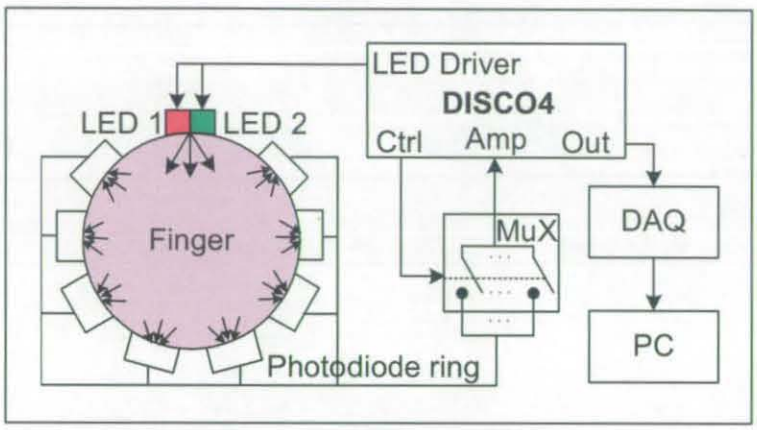

Figure 4.8 – Diagram of Photodiode array solution.

Figure 4.9 - Photodiode array solution for recording transmitted intensity distributions. Photodiode array ring sensor with dual wavelength light source (left) and finger placement prior to securing (right).

The photodiode array solution consists of eight photodiodes (RS Components, UK) forming a ring, and two surface mount LEDs (Farnell, UK). Electronics for the ring sensor consisted of a PPG hardware platform (DISCO4, Dialog Devices, UK) driving two surface-mount LEDs, triggering a low-noise multiplexer to switch between the array sensors, and capturing the multiplexed signal through its amplifier stages. A

custom LabVIEW virtual instrument was used to control the DISCO4 and to stream data from a USB data acquisition device (National Instruments, USA). This virtual instrument is documented in Appendix II.

4.3.1.2 Hardware Solution 2: Imaging

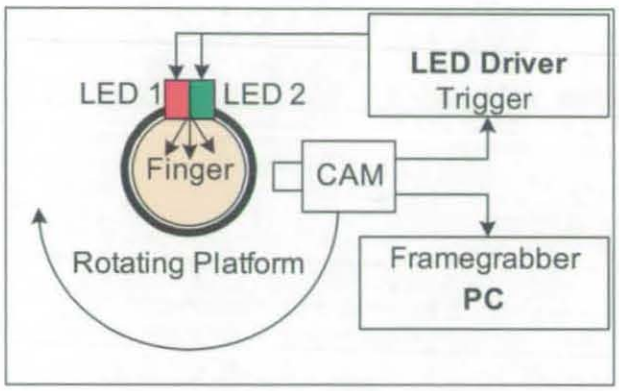

Figure 4.10 – Diagram of Imaging solution.

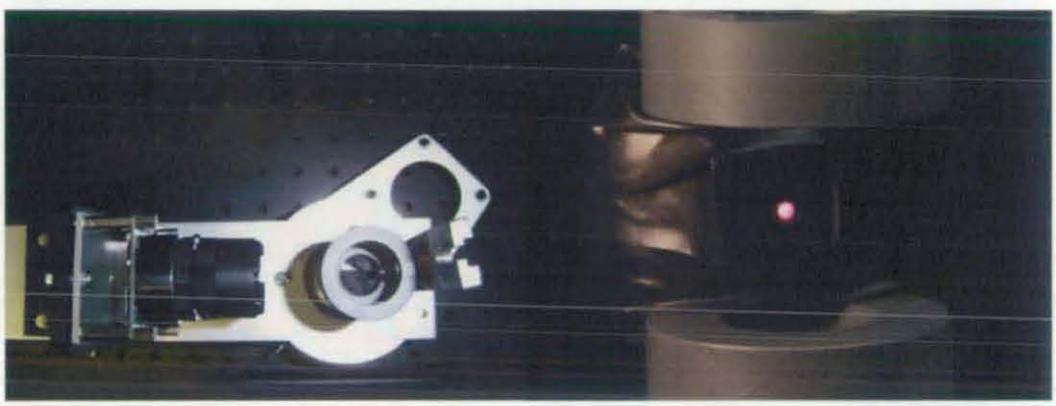

Figure 4.11 - Overview of Imaging solution rotating platform fitted with an 8 bit camera (Mightex, USA) (left), and finger support structure with light source pad (right).

For the imaging solution, a rotating platform was developed, capable of seating a digital CCD or CMOS camera concentric to a support structure for the subject's finger. The rotating platform allows the camera to maintain a constant distance and alignment with respect to the subject's finger. The support structure consists of two hard plastic rings placed concentric to each other and foam padding for the tip and back of the finger, the latter of which houses an ergonomic plastic pad containing the

light source. This arrangement ensures minimal motion while minimising pressure on the finger as shown in Figure 4.12.

The imaging setup consists of the following:

- Rotating platform
- 12 bit monochrome CCD camera (Hamamatsu Photonics, Japan)
- LED driving circuitry
- Cameralink interface frame grabber (Mikrotron, Germany)
- Custom LabVIEW frame grabber control software

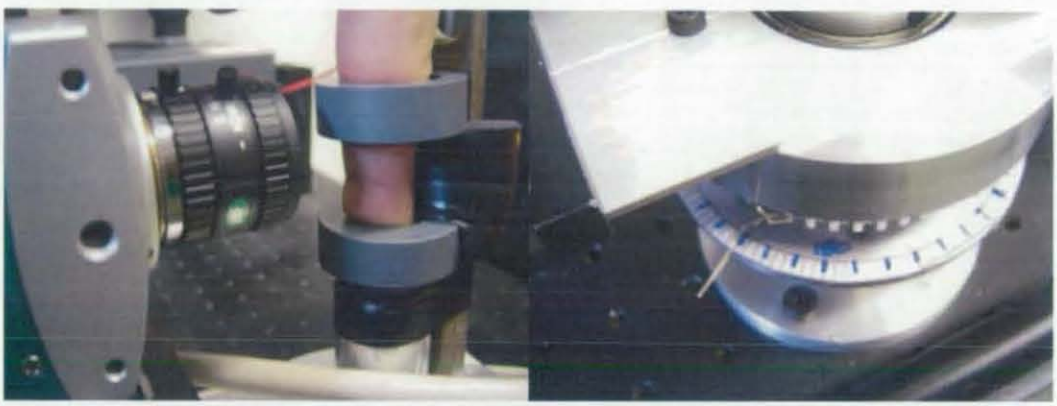

Figure 4.12 - Finger placement on rotating platform (left) and circumferential position indicator (right).

The hardware is configured to capture a sequence of frames in synchronisation with the light source, where each of the two LEDs is triggered in an alternating sequence. The result of this is a multiplexed sequence in which every other frame corresponds to an illumination wavelength. LED circuitry is triggered by the 'frame valid' signal from the camera, which indicates the period of exposure of each frame. A sequence of frames long enough to construct PPG signals is captured for each position. The frame grabber and customised LabVIEW control software is detailed in Appendix I. Several cameras were assessed in preliminary validation experiments performed during the development of a protocol for this solution. The details of these cameras are discussed in Chapter 5.

4.3.2 Construction of Empirical Intensity Distributions

4.3.2.1 Ring Sensor

Processing of raw data from the ring sensor was performed using MATLAB and consisted of the following steps:

- Removal of transitions between sensors by means of a control signal;
- De-multiplexing of raw data into continuous signals from each photodiode;
- Manual trimming of individual PPG signals for removal of artefact regions;
- Low-pass filtering of raw PPG signals for removal of noise;
- Extraction of quasi-static DC components from raw signals via low-pass filtering;
- Extraction of AC components via subtraction of DC from raw signals;
- Positive and negative AC signal envelope detection, and subsequent determination of peak-to-peak AC signal amplitudes; and,
- Determination of maximum, mean, and minimum intensities for DC and peak-to-peak AC signals from each photodiode.

The values determined from the final step were mapped to the corresponding physical location of each sensor in the ring, thus providing discrete static and dynamic intensity maps.

4.3.2.2 Imaging Platform

The resultant data from imaging experiments was processed using MATLAB in two different ways. The first of these yielded discrete values of DC and peak-to-peak AC for each circumferential position of the raw data and was performed in accordance to the following steps:

- De-multiplexing of raw frame sequence into separate sequences for each light source wavelength;
- Manual inspection of frame sets and subsequent determination of centre of image in the longitudinal axis of the finger (rotating platform is calibrated to

maintain alignment with the centre of the width of the finger prior to recording, yielding a known centre at half the width of the corresponding frame axis);

- Definition of a square window of arbitrary size centred on (x,y) pixel coordinates determined in previous step, followed by cropping of all frames
- Averaging of resultant cropped frames to form raw PPG signals for each position and each wavelength;
- Manual trimming of individual PPG signals for removal of artefact regions;
- Noise reduction filtering of individual signals;
- Extraction of quasi-static DC components from raw signals via low-pass filtering;
- Extraction of AC components via subtraction of DC from raw signals;
- Positive and negative AC signal envelope detection, and subsequent determination of peak-to-peak AC signal amplitudes; and,
- Determination of maximum, mean, and minimum intensities for DC and peak-to-peak AC signals from each position at each wavelength.

The second technique yielded much higher continuity in the characterisation of distributions by essentially providing values at spatial increments corresponding to a single pixel. This process had a similar approach to the first. Instead of extracting data from a single window at the centre of each set of frames, the window was scanned in pixel increments within a set of constraints. These constraints were defined as the quarter mark and three quarters mark of the minimum width of the finger to avoid the distortion caused by the curvature of the finger. The mm/deg ratio was determined by generation and inspection of continuous strips by concatenation under manual iteration of trimming extents as shown in Figure 4.13. This ratio was subsequently used to determine the amount of overlap between sections of the individual distributions from each frame set prior to performing a weighted mix of these. The process is illustrated in Figure 4.14. Once again, the values determined from either of these techniques were mapped to the corresponding physical locations of each circumferential position as annotated during recording, thus providing discrete static and dynamic intensity maps of a lesser or greater spatial resolution.

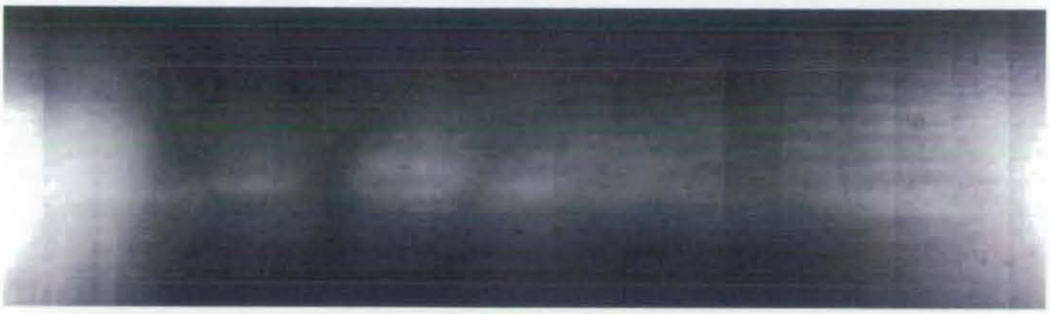

Figure 4.13 - Continuous image generated by trimming and concatenation of single frames from each set of frames.

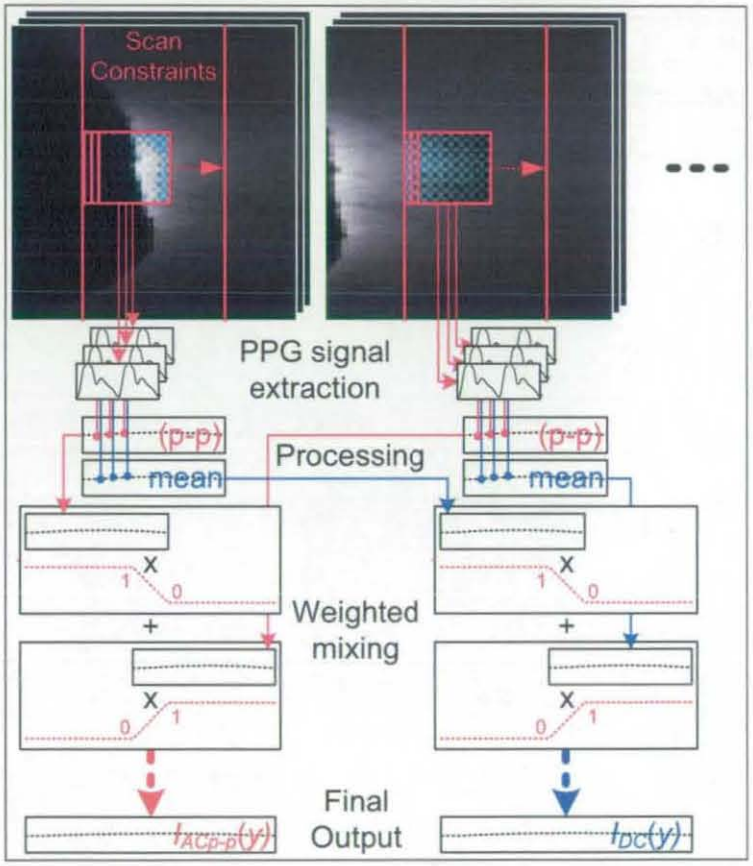

Figure 4.14 - Illustration of the generation of continuous static and dynamic intensity distributions.

4.3.3 Common Filtering and Tuning

Prior to filtering, each raw PPG signal was inspected for motion artefact spikes and trimmed if necessary. To do this, a trimmer function with a graphical user interface

was called just after generating and noise filtering each signal, giving the option to trim arbitrarily from the edges.

The range of sampling frequencies (frame rates in the case of imaging) used throughout empirical experimentation meant that it was necessary to adjust the filters used in the processing of extracted PPG signals with every change of experimental parameters. To this end, another graphical user interface was called at the start of each full dataset, allowing a manual adjustment of filter parameters. A balanced moving average filter was the choice when performing low-pass filtering for noise reduction and extraction of quasi-DC and AC components from raw PPG signals. The optimum window size for the moving average filters was determined visually on a case by case basis using the following criteria:

- For noise reduction, the window size must be such that the resultant raw signal exhibits clearly defined PPG signal characteristics and a reduction of peak-to-peak intensity limited at the point where the resultant signal maintains the mean values of the original one; and,
- For extraction of quasi-static DC components, the window size must be such that it keeps the DC signal within all peaks and troughs of the raw signal while showing negligible rippling at the frequency of the AC oscillations found in the latter.

For positive and negative AC signal envelope detection, the exponential growth and decay were chosen to result in clipping of as many peaks and troughs as possible, while constraining the clipping as close to the extremes of these as possible. Additionally, the degree of correlation between mean peak-to-peak amplitude as determined by the separation of the resultant envelopes was compared with a visual estimate of amplitude. Once the optimum filter parameters were determined, they were kept constant within all signals produced under the specific hardware configuration. This process was made possible by a set of graphical user interfaces that could be activated or bypassed by means of a flag when calling the validation processing function. The visual assessment is illustrated in Figure 4.15, and the description of the generic MATLAB GUI function caller can be seen in Figure 4.16.

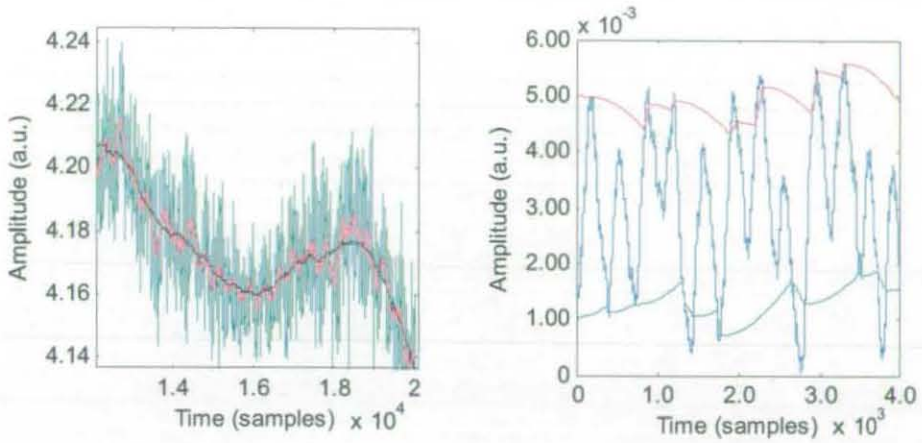

Figure 4.15 - Visual assessment of low-pass filter parameters for noise reduction and quasi-DC extraction (left) and AC envelope detection (right), both demonstrated on a particular ring sensor signal.

When processing the raw frames from the imaging platform, the visual assessment was performed on an initial pass using the simplified process that utilises a single window on the centre of each set of frames. Once an adequate set of parameters was determined, processing was performed using these on the method that generates continuous distributions as detailed in the previous section.

```
% [out,varargout]=Tweaker(funcname,vsel,in,steps,varargin)
%
% This function calls the function FUNCNAME with arbitrary inputs and
% outputs VARARGIN and VARARGOUT.  Up to 2 of the input variables in
% VARARGIN can be iterated manually by means of the cursor keys: the
% function will preview the outputs of FUNCNAME at each iteration
% until the user presses RETURN, at which point the iteration values
% are returned along with the final output of FUNCNAME.
%
% VSEL contains pointers to the inputs in VARARGIN that are to
% be iterated (max three variables)
%
% The initial values in the elements of VARARGIN pointed to by VSEL
% are stored and can be reverted to by pressing ESCAPE.
%
% STEPS contains the initial step sizes of each of these inputs
%
% OUT returns the last values used  prior to key press RETURN
%
% Example:
% [out,pos,neg]=Tweaker('Diode4',[2 3],[0.1 0.001],data,1,0.005);
```

Figure 4.16 - Help section for generic GUI function caller for iteration of arbitrary parameters.

4.3.4 Iterative Analysis Functions

The interfacing functions used to process MC data yield mean path lengths for each model layer as a function of detector position, and the validation data processing functions yield empirical DC and peak-to-peak AC distributions. At this stage, ray-trace data are ready for the post-processing phase, which consists of iteration of constrained absorption coefficients for generation and successive approximation of intensity distributions from the simulated data, with the empirical distributions as a reference.

4.3.4.1 Construction of Simulated Intensity Distributions

Iterative analysis function *IntensityMaps*, shown in Figure 4.17 overleaf, contains a set of tools that enable a process of successive approximation to a real-life representation of the system under study from the available simulated data. The core of the function generates static and dynamic intensity distributions with respect to detector position as dictated by the absorption and pulsatility coefficients passed to it from the iterative process. For each set of coefficients, optical densities at all detector positions (x,y) at each layer l are first computed:

$$OD(x,y,l) = -G.MPL(x,y,l) \times \mu_a(l), \qquad \textbf{[4.6]}$$

Where $\mu_a(l)$ is the absorption coefficient for layer l. These OD distributions are then added for all layers, and averaged along all cross-sections $(x_1:x_n)$ as generated in the interfacing phase, resulting in the effective optical density with respect to circumferential detector position (y):

$$OD_{eff}(y) = \frac{\sum_{x=x_1}^{x_n}\left(\sum_{l=1}^{11} OD(x,y,l)\right)}{n}. \qquad \textbf{[4.7]}$$

At this point, equations 3.7 and 3.8 are used to compute a static intensity map for the specific set of absorption coefficients as:

$$DC(y) = \exp\left(OD_{eff}(y)\right). \qquad \textbf{[4.8]}$$

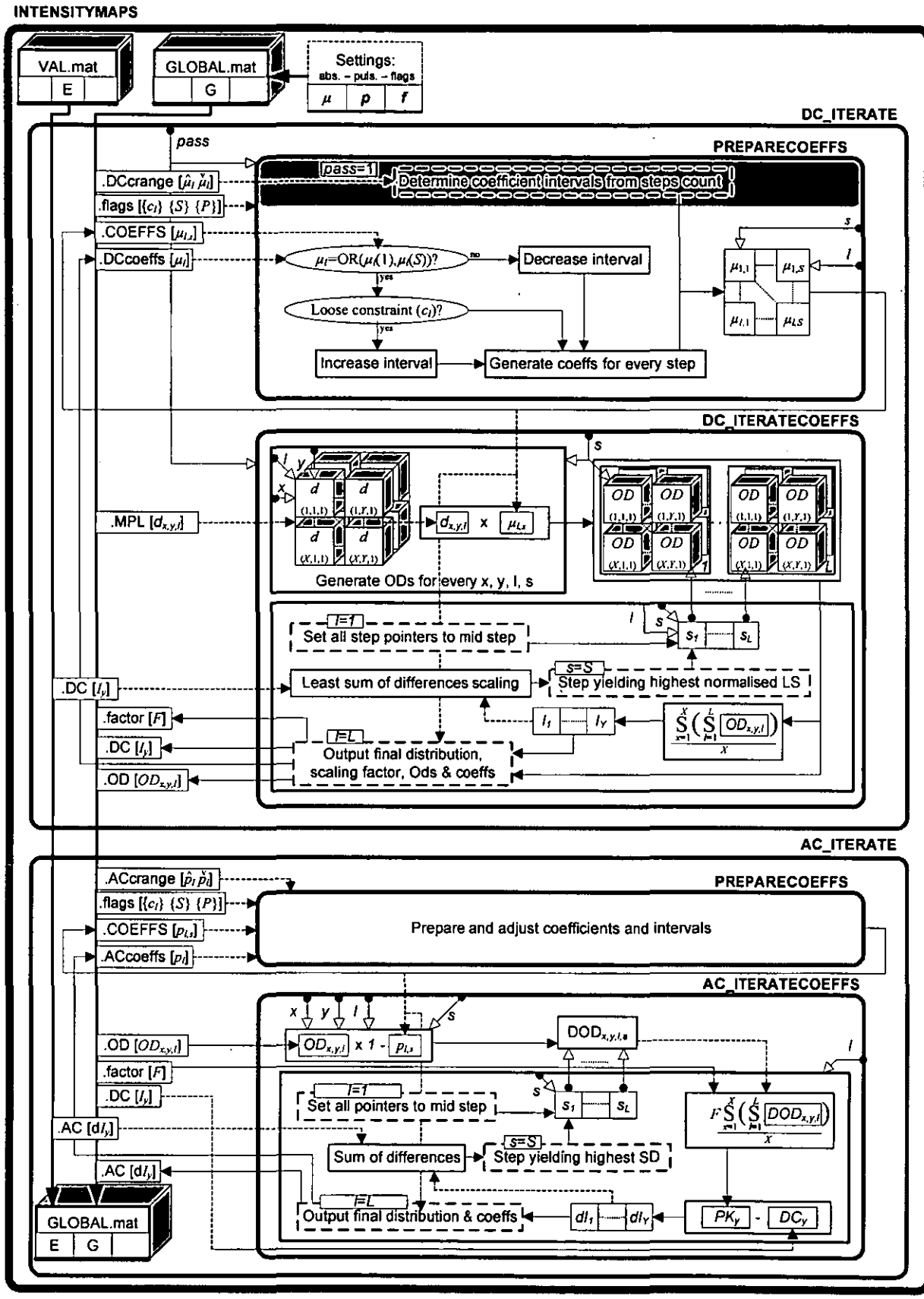

Figure 4.17 – Block diagram of iterative analysis function.

In accordance to the engineering model, optical densities for layer l vary by a proportion dictated by the pulsatility coefficient for that layer:

$$DOD(y,l) = OD(y,l) \times (1 - \rho(l)). \quad \textbf{[4.9]}$$

A proportional decrease of static optical densities as determined by pulsatility yields a corresponding peak intensity distribution:

$$PK(y) = \exp\left(\sum_{l=1}^{11} DOD(y,l)\right). \quad \textbf{[4.10]}$$

Finally, with knowledge of the mean and peak intensities at all detector positions, we are able to define the peak-to-peak dynamic intensity map for the set of absorption and pulsatility coefficients:

$$AC(y) = 2(PK(y) - DC(y)). \quad \textbf{[4.11]}$$

4.3.4.2 Iteration of Coefficients

The iterative process consists of the adjustment of a range of absorption and pulsatility coefficients until the maximum correlation is found between real and simulated intensity distributions. The process of iteration works on an initial set of constrained coefficients, each of which is submitted to an interval and an arbitrary step count that define the step size and the number of steps in either direction of these. There is an arbitrary number of iteration passes on the full set of coefficients.

Absorption coefficients are constrained according to maximum and minimum values at the corresponding wavelengths as found in the literature. Default iteration settings dictate that the coefficients be limited to these values. However, the function accepts a string of flags that essentially relax these constraints. When one of these flags is enabled and the corresponding coefficient gives a maximum correlation at a constraint, the latter is increased by a factor proportional to the range between the

maximum and minimum constraints. Lack of information with respect to pulsatility coefficients dictates that AC iterative analysis is performed unconstrained.

Each layer is iterated in turn, following a sequence which was optimised by running a high number of repetitions using randomised sequences and determining the one with highest probability of providing the highest correlation. Optical densities for each layer are replaced with the next set of them in the runtime optical density structure *OD*, the effective intensity map is produced and correlated with the empirical data, and the correlation is stored. Upon completion of each iteration pass, the set of optical densities that yielded the highest correlation is re-inserted into the runtime structure and the iteration process moves on to the next layer.

Correlation consists of a scaled least sums approach. The scaling of each resultant distribution is successively approximated until reaching a scaling factor that yields the minimum sum of absolute differences between simulated and empirical distributions. This is analogous to modification of light source intensity and therefore maintains the physical significance of the simulated distribution. The measure of least sums is determined in the following way: The difference between distributions at each point is normalised to the values of the empirical distribution, setting any values greater than 1 to 0:

$$LS(y) = \begin{cases} \dfrac{\left|DC_{val}(y) - DC_{sim}(y)\right|}{DC_{val}(y)} & \left(0 \le LS(y) \le 1\right) \\ 0 & \left(LS(y) > 1\right) \end{cases} \qquad \textbf{[4.12]}$$

The mean of these normalised absolute differences is then normalised with respect to 1 to obtain the degree of correlation between distributions,

$$C = 1 - \overline{LS(y)}. \qquad \textbf{[4.13]}$$

The process is repeated an arbitrary number of times for all layers, where the intervals of coefficients whose local optimum value was not found on the maximum or minimum iteration values were reduced to ensure a finer approximation. The result is an optimised set of static coefficients and a corresponding static intensity map. Once

the static coefficients have been approximated, the process is repeated for the dynamic ones using the optimised static map. Preliminary analysis of the iteration process proved that a high correlation of DC distributions invariably yielded an equally high correlation in AC distributions, thus justifying the approach of complete DC coefficients iteration prior to AC ones.

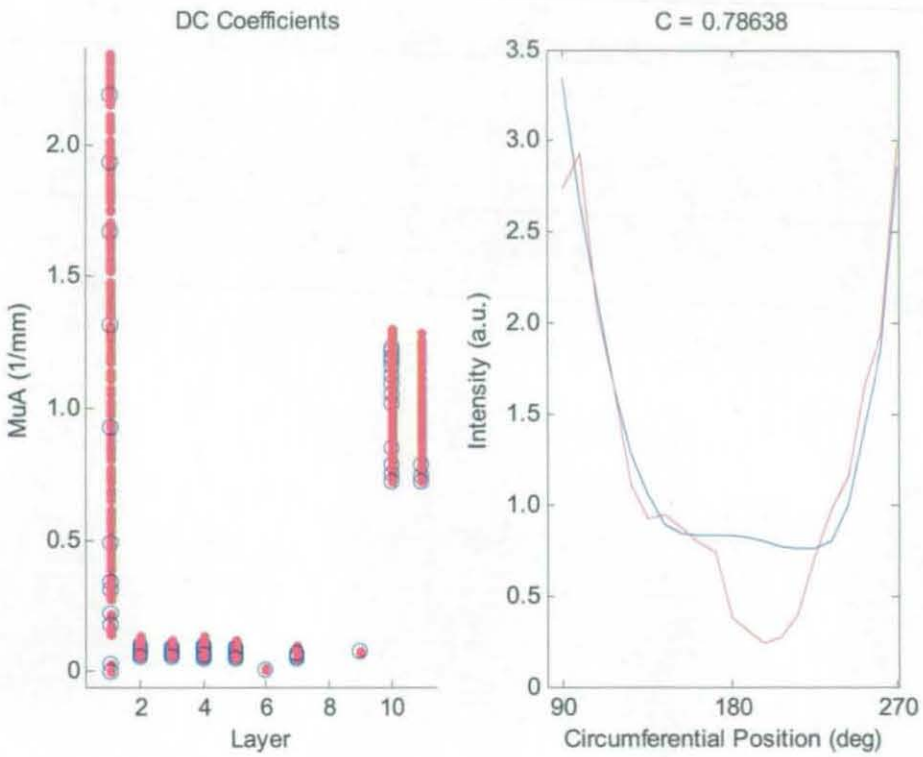

Figure 4.18 - Sample graphical output from iterative process of DC coefficients showing coefficients iteration (left) and correlation between simulated and empirical intensity distributions (right).

The resultant arbitrary settings in iterative analysis are the relaxation of constraints for selected layers and the number of iteration passes. Combinations of these settings result in a set of optimised coefficients that fall into a scale of compromise between highest fidelity to the theoretically significant ranges of coefficients as determined from the literature and the highest degree of correlation between simulation and empirical validation. The degree of correlation converges to an optimum value as the number of iteration passes increases, yielding expectedly higher values as the number of unconstrained layers increases. The significance of these settings is discussed in the following chapter, and a graphical representation of the iterative process can be seen in Figure 4.18.

This chapter has provided the key aspects of the methodology applied in this project. The structure and dataflow of the Monte Carlo simulation platform for light propagation through arbitrary geometries has been detailed along with all output data processing algorithms. The specifications of all hardware and control software used for generation of empirical data has been provided, specifically for the 1D photodiode sensor array and the 2D CMOS camera solutions. Finally, a description of all empirical data processing algorithms has been provided.

5 RESULTS

Having developed the simulation environment and the empirical validation platform, this chapter moves on to detailing the series of experiments performed with both of these. A series of preliminary distributions were generated in order to test the simulation platform. Empirical measurements performed using the ring sensor and several cameras on the rotating platform are presented and discussed, followed by the results of curve fitting by iterative analysis of correlation between the empirical distributions and those generated from the simulation environment. The chapter highlights the engineering issues encountered, as well as the degree of correlation achieved between platforms.

5.1 MONTE CARLO SIMULATION RESULTS

A series of experiments were performed on each component of the opto-physiological modelling platform. These served the purpose of elucidating flaws in the setup and engineering issues to be encountered in the experimental process. As such, they represent the initial phases of experimental protocol development.

While a range of sources contained optical properties of human tissues at 633nm, those at 850nm were scarce in the literature. A series of ratios were taken from a range of sources which allowed the derivation of coefficients at 850nm by means of scaling those at 633nm. This process aimed to ensure that the derived coefficients emulated the experimental conditions used in the determination of the readily available 633nm coefficients. Only the surface optical properties of bone were considered, namely its diffuse reflectance and transmission. MC simulation results from OptiCAD were utilised solely for tracing the ray paths as determined by the scattering coefficients, while absorption coefficients were iterated until an optimum correlation between resultant simulated distributions and reference ones from the empirical experiments was reached. The reduced scattering coefficients used to produce the simulation data and the ranges of absorption coefficients used in the iterative analysis were determined from Tuchin's review of tissue optical properties in literature[49], with the exception of some coefficients for 850nm, which were computed from relationships shown in Table 5.1.

	633 nm		850 nm		
	μ_a (mm^{-1})	μ_s' (mm^{-1})	μ_a (mm^{-1})	μ_s' (mm^{-1})	References
Epidermis	0.43-3.5	2.25	0.22-4	1.69	$\mu_{s850}' = 0.75\mu_{s633}'$[63]
Dermis	0.015-0.27	3.37	0.098-0.14	2.52	$\mu_{a850} = 0.50\mu_{a633}$[63]
Dermal plexus	0.03-0.33	3.46	0.09-0.12	2.59	
Subcutaneous fat	0.0013-0.0026	1.2	0.009-0.012	0.98	$\mu_{s850}' = 0.82\mu_{s633}'$[63]
Nerve fibre	0.04-0.06	1.8	0.075-0.08	1.7	
Muscle	0.098-0.14	0.53	0.05-0.1	0.35	
Whole blood S_aO_2=97%, hct=0.41	0.66-1.43	1.7	0.72-1.3	1.58	$\mu_{s850}' = 0.75\mu_{s633}'$[51]
	Reflection (%)	Absorption (%)	Reflection (%)	Absorption (%)	
Bone	0.54	0.22	0.54	0.18	Ugnell[64]

Table 5.1 - Absorption constraints, scattering coefficients used for MC raytraces, sources of data, and ratios used to determine the coefficients at 850 nm.

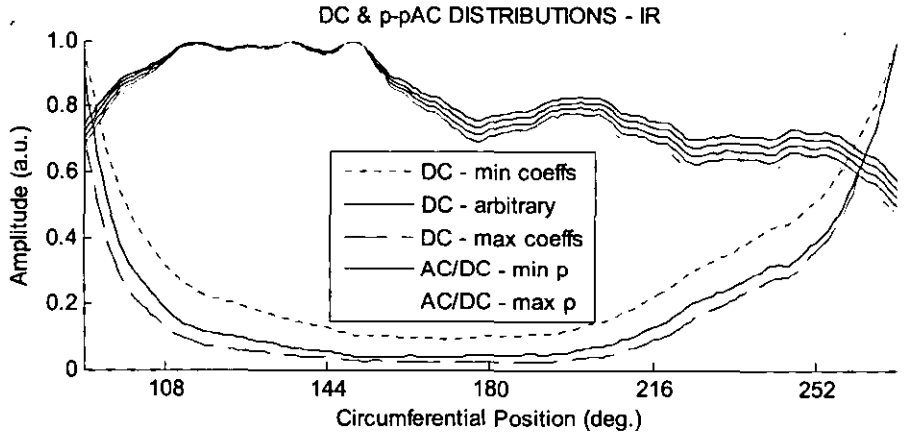

Figure 5.1 - Resultant DC distributions from minimum, arbitrary and maximum coefficients from constraints, and range of normalised AC distributions from arbitrary coefficients for IR illumination.

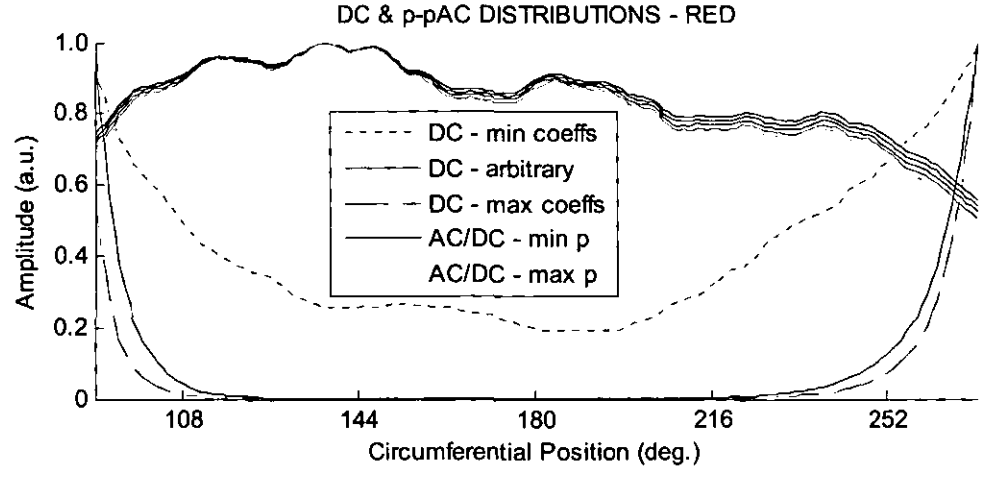

Figure 5.2 - Resultant DC distributions from minimum, arbitrary and maximum coefficients from constraints, and range of normalised AC distributions from arbitrary coefficients for red illumination.

During the course of platform development, an initial MC ray trace was attempted on the faceted finger model, with the inclusion of anisotropic scattering as defined by anisotropy factors from literature. These ray traces were abandoned before completion due to their slow convergence, and led to the decision to use reduced scattering for all coefficients. A series of preliminary outputs were produced from the virtual environment, using arbitrarily chosen coefficients. Absorption coefficients were chosen to be arbitrary values within the defined range, while pulsatility coefficients were set to 0.1% for all layers, except those for arteries which were

iterated from 1-5%; The results are shown in Figures 5.1 and 5.2. Figure 5.4 demonstrates the normalised dynamic intensity surfaces that the platform is capable of generating.

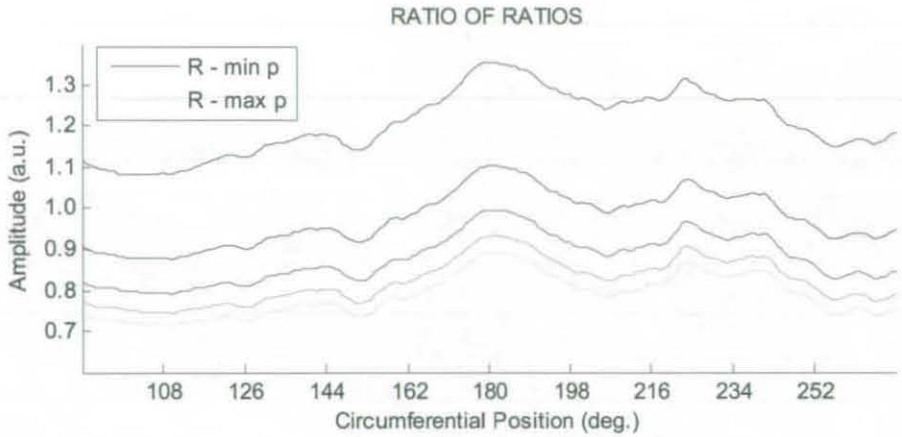

Figure 5.3 - Resultant range of *R* distributions from arbitrarily selected absorption and pulsatility coefficients.

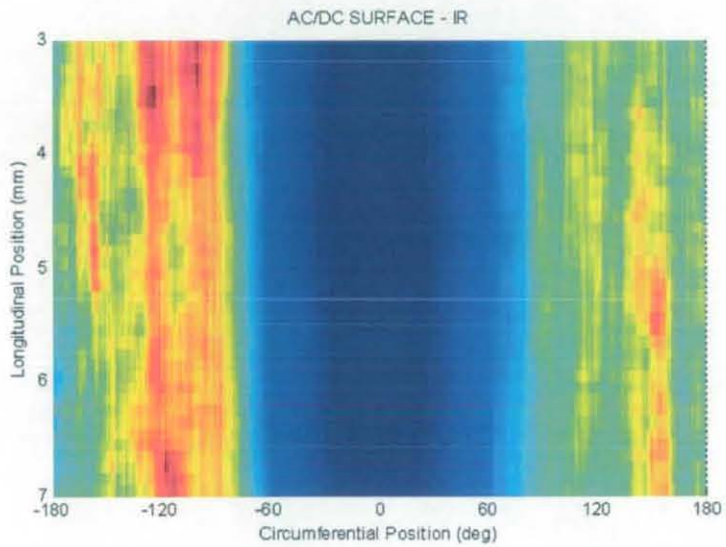

Figure 5.4 - 2D normalised AC output of virtual environment using arbitrary absorption coefficients and pulsatility defined for arteries.

5.2 EMPIRICAL MEASUREMENT RESULTS

This section details the results of tests performed with the ring sensor hardware solution to validation, followed by the results of the rotating platform solution, which was executed using three cameras of increasing capabilities.

5.2.1 Ring Sensor

The ring sensor setup was the initial hardware solution to empirical validation. The ring was closed and tightened around the finger with black insulating tape. Special care was taken in fitting the light source on the ring with opaque foam on either side to avoid direct coupling of light with the photodiodes closest to it. The subject placed their hand level with the heart and remained at rest for five minutes prior to recording. Two sets with three minutes of data each were recorded for a single wavelength.

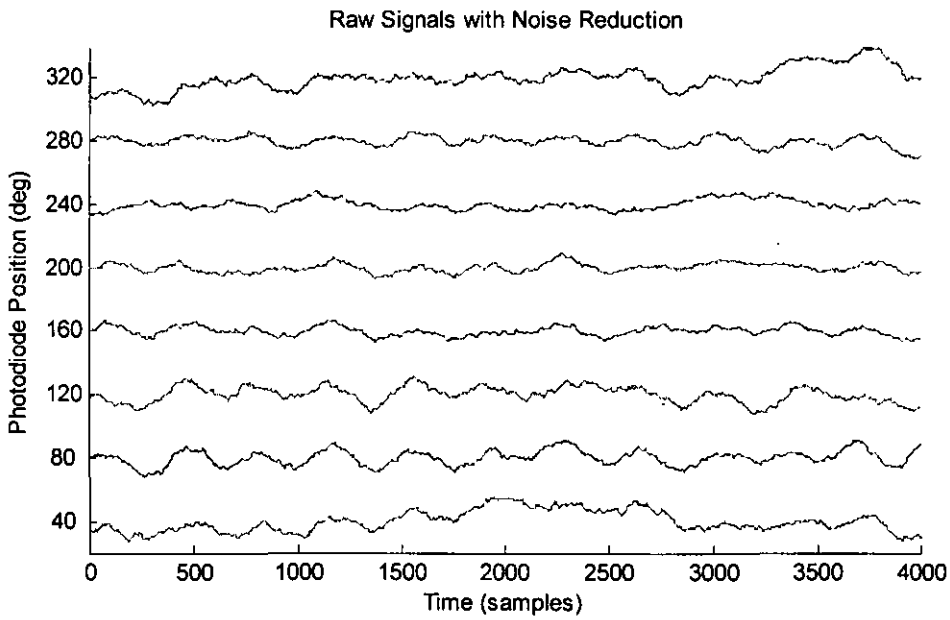

Figure 5.5 - Inspection of signal quality from raw signals of a single dataset with noise reduction.

In the case of the ring sensor, photodiode positions corresponded to the range 40° to 320° in 40° steps as dictated by the physical constraints of the probe. This limitation poses a greatly reduced characterisation of intensity distributions.

Close-up visual inspection of PPG signals in Figure 5.5 showed a reasonable signal quality, and signal peak-to-peak intensities were found to drop to a minimum at positions furthest from the light source (160° -200°) as expected. However, inspection of quasi-DC signals in Figure 5.6 reveals a non-linear effect amongst signals regardless of minimised motion artefact during recording. Signals corresponding to the photodiodes closest to the light source, heretofore referred to as lateral positions, are the most affected, indicating an insufficient reduction of direct coupling regardless of countermeasures. Correlation between the signals from remaining photodiode positions (central positions) support the assumption that quasi-static variations characterise a physiological response. Nevertheless, the corruption of the former signals indicate an instabilities in the optical coupling between detectors and the probed tissue and in the shielding for reduction of direct coupling, both of which are factors of the ring sensor design.

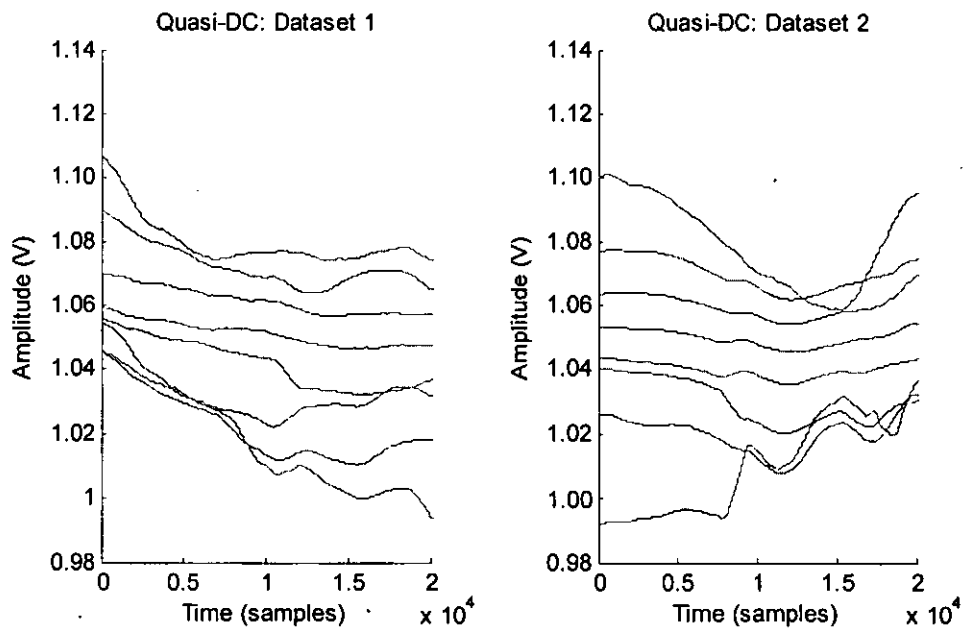

Figure 5.6 - Inspection of quasi-DC signals from both datasets, intensity-shifted so that these correspond to 40° - 320° from bottom to top.

Figure 5.7 shows the maximum, minimum and mean values of DC and peak-to-peak AC distributions, which were produced by normalising all raw signals from each dataset with respect to the maximum value of the DC distribution of each. In central positions, DC data show a sensible variability as expected from the physiological response of the subject at rest, and as a whole, these data demonstrate the ability of

the ring sensor to provide characterisation of DC levels. AC peak-to-peak data, which were smoothed to remove spikes before the determination of maxima and minima, indicates the opposite, on average showing variability greater than 100%. The two factors that would cause such an effect are unstable optical coupling and restriction of physiological pulse wave propagation due to a high enough pressure from the ring sensor.

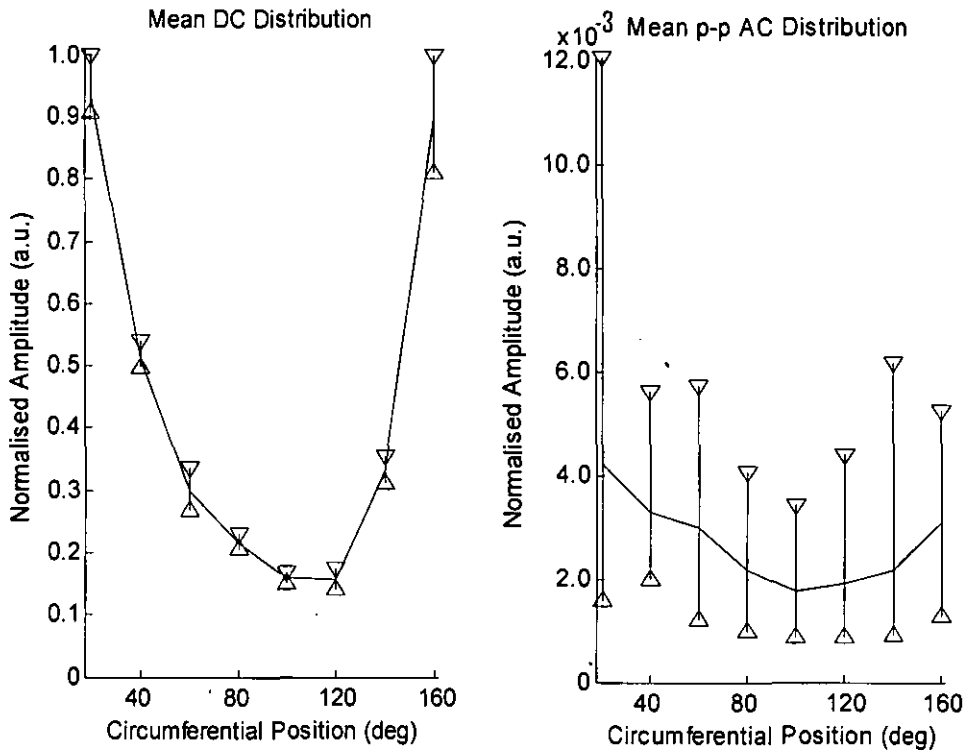

Figure 5.7 - Distribution of mean DC (left) and mean AC peak-to-peak (right) intensities with maximum and minimum values, recorded from photodiode array ring sensor.

Having shown satisfactory performance in terms of noise, it was determined that the hardware setup exhibited instability of signals due to both insufficient and irregular optical coupling between photodiodes and probing tissue. Essentially, the size of the photodiodes employed meant that they could not lay flat on the skin surface and resulted in these tilting along the curvature of the finger. The attempt to minimise this effect by tightening the ring sensor seemed to make matters worse by resulting in an unstable characterisation of dynamic physiological responses.

An assessment of requirements for an improved ring sensor design to circumvent the issues of insufficient characterisation and poor optical coupling yields the need for an increased number of smaller photodiodes. However, further preliminary studies showed that the reduction in sensing area inherent in smaller photodiodes resulted in an exacerbation of signal corruption due to motion artefact. A practicable solution to the characterisation of circumferential intensity distributions through the use of photodiodes would require the use of photodiodes with a rectangular photoactive surface, thus maximising both the robustness to motion artefact and the number of photodiodes that can be placed circumferentially. It would also require an ergonomically designed ring to house these. However, such a solution is beyond the scope of this research.

5.2.2 Rotating Imaging Platform

An essential requirement in all validation protocols was the normalisation of captured data across all positions. The ring sensor captured data from all positions simultaneously and thus circumvented this issue, but for imaging protocols the time taken to acquire data across all circumferential positions was usually more than five minutes. The subject was instructed to sit motionless for 20 minutes in order to stabilise the cardiovascular system, thus ensuring that quasi-static changes in PPG signals were kept to a minimum. The maximum size of the virtual detector window used to produce PPG signals was set to be half of the finger width in units of pixels for each data set, thus minimising the distortion that is expected from the curvature of the finger.

5.2.2.1 8 Bit Camera

The first camera used for imaging was a USB interface CMOS camera (Mightex, USA) capable of capturing 8 bit frames of size 320*240 at 60 fps. Set of 180 frames of the quoted size were captured at 37fps at every 9° step between 45° - 216°. This resulted in two sets of 90 frames for IR and red illumination at every position, each containing approximately 5 seconds of signal. The virtual detector window size was set to 46x46 pixels, corresponding to half of the finger width.

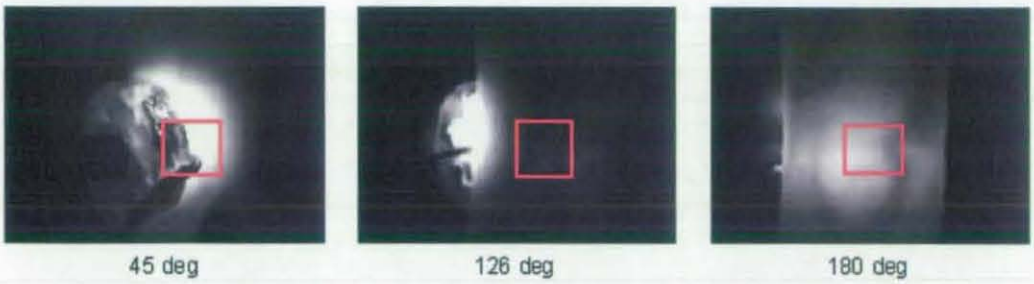

Figure 5.8 - Sample frames with illustration of analysis window, showing obstruction of measurement from light source (left) and visibility of blood vessels (middle & right)

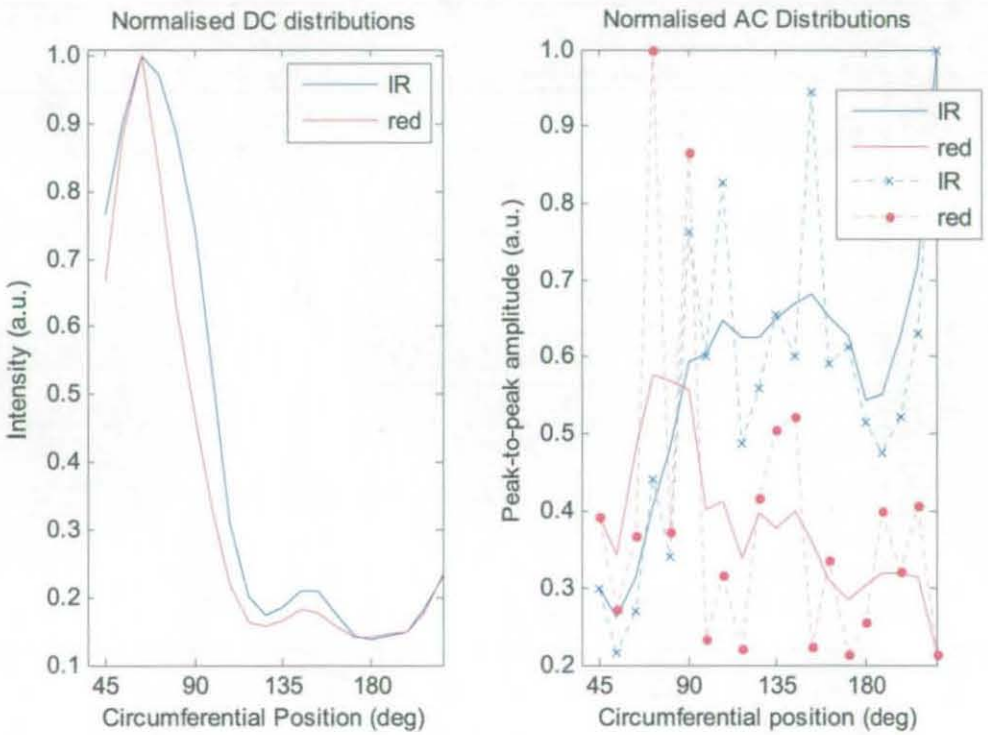

Figure 5.9 - Static (left) and dynamic (right) distributions under IR and red illumination. Smooth dynamic distributions are shown as solid lines (right).

The light source consisted of a circuit board housing arrays of four surface-mount red and IR LEDs at 633nm and 850nm, all with a 180° viewing angle. These were operated at their maximum safe operating current (30mA), and camera exposure time was increased at the expense of an acceptable loss of frame rate. Light source intensity was limited for the IR channel by adjusting the LED current so that a few of the sensor pixels saturate (I=255) at the position of highest output. This process was

not necessary for the red channel since the maximum DC values encountered were in the vicinity of I=75 regardless of the strong illumination source.

Resultant DC distributions shown in Figure 5.9 demonstrate stability by virtue of their high degree of smoothness and cross-correlation. Several features of these are significant: The distributions have a maximum value at 63° as opposed to the first position (45°) due to the reduction of mean values caused by the inclusion of frames obstructed by the light source head in the analysis window used during PPG signal extraction. Two dips can be found in the curves at 126° and 180°. These are easily explained by the relative manifestation of blood vessels with respect to position, as shown in Figure 5.8. A slight difference in response between illumination wavelengths is apparent, as expected.

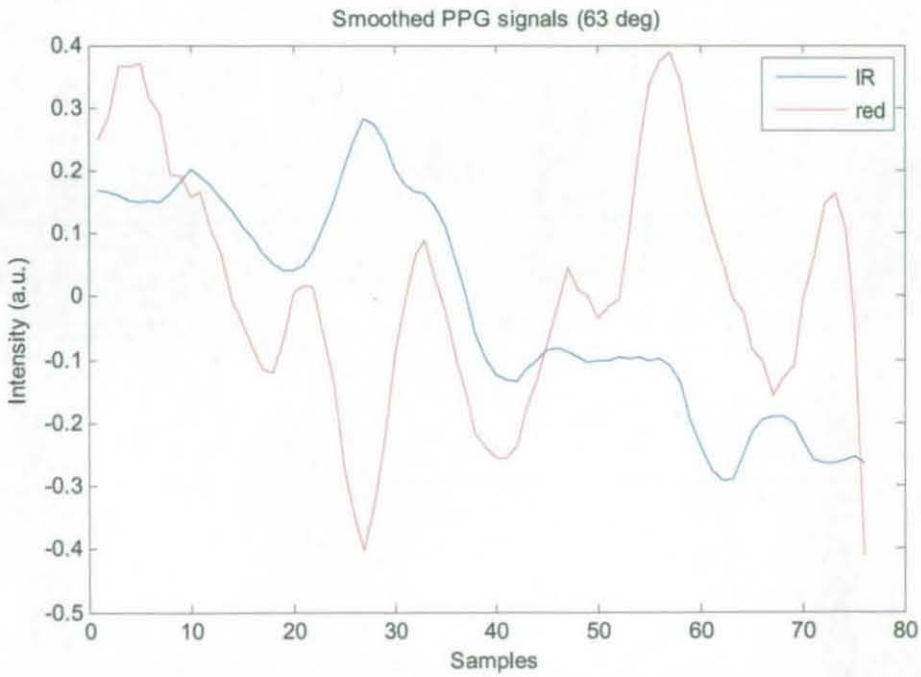

Figure 5.10 - Smoothed PPG signals from IR and red data sets corresponding to positions with highest DC.

Contrary to the DC data, AC responses shown in Figure 5.9 show a low cross-correlation and a high variability, although the dips seen in DC distributions can be appreciated in the corresponding positions. Inspection of PPG signals in Figure 5.10 reveal an insignificant correlation (0.3) between IR and red signals at the position of highest DC intensity, where the quality of signals is best in theory. AC signal

amplitudes are seen to correspond to ±0.2-0.5 of a sensor amplitude level, which means that significant quantisation takes place. In spite of this, relatively constant peak-to-peak amplitudes and periods are apparent amongst the signals thanks to the averaging that takes place in the signal extraction process. Nevertheless, it is expected that sensor noise has a similar range and can therefore corrupt the signals beyond recognition.

5.2.2.2 10 Bit Camera

The next camera used was a Cameralink interface high-speed CMOS camera (Mikrotron, Germany) capable of capturing 10 bit frames of size 1024*768 at 300 fps. Sets of 200 frames were captured at 40 fps for each illumination wavelength at every 9° step between 90° and 270°, which, after discarding the first two data sets due to obstruction of the camera's line of sight, yielded sets between 108° and 270°. In addition to the 20 minute resting period of the subject prior to recording, the acquisition of each set of frames was manually triggered at times where the AC/DC ratio as provided by a standard pulse oximetry probe was within an arbitrary range determined during the rest period.

In this experiment, red and IR were recorded in two separate sessions to allow a higher frame rate per channel. The light source consisted of single red and IR surface-mount LEDs at 633nm and 850nm respectively, both with a 180° viewing angle. Each of these was placed in turn with no housing on the standard position found in commercial transmission-mode pulse oximetry probes. Due to the relatively high frame rate used, exposure time was limited, and consequently, the maximum safe operating current for the LEDs yielded maximum DC values at approximately 50% and 15% of the sensor's full dynamic range for IR and red respectively.

Initially, a virtual window size of 20x20 pixels was used to extract a single PPG signal from each set of frames. Visual inspection of these showed a consistently high quality across all signals. For subsequent analysis, the optimum window size was determined by assessing the quality of PPG signals produced from the frame sequence at 180° under red illumination. It can be seen from Figure 5.11 that a window size of 6x6 pixels yielded a signal that shows minimal distortion and consistent peak-to-peak intensity with respect to signals from larger window sizes. Having produced these

signals from the frame sequence with lowest DC intensity, it is safe to assume that a window size of 6x6 pixels will yield minimal distortion, if any, from all other positions.

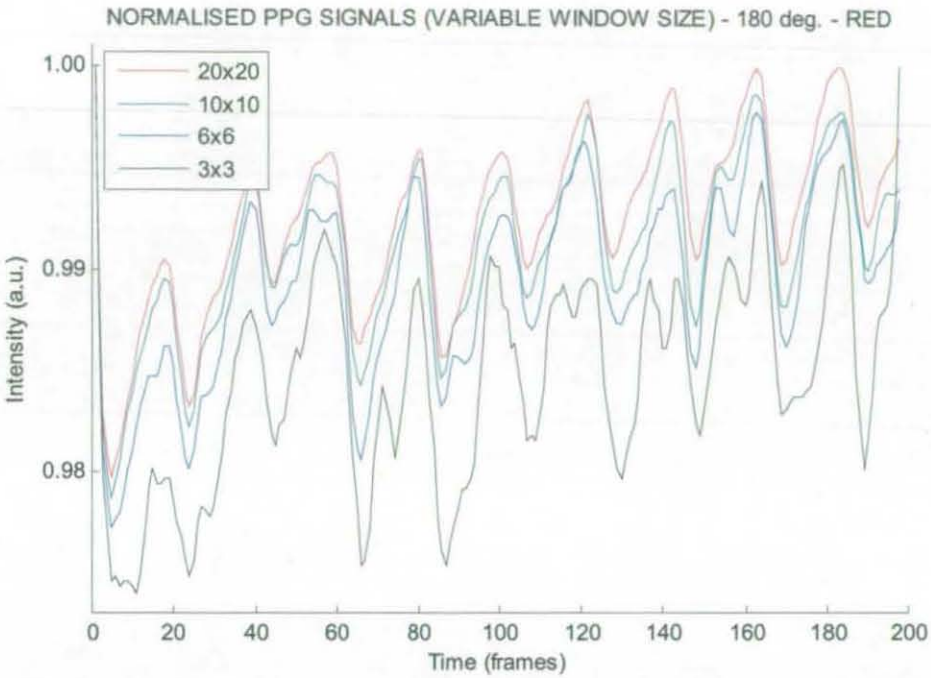

Figure 5.11 - PPG signals generated with variable window sizes from 180 deg. position under red illumination.

Analysis of Figure 5.12 demonstrates a high degree of response characterisation. High correlation between corresponding distributions at different wavelengths is indicative of the reliability of these responses, as is a high inverse correlation between the static and normalised dynamic distributions. The latter inverse relationship is expected since responses in the vicinity of blood vessels will demonstrate both a higher absorption of light and a higher variability in absorption due to the concentration of blood in these. Comparative analysis of Figures 5.12 and 5.13 confirms this further, also demonstrating a fine spatial characterisation thanks to a reduced virtual window size. A smoother response from red illumination is apparent both numerically and visually, as would be expected from a higher degree of optical diffusion. This is substantiated by the fact that the scattering coefficients of all relevant human tissue types under red illumination are notably higher than those corresponding to IR. Ratio of ratios distribution shows a high variability of ±0.3 in the central positions. Also, an offset is visible between both static and dynamic

responses with respect to illumination wavelength. This is evidence of variations in light source and finger positions due to individual recording sessions for each wavelength.

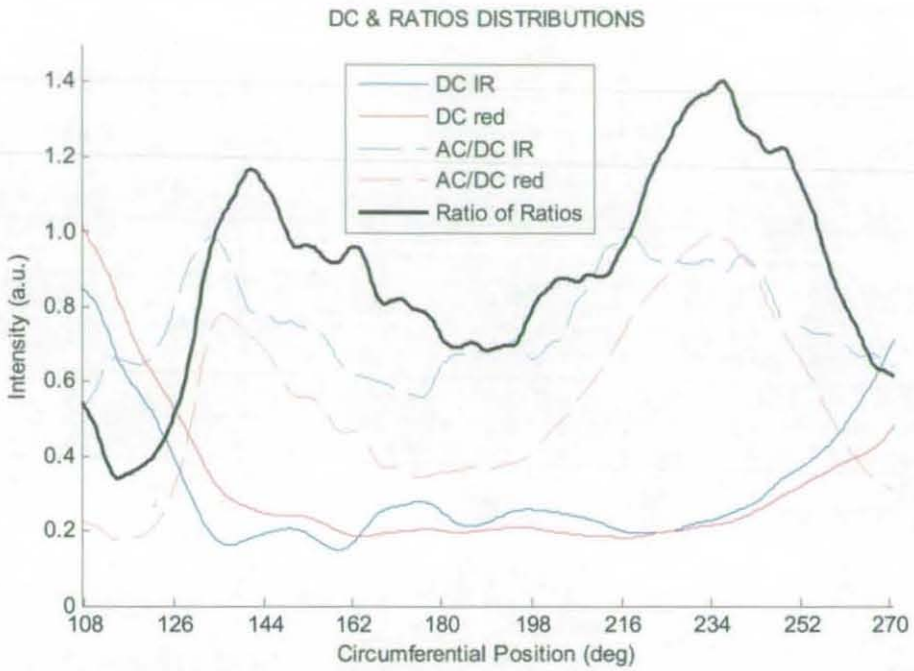

Figure 5.12 - DC and DC normalised peak-to-peak AC distributions from 10 bit camera data sweep with window of size 6x6 pixels.

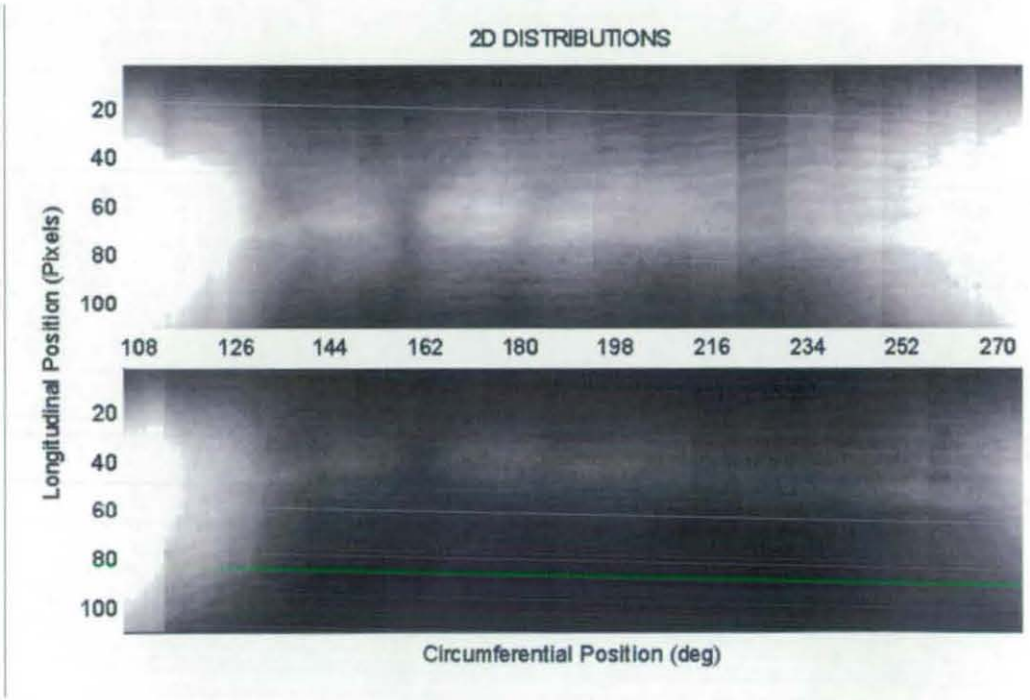

Figure 5.13 - Concatenated strips of images from all circumferential positions for IR (top) and red (bottom) data.

5.2.2.3 12 Bit Camera – Recording Session 1

For the last hardware setup, a CCD camera (Hamamatsu Photonics, Japan) was used, capable of capturing 12 bit frames of size 2048*128 at 50 fps. Two separate recording sessions were performed under this setup.

The resultant experimental protocol dictated that 90 frames be captured at 30fps at every 9° step in the range 45° - 325°. This resulted in sets of 45 frames at 15fps for each of the two illumination wavelengths at each circumferential position. In this experiment, the process was repeated for four positions of the subject's hand at different heights with respect to the subject's heart. The first position had the subject's hand above head level, as high as the experimental platform allowed. The second and third hand positions were just above and below heart level, and the last position had the subject's arm fully extended downwards. The light source consisted of two surface-mount resonant cavity LEDs (RCLEDs, Weltek co. Ltd., Taiwan) at wavelengths 650nm and 870nm, mounted inside an ergonomic housing. The intensities of these were set to almost saturate the camera sensor at the position yielding the highest mean intensity.

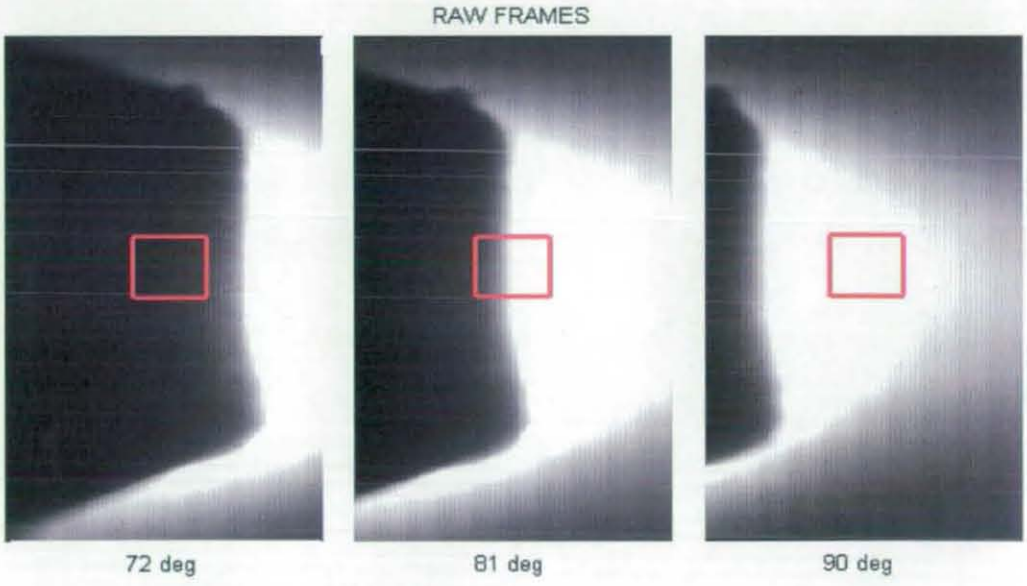

Figure 5.14 - Sample frames from positions 72° - 90° with analysis window

The setup included simultaneous measurement from a standard transmission-mode pulse oximetry probe (Viamed, UK) placed on a finger of the hand undergoing

measurement, together with a digital signal representing the capture periods for each camera position. Analysis was performed on a window of 10x10 pixels, centred with respect to finger width and light-source longitudinal position. PPG signals showed negligible change with respect to window size, reflecting a high spatial stability due to the increased bit rate.

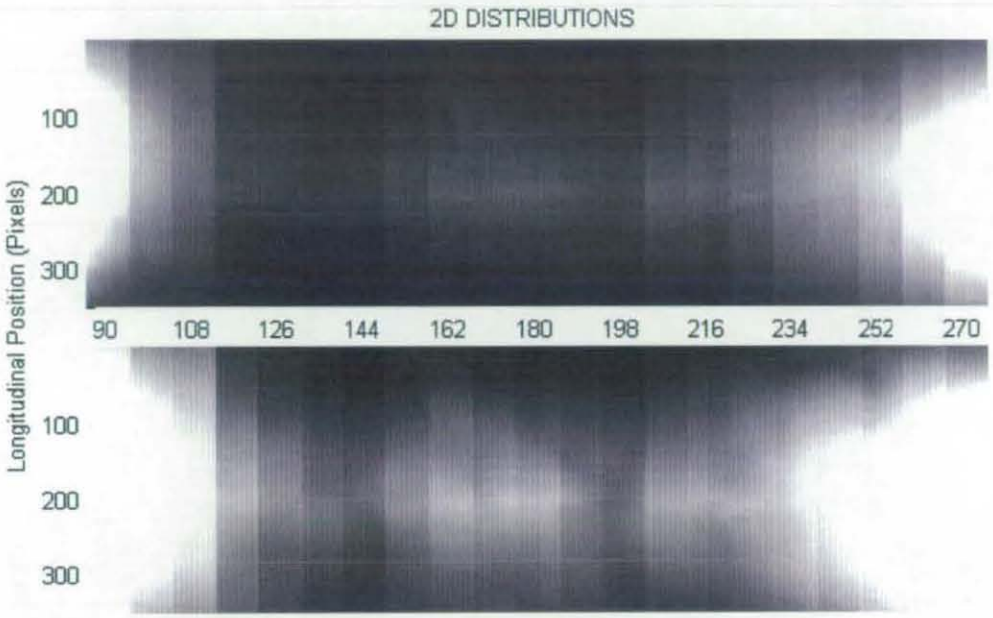

Figure 5.15 - Concatenated strips of images from positions 90° - 270° for IR (top) and red (bottom) datasets.

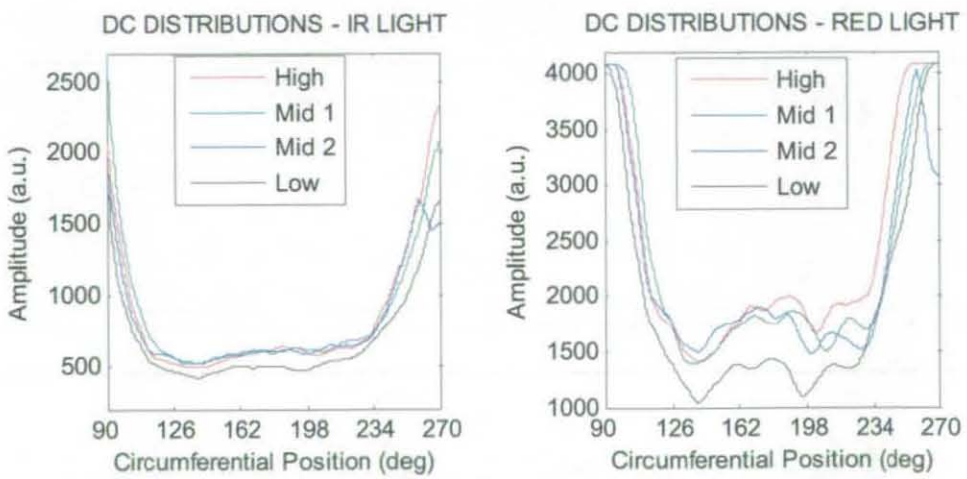

Figure 5.16 - Static (DC) distributions from four hand heights under IR (left) and red (right) illumination

Inspection of raw data showed that, despite improvements in the light source design aimed towards reducing direct coupling while maintaining high a visibility range, it remained a challenging task to gather useful data in positions less than 90° from the light source. Figure 5.14 shows how the light source housing obstructed the probing surface of the analysis window for positions below 90°. Consequently, raw data was trimmed to the 90° - 270° range.

DC distributions in Figure 5.16 show a well defined intensity range reflecting a response from variable venous blood pooling. A sudden intensity drop is evidenced in the last positions of data corresponding to the *mid2* position, most likely due to an obstruction from cabling. The DC responses under red illumination show a clear saturation at the first and last two positions closest to the light source, due to an improper calibration of light source currents at the start of recording. This is reflected as a drop to zero in the corresponding positions in the AC distributions, as can be seen in Figure 5.17. The absence of dichrotic notches in the PPG signals of Figure 5.18 demonstrates a lack of temporal definition in these. However, their smoothness, together with their high correlation between channels indicates that the time characterisation of peak-to-peak responses is reliable. Nevertheless, dynamic responses generally show a lack of correlation in terms of hand position; the variability encountered in peak-to-peak amplitudes suggests the presence of significant motion artefact, most likely arising from an enhanced sensitivity to optical coupling due to the characteristics of the RCLEDs.

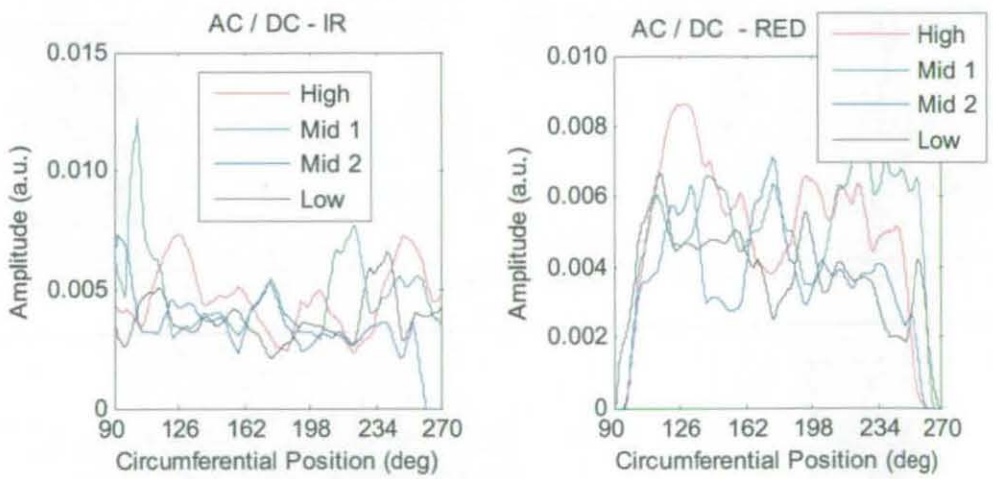

Figure 5.17 - Distributions of peak-to-peak dynamic amplitudes for IR (left) and red (right) illumination.

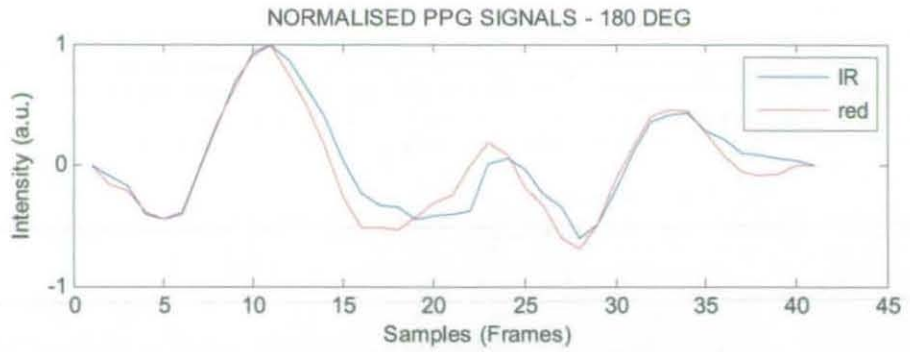

Figure 5.18 - PPG signals for lowest intensity position (180 °).

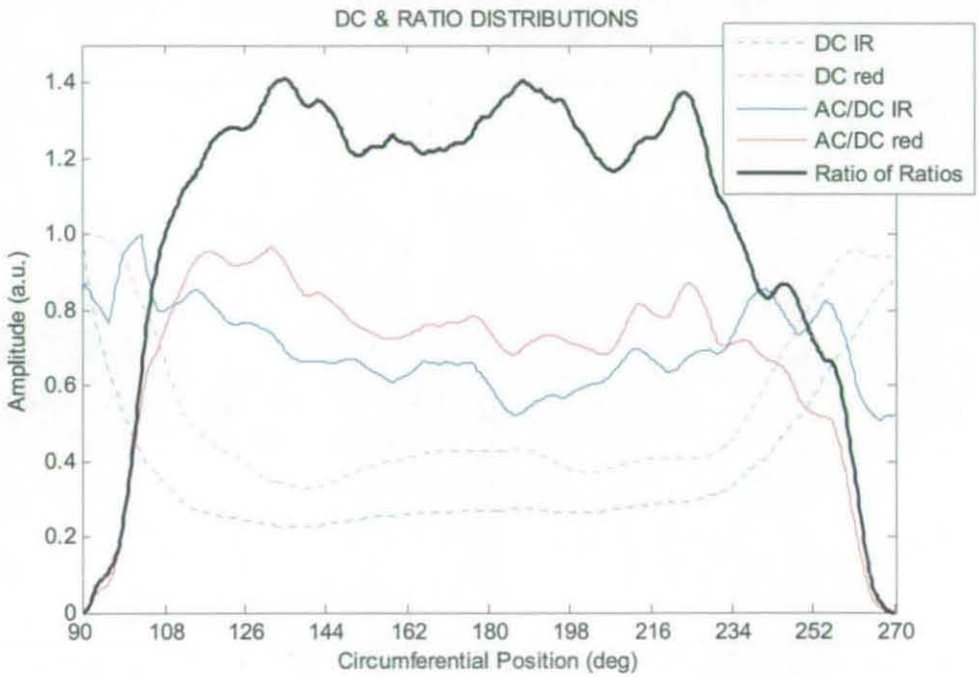

Figure 5.19 - Normalised mean DC and peak-to-peak AC/DC distributions for all hand positions, and ratio of ratios from these in bold.

Regardless of poor dynamic characterisation, Figure 5.19 shows that the ratio of ratios in the range 117° - 243° is stable with a variation of ±0.1, showing peaks corresponding to positions of blood vessels. The drops at positions closest to the light source reflect the loss of dynamic signals due to saturation of the red channel.

5.2.2.4 12 Bit Camera - Recording Session 2

. The experimental protocol was modified to capture separate sets of 60 frames for each wavelength at 20fps at every 9° step in the range 90° - 270°. The two sets of frames for each position were captured one after the other, thus maintaining the physiological conditions as close a possible for the source wavelengths. The process was repeated for three positions of the subject's hand—high, medium, and low—as opposed to the four positions of the previous session. The middle hand position was just below heart level. Additionally, the whole process was repeated in reverse, starting from 270° at the low hand position and ending at 90° at the high hand position. The light source utilised the same RCLEDs as before, where its housing was made more absorptive by covering it with black insulating tape and the LEDs were covered with a white diffusion filter to reduce the sensitivity to optical coupling. The intensities of these were set at a safe distance from saturation of the camera sensor at the position yielding the highest mean intensity in order to account for unexpected rises in light transmission due to motion. The pressure applied by the light source housing was increased in an attempt to minimise signal corruption due to motion artefact. As dictated by window size optimisation, analysis was performed using a window of 15x15 pixels, centred with respect to finger width and light-source longitudinal position.

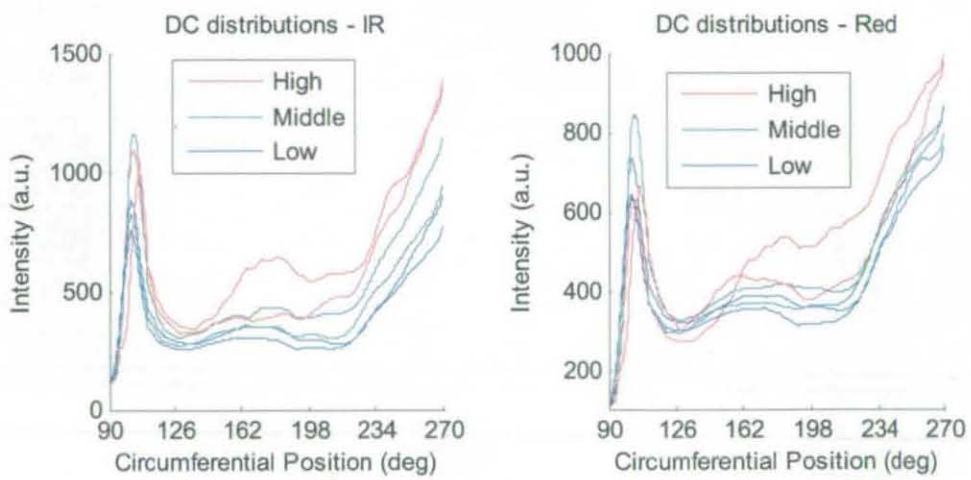

Figure 5.20 - Two pass static (DC) distributions from three hand heights under IR (left) and red (right) illumination

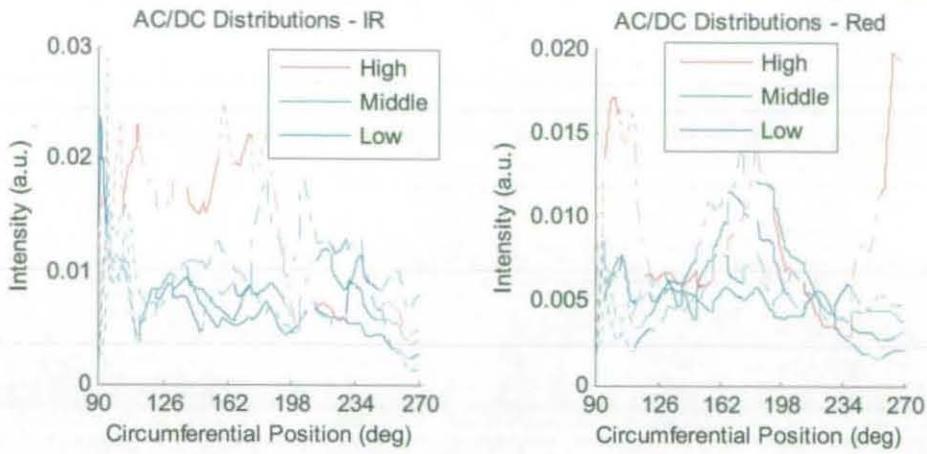

Figure 5.21 - Normalised dynamic (AC/DC) distributions from three hand heights under IR (left) and red (right) illumination, where solid and dotted segments represent clean and distorted PPG signals respectively.

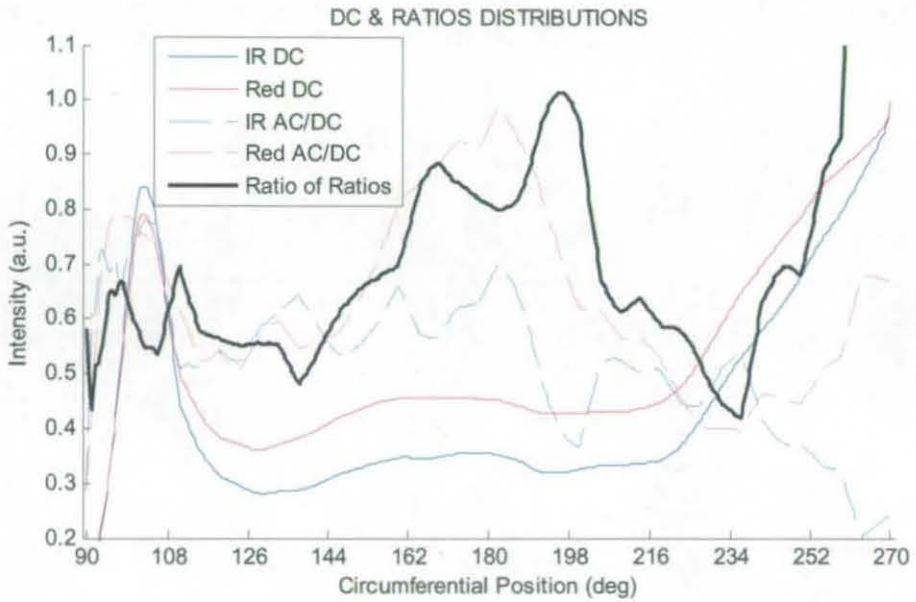

Figure 5.22 - Normalised mean DC and peak-to-peak AC/DC distributions, and ratio of ratios from these in bold.

Initial inspection of all DC distributions shown in Figure 5.20 evidences a skewing of the forward pass at the high hand position, most likely due to the subject's arm increasingly weighing down as a consequence of fatigue. Although present, this skewing effect can be seen to decrease in intensity at lower positions. This suggests that extra care is to be taken to ensure the comfort of the patient, and that it is possible to attain a more symmetric response. Finally, the commonly encountered effect of light source housing obstruction can be seen at 90°, clearly aggravated by the

increased pressure of the housing against the finger. It follows that the best course of action is to remove all data from the high forward pass and all 90° data from further analysis. A mean distribution was subsequently determined for each wavelength from the remaining high pass distribution and the means of the middle and low pass distributions. Figure 5.21 shows the AC distributions remaining after the removal of data after DC analysis, where the PPG signals corresponding to all positions in these were manually inspected and given an assessment (dotted line = severely corrupted signal, dash-dot line = mildly corrupted signal, solid line = clean signal). Resultant AC distributions shown in Figure 5.22 reflect the level of corruption, although the correlation between IR and red distributions does provide evidence of features. Nevertheless, the ratio of ratios distribution shows some instability.

5.2.2.5 12 Bit Camera – Repeatability Study

The comparative results from single subject experiments helped to determine the optimal hardware settings and experimental protocol for further empirical validation studies. At this stage, a further study was performed in order to test the repeatability and robustness of the rotating imaging platform with respect to multiple subjects.

For this study, 10 subjects were selected by merit of whether the platform could yield signals with minimal motion artefact from their left index finger. This limitation was a function of finger size, where only average-sized fingers were small enough to fit in the support structure without cutting off the circulation to the finger while fitting tightly enough to minimise motion artefact and optical coupling of the light source. The resultant subjects were aged 20-50 years old and all had average-sized fingers. Each subject stood with their arm fully extended downwards to yield the lowest possible hand position with respect to their heart. Two camera passes were performed on each subject, with a two minute resting period in between. A single pass consisted of camera positions from 90-270 in 9 steps. Five seconds worth of frames were recorded at 35 fps for each step, at a frame size of 200 x 128 pixels, under red and IR illumination at every other frame.

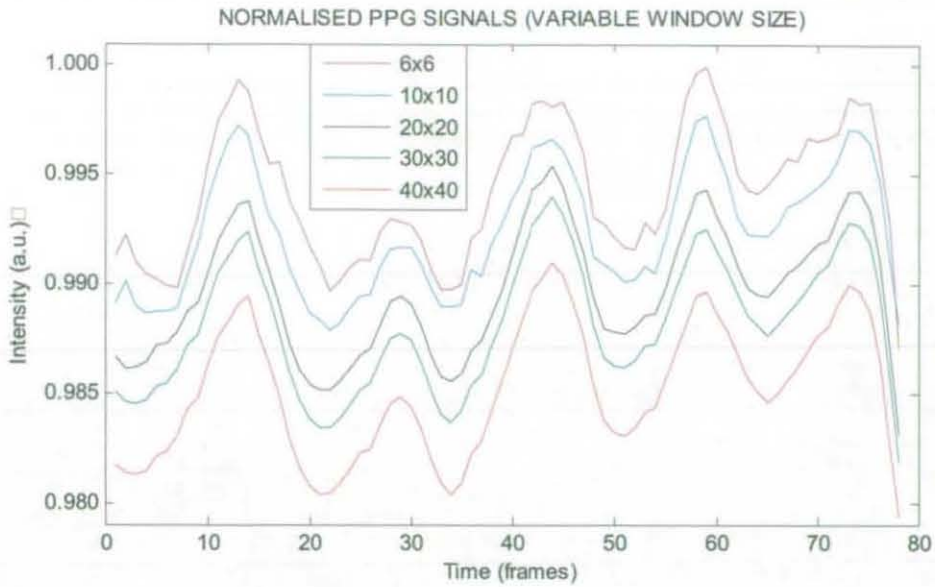

Figure 5.23 - PPG signals generated with variable window sizes from 180 deg. position under IR illumination, chosen from raw data with the best overall signal quality.

The raw output of the experiment detailed above consisted of two sets of 80 frames for both light source wavelengths, for each of 21 positions in each of two passes performed on each of 10 subjects. Continuous static and dynamic intensity distributions were generated for each pass in the raw data, and the distributions from the passes with highest overall signal quality were in turn used to generate normalised dynamic intensity (ratio) and ratio of ratios distributions. Signals were extracted from raw data using a window size of 20 x 20 pixels as dictated by the window size optimisation illustrated in Figure 5.23.

Subject	Inter-λ		Inter-set		Inter-subject	
	set 1	set 2	DC	AC	AC/DC	R
1	0.96	0.80	0.98	0.90	0.20	0.22
2	0.87	0.81	0.99	0.76	0.02	-0.39
3	0.83	0.74	0.96	0.85	0.22	0.19
4	0.75	0.68	0.96	0.20	-0.25	0.11
5	0.90	0.69	0.97	0.72	0.21	0.37
6	0.92	0.79	0.99	0.99	0.32	0.22
7	0.85	0.66	1.00	0.96	0.32	0.27
8	0.92	0.78	0.99	0.85	-0.06	0.29
9	0.86	0.64	0.95	0.83	0.21	0.05
10	0.93	0.77	1.00	0.87	0.27	0.08
Mean	0.88	0.73	0.98	0.79	0.14	0.14

Table 5.2 – Results for inter-wavelength and inter-set correlation analyses for assessment of quality and same-subject repeatability.

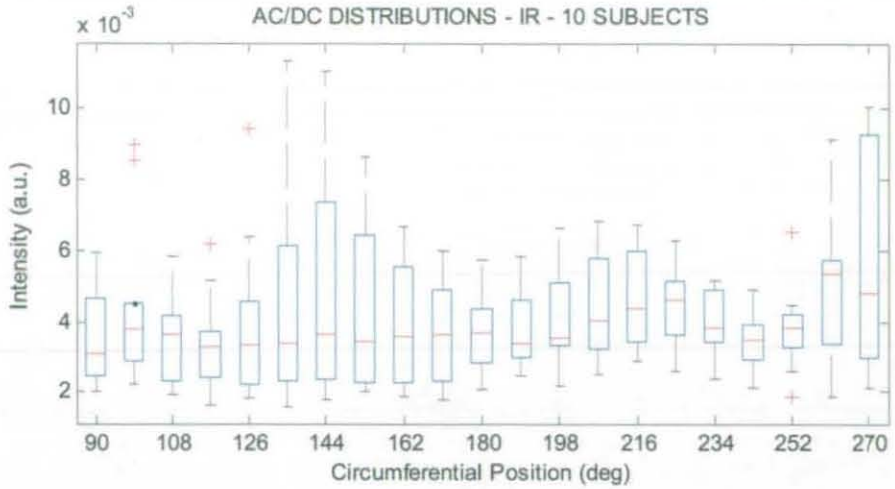

Figure 5.24 – Box & whisker plot of IR ratio distributions for all subjects

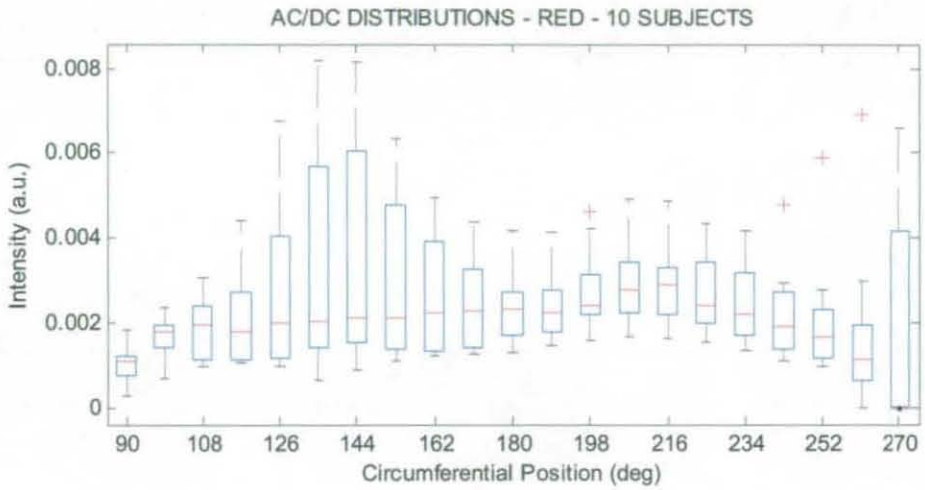

Figure 5.25 – Box & whisker plot of red ratio distributions for all subjects

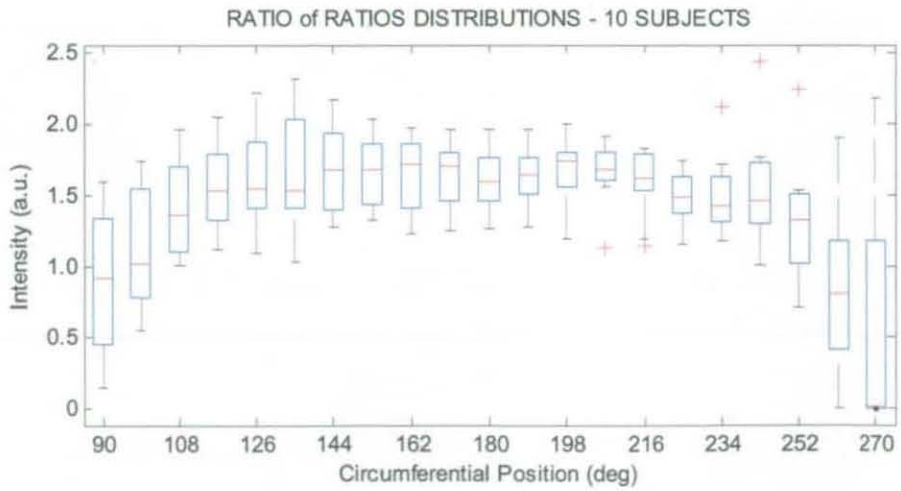

Figure 5.26 – Box & whisker plot of ratio of ratios distributions for all subjects

Several correlative analyses were performed on the raw experimental data sets, the results of which can be found in Table 5.2. The first of these aimed to determine the overall signal quality of each individual pass by determining the average correlation coefficient between red and IR signals extracted from each camera position. Results indicate a lower signal quality in all second passes with respect to first passes and a high overall signal quality in first passes (mean cross-correlation of 0.88), indicating an effect related to subject fatigue. The second analysis provides a measure of same-subject repeatability and an additional measure of signal quality by performing a cross-correlation of corresponding static and dynamic intensity distributions between the two passes of each subject. The results in Table 5.2 show a correlation with this analysis and the previous one, demonstrating the inherent quality assessment of this stage. The analysis shows high overall subject repeatability, where the reliability of DC distributions expectedly shows little dependency to signal quality and the reliability of AC distributions can vary significantly due to the high sensitivity to optical coupling between light source and tissue.

The final analysis considers inter-subject repeatability by determining the correlation and the variability between ratio and ratio of ratios distributions across all subjects. Specific correlation coefficients in Table 5.2 are calculated by taking the mean of cross-correlations of the distribution in question with the corresponding distributions of all remaining subjects. In the case of ratio distributions, the mean is also taken for both wavelengths. Results show little correlation between ratio distributions of subjects. This is attributed to both physiological variability between subjects and to the inherent difficulty in normalising the venous system for across subjects when using the experimental apparatus. The box and whisker plots for ratio distributions shown in Figures 5.24 and 5.25 reflect this variability but demonstrate similar inter-wavelength characteristics.

5.2.2.6 12 Bit Camera – Two-Dimensional Maps

A series of 2-dimensional distributions were produced in order to investigate the imaging capability of the empirical platform. The set of frames from a single subject in the repeatability study was used for this process. A window size of 20 x 20 pixels was used as determined in the analysis shown in Figure 5.23.

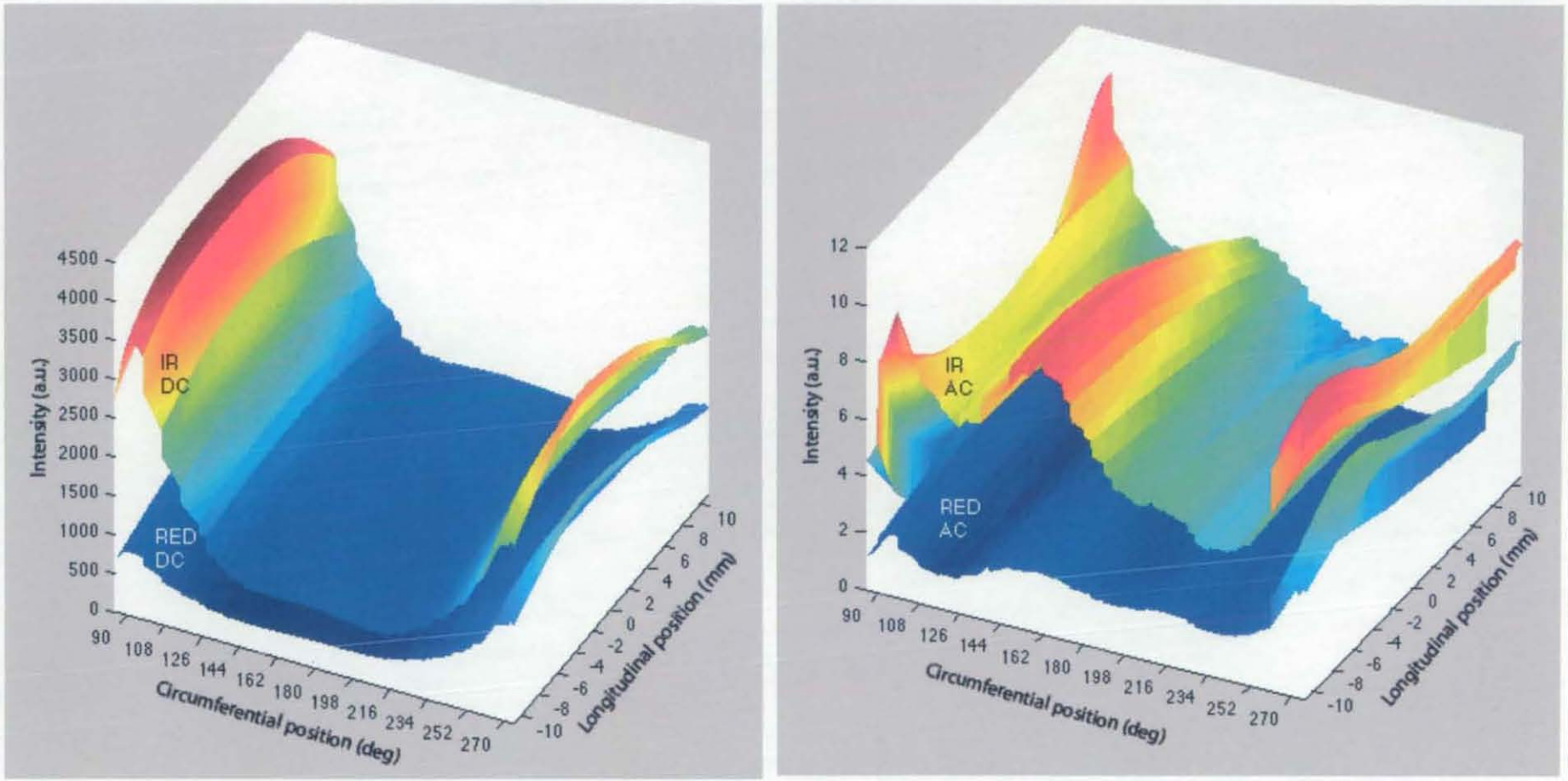

Figure 5.27 – Two-dimensional static (left) and dynamic (right) intensity maps for a single subject.

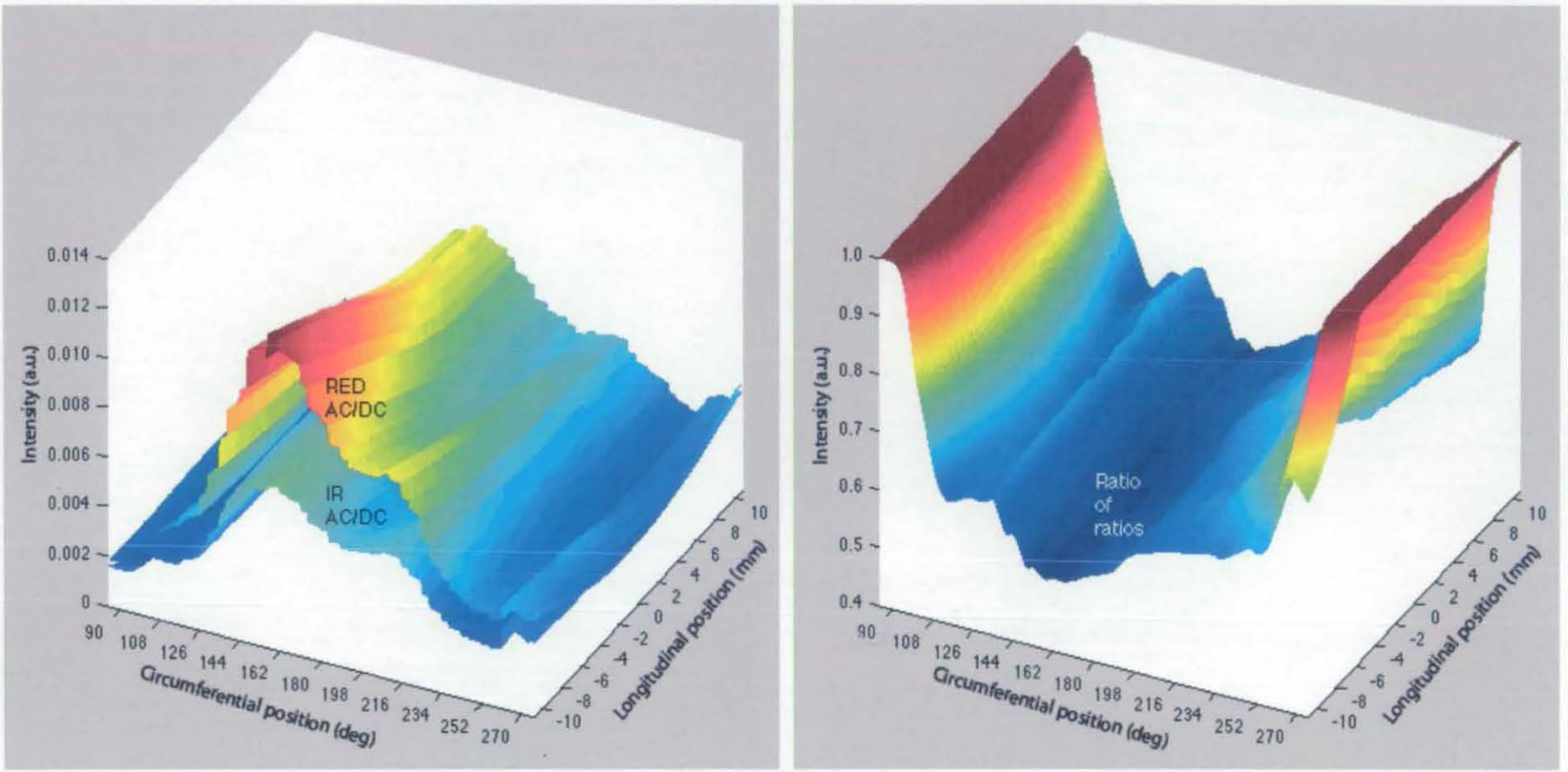

Figure 5.28 – Two-dimensional normalised dynamic intensity (left) and ratio of ratios (right) maps for a single subject.

Figure 5.27 shows the 2D static and dynamic intensity maps, where a curvature along the longitudinal axis with a peak corresponding to the light source position is evident, and where a clear loss of signal quality can be appreciated at the circumferential positions closest to the light source. The normalised dynamic intensity maps in Figure 5.28 suggest an increase in dynamic signal strength when detecting at longitudinal positions which are offset from light source position towards the tip of the finger. Finally, the ratio of ratios map in Figure 5.28 shows a very high stability with respect to longitudinal position.

5.3 ITERATIVE ANALYSIS RESULTS

Findings from the assessment of quality of empirical measurements shown in the previous section are one of the factors which determine the validity of results from the iterative analysis. Empirical results show evidence of variability due to artefacts, and potential areas of improvement in the data acquisition platform. Nevertheless, a high degree of characterisation is evident throughout these results. Iterative analysis was performed on two sets of empirical distributions, namely those produced from the images captured with the 10 bit camera and the second set of results produced from 12 bit camera images. Analysis was performed fully on DC distributions before moving on to AC distributions.

5.3.1 10 Bit Camera Distributions

The wavelengths of LEDS (RS Components, UK) used in the light source for empirical measurements using the 10 bit camera were 633nm and 850nm, which coincide with those of the scattering and absorption coefficients used in the simulation. A high correlation can thus be expected between simulation and validation distributions. These distributions, shown in Figure 5.29, were trimmed to the range 99° - 261° in order to remove the effects of light source housing obstruction and were reversed in order to increase the correlation.

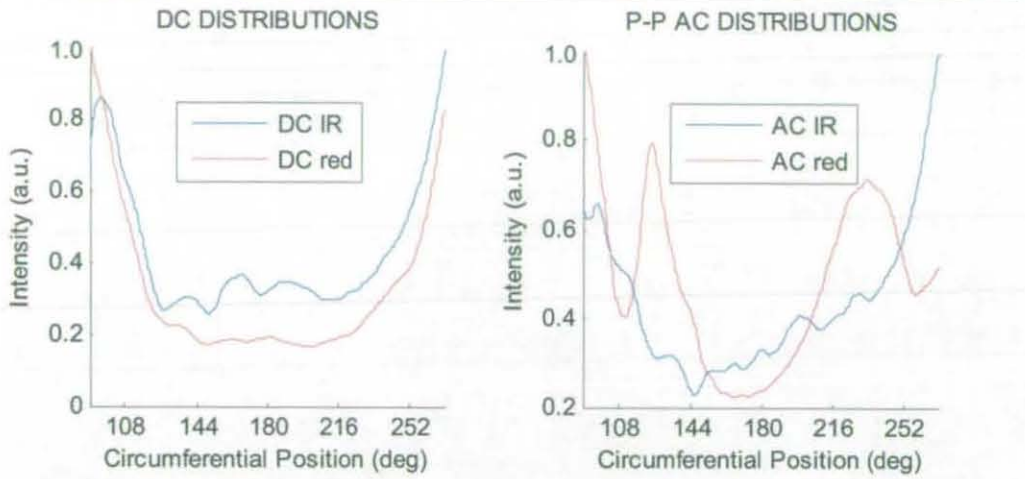

Figure 5.29 - Normalised DC and peak-to-peak AC distributions from 10 bit data set used in iterative analysis.

5.3.1.1 Absorption Coefficients

Iterative analysis was initially performed on DC distributions using unconstrained coefficients, using a variable number of coefficient iteration passes from 1 to 30. Figure 5.30 shows the normalised sum of differences between simulated and empirical DC distributions and the quality assessment of coefficients with respect to number of iteration passes. For the latter assessment, coefficients get a score of 1 if within their constraints and zero otherwise, and the mean of these scores is taken. Red distributions consistently score better than IR ones in both aspects of the analysis, indicating that the absorption and scattering coefficients of the former generally provide a more faithful representation. Correlations of distributions can be seen to converge at above 0.8 for iteration pass counts over 15, with maximum values of 0.88 and 0.93 for IR and red light respectively. Coefficient qualities stabilise at pass counts above 10 after a sharp drop at low counts, showing three coefficients converging within constraints for red and a single coefficient cyclically falling within constraints for IR. It is concluded that a pass count of 20 is a reasonable pass count and is consequently used for constrained coefficient iterative analysis.

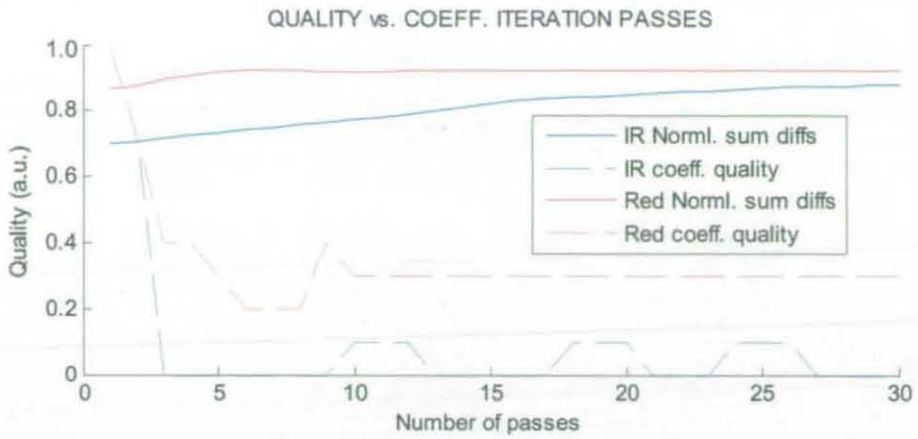

Figure 5.30 – Assessment of distributions correlation and coefficients quality, where correlation is assessed by normalised sum of differences and coefficient quality is assessed by these being within constraints.

Iterative analysis using individually unconstrained coefficients follows. Resultant normalised sums of differences ranged from 0.71 to 0.76 for IR light and from 0.87 to 0.91 for red light distributions. The results from fully constrained coefficients yielded the lowest correlation in IR distributions, and an average correlation in red distributions, demonstrating lower and higher qualities respectively. The highest correlations in both channels resulted from unconstrained coefficients for plexus profundus, deep dermis, arteries and veins. The resultant DC distributions can be seen in Figure 5.31.

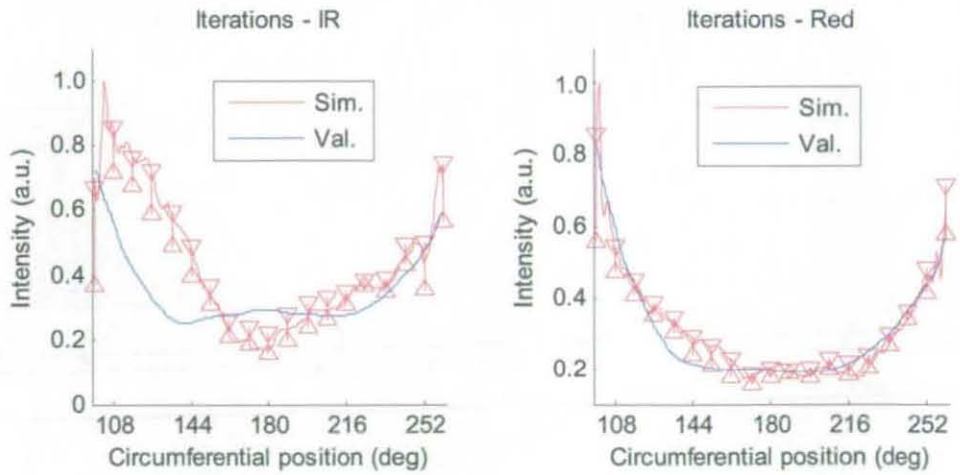

Figure 5.31 - Normalised sums of differences of empirical validation (val.) DCs and simulation (sim.) DCs for IR (left) and red (right) illumination, where simulation curves show the results of iterative analysis with constrained coefficients and ranges represent the maximum and minimum values from single unconstrained coefficients.

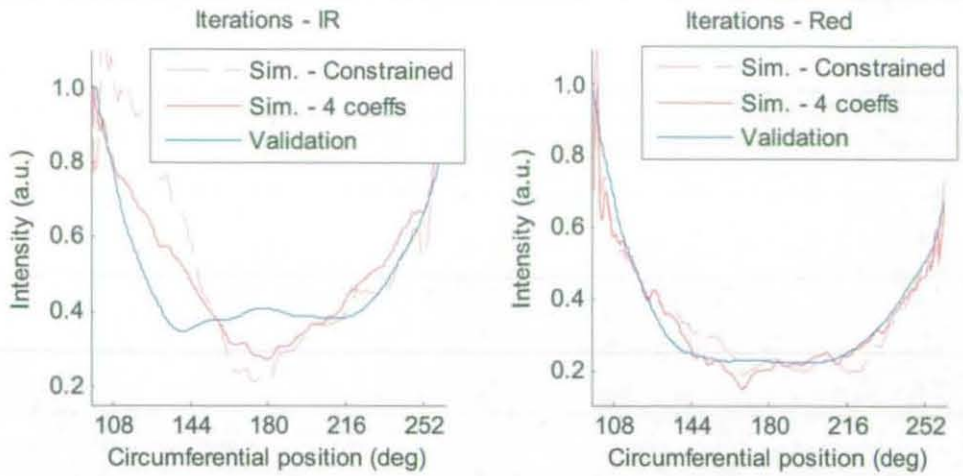

Figure 5.32 - Normalised sums of differences of empirical validation DCs and simulation DCs for IR (left) and red (right) illumination, showing the results of iterative analysis with constrained coefficients in dashed and unconstrained ones of plexus profundus, deep dermis, arteries and veins in solid lines.

Adhering to these findings, the next iterative analysis was performed with the coefficients of mentioned layers unconstrained. These yielded normalised sums of differences of 0.84 and 0.92 respectively for IR and red illumination. Unconstrained iterative analysis yielded correlations that were higher by 0.1-0.4, therefore it was concluded that this level of compromise between quality of coefficients and distribution correlation was ideal.

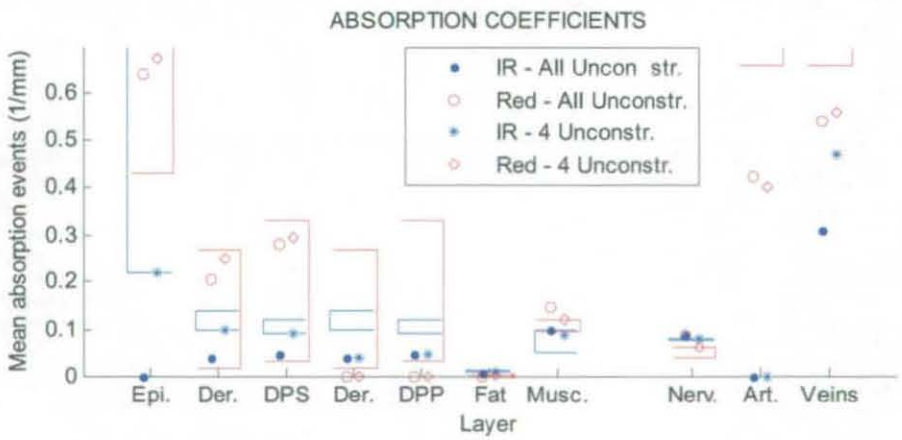

Figure 5.33 - Absorption coefficients and corresponding constraints for IR and red, for iterative analysis with unconstrained coefficients and with deep dermis, plexus profundus, arteries and veins coefficients unconstrained.

The resultant absorption coefficients with respect to their constraints, together with the coefficients that result from a 20-pass completely unconstrained iterative analysis

can be seen in Figure 5.33. The similarity between these sets of coefficients demonstrates a reliable convergence that is due to the high correlation between distributions. In addition, practically all coefficients converge within or close to constraints, thus demonstrating the high reliability of these.

5.3.1.2 Pulsatility Coefficients

Iterative analysis for dynamic distributions is performed using unconstrained coefficients. Pulsatility coefficients, which can be seen in Figure 5.34, have abnormally high values and little correlation between channels. However it can also be seen that values converge, with none reaching the upper constraint, and all coefficients at zero correspond to absorption coefficients having diverged to zero, with the exception of the IR coefficient for nerves. The analysis yielded normalised sums of differences of 0.85 and 0.83 for IR and red light respectively, and the resultant distributions are compared with empirical ones in Figure 5.35.

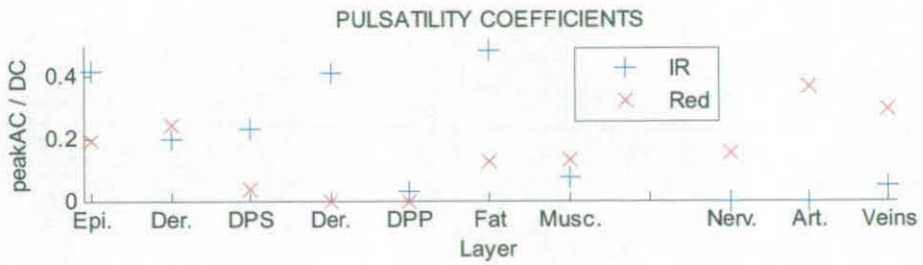

Figure 5.34 - AC coefficients for IR (left) and red (right) illumination after unconstrained iterative analysis.

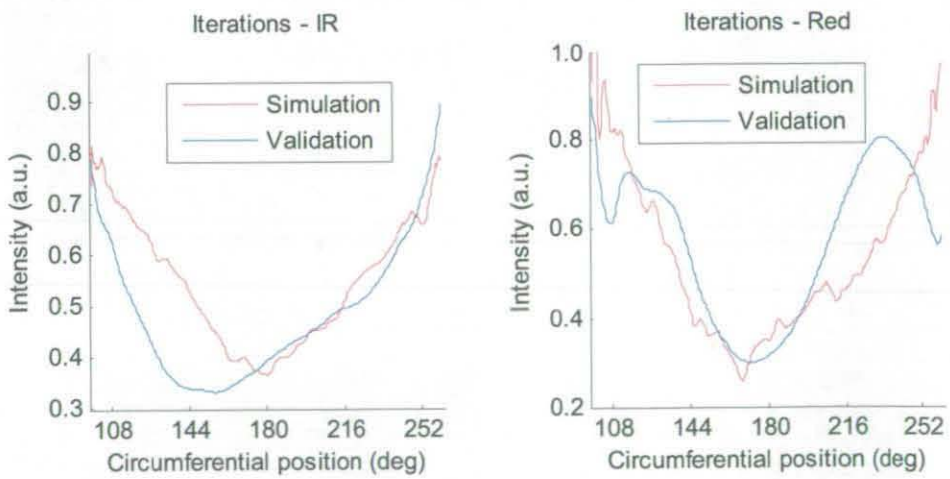

Figure 5.35 - AC distributions for IR (left) and red (right) illumination after unconstrained iterative analysis.

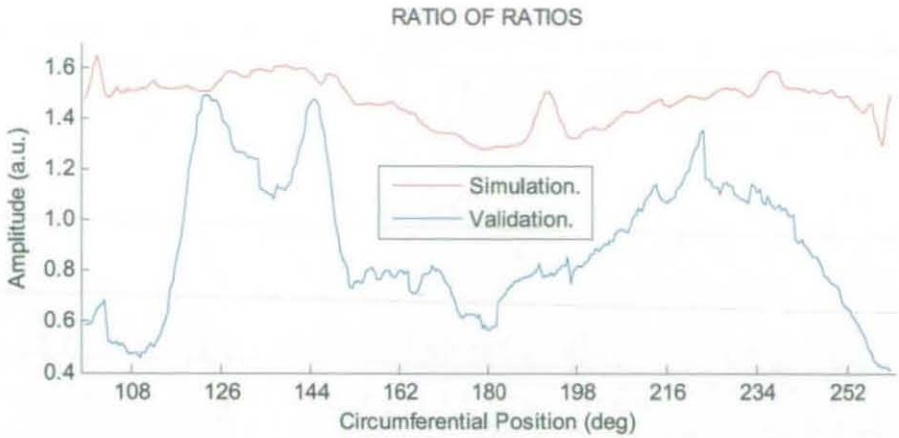

Figure 5.36 - Comparative plot of empirical and simulated ratio of ratios distributions.

Dynamic distributions can be seen to have shapes that are very similar to their static counterparts as is to be expected, since any sequence of equivalent pulsatility coefficients would yield identical shapes. However, a notable degree of deformation towards adaptation to the empirical dynamic distributions is also evident. The AC iterative analysis process thus shows how distinct dynamic contributions of layers can, to some extent, lead to specific dynamic distributions. The ratio of ratios distribution produced from the use of the static and dynamic distributions from iterative analysis is compared with that of validation in Figure 5.36.

5.3.2 12 Bit Camera Distributions

The second set of 12 bit camera results proved to be the most faithful characterisation of static and dynamic responses achieved thus far and was therefore selected to be used for the following validation process of the virtual environment. The corresponding distributions, shown in Figure 5.37, were trimmed to the range 99° - 261° in order to remove the effects of light source housing obstruction. In this case, the empirical distributions were produced using a light source at 650nm and 870nm, differing from those used in simulation by 20-30nm.

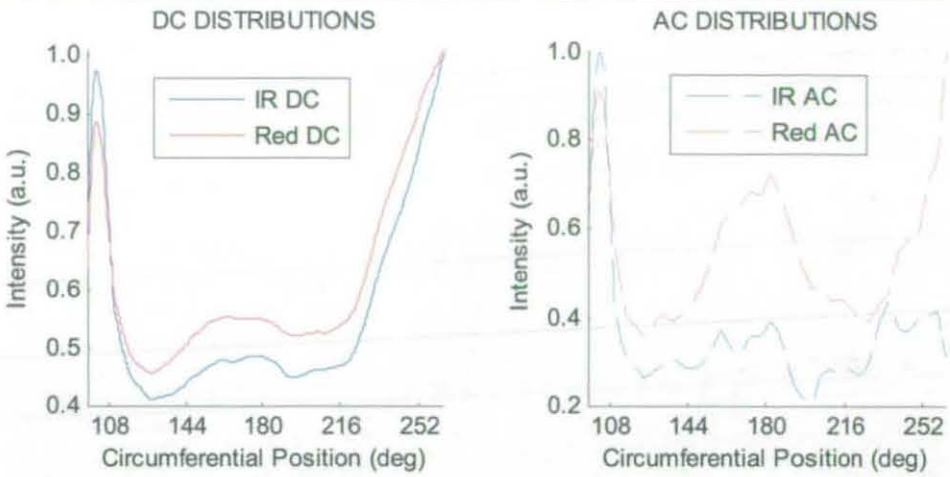

Figure 5.37 - Normalised DC and peak-to-peak AC distributions from data set selected for iterative analysis.

5.3.2.1 Absorption Coefficients

Iterative analysis was initially performed on DC distributions using unconstrained coefficients, using a variable number of coefficient iteration passes from 1 to 30. Figure 5.38 shows the normalised sum of differences between simulated and empirical DC distributions and the quality assessment of coefficients with respect to number of iteration passes. For the latter assessment, coefficients get a score of 1 if within their constraints and zero otherwise, and the mean of these scores is taken.

Red light distributions consistently score better than IR ones in both aspects of the analysis, indicating that the absorption and scattering coefficients of the former generally provide a more faithful representation. Correlations of distributions can be seen to converge at around 0.8 for iteration pass counts over 15, with maximum values of 0.86 and 0.88 for IR and red respectively. Coefficient qualities show stability at pass counts above 10 after a sharp drop at low counts and a transient peak at 20. It is concluded that the latter is the optimum pass count and is consequently used for constrained coefficient iterative analysis.

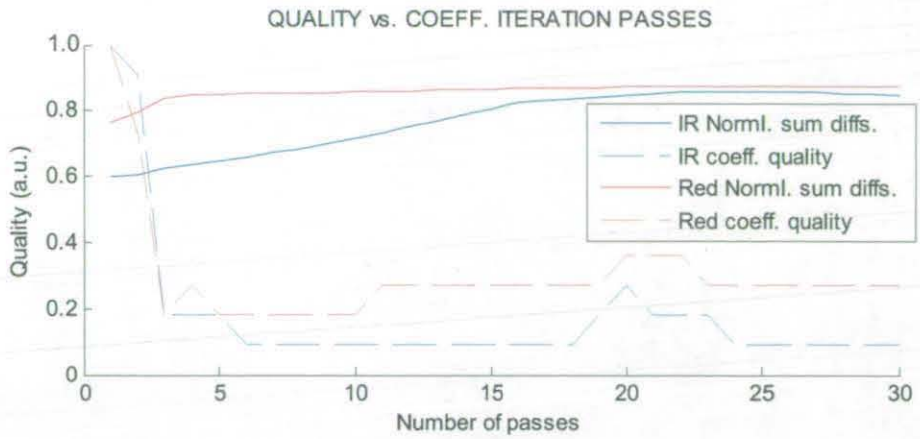

Figure 5.38 - Assessment of distributions correlation and coefficients quality, where correlation is assessed by normalised sum of differences and coefficient quality is assessed by these being within constraints.

Iterative analysis using individually unconstrained coefficients follows. Resultant normalised sums of differences ranged from 0.81 to 0.83 for IR and from 0.79 to 0.83 for red light distributions, where results from fully constrained coefficients yielded the lowest correlations in comparison. The highest correlations resulted from unconstrained coefficients for veins, arteries and epidermis. The resultant DC distributions can be seen in Figure 5.39.

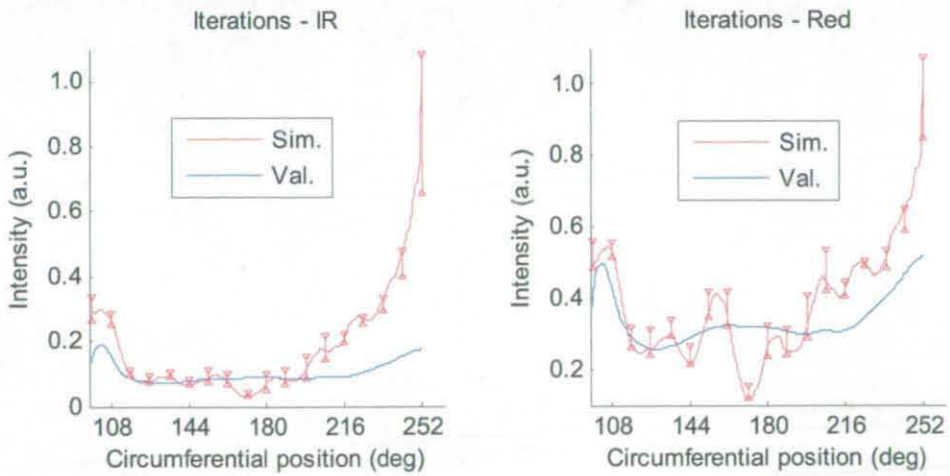

Figure 5.39 - Normalised sums of differences of empirical validation DCs and simulation DCs for IR (left) and red (right) illumination, where simulation curves show the results of iterative analysis with constrained coefficients and ranges represent the maximum and minimum values from single unconstrained coefficients.

Adhering to these findings, the next iterative analysis was performed with coefficients for arteries and veins, and epidermis unconstrained. These yielded normalised sums

of differences of 0.83 and 0.86 respectively for both IR and red light illumination, demonstrating an increased sensitivity to the absorption coefficient of epidermis. Unconstrained iterative analysis yielded correlations higher by 0.2-0.3, therefore it was concluded that this level of compromise between quality of coefficients and distribution correlation was ideal.

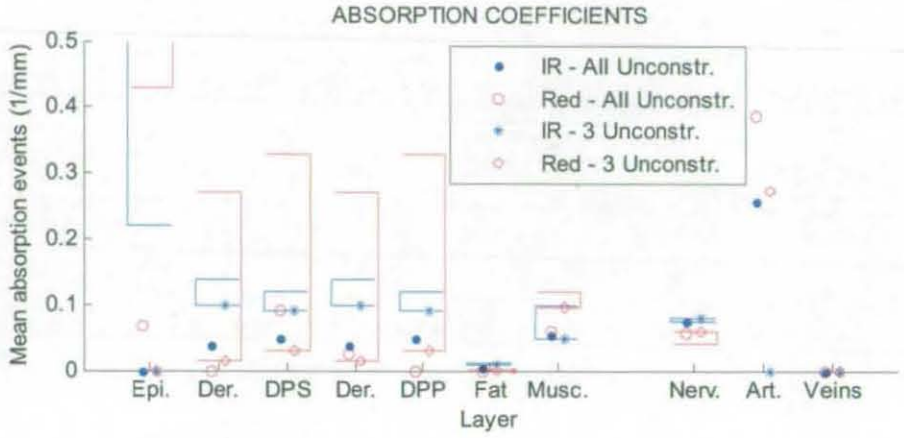

Figure 5.40 - Absorption coefficients and corresponding constraints for IR and red for iterative analysis with all coefficients unconstrained and arteries, veins and epidermis coefficients unconstrained.

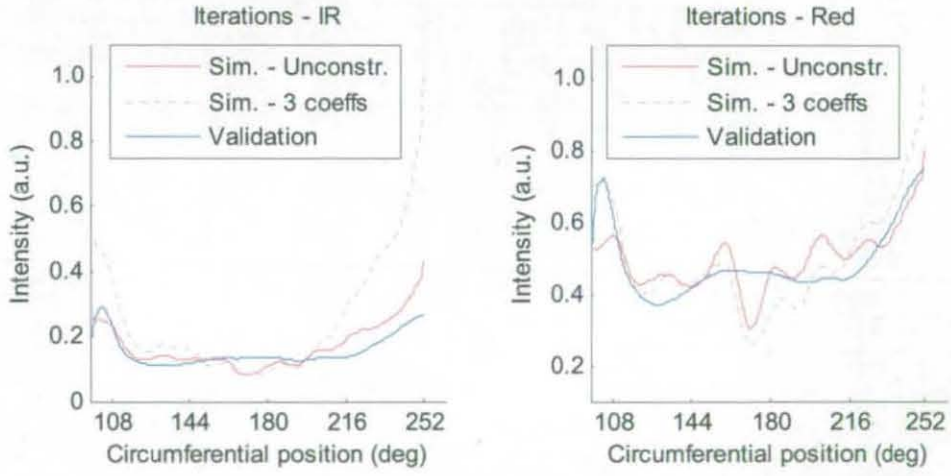

Figure 5.41 - Normalised sums of differences of empirical validation DCs and simulation DCs for IR (left) and red (right) illumination, showing the results of iterative analysis with constrained coefficients and uncontrained coefficients for arteries, veins and epidermis.

A certain agreement is evident between the coefficients resulting from constrained and unconstrained analysis shown in Figure 5.40. However, the unconstrained coefficients in the results from constrained analysis, namely, epidermis, and blood

vessel coefficients, demonstrate poorer convergence than the corresponding ones of the unconstrained analysis. This is a sign that, firstly, the constraints as defined from ranges of coefficients found in literature do not correspond to the real values that would correspond to the empirical data, and secondly, that the scattering coefficients which yielded the mean path lengths used to generate the simulated distributions similarly do not correspond. Both of these statements are in agreement with the fact that the wavelengths of coefficients used in the set of simulation data do not correspond to the wavelengths used in the light source for this set of empirical data.

5.3.2.2 Pulsatility Coefficients

The final iterative analysis is performed on the dynamic distributions yielded by the DC distributions from unconstrained processing, which are shown in Figure 5.41. The resultant coefficients and dynamic distributions are generated using unconstrained analysis and each of these can be seen in Figures 5.42 and 5.43. An imperfect characterisation in the static distributions expectedly yields divergence in the coefficients. Resultant ratio of ratios distributions shown in Figure 5.44 show unreasonably high values and variability, thus further demonstrating the lack of correlation.

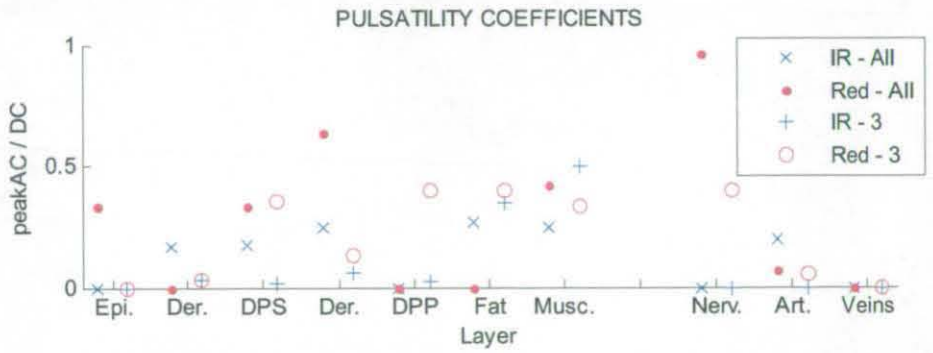

Figure 5.42 - AC coefficients for IR (left) and red (right) illumination after iterative analysis with all coefficients and 3 coefficients unconstrained.

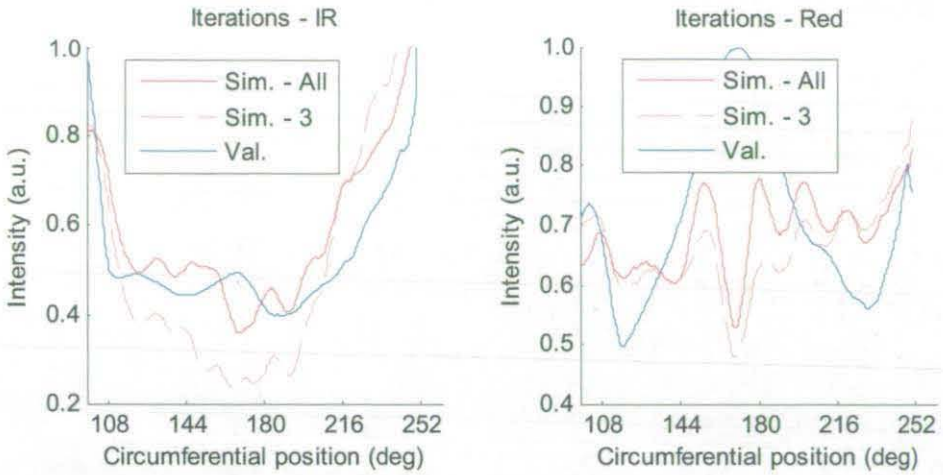

Figure 5.43 - AC distributions for IR (left) and red (right) illumination after iterative analysis with all coefficients and 3 coefficients unconstrained.

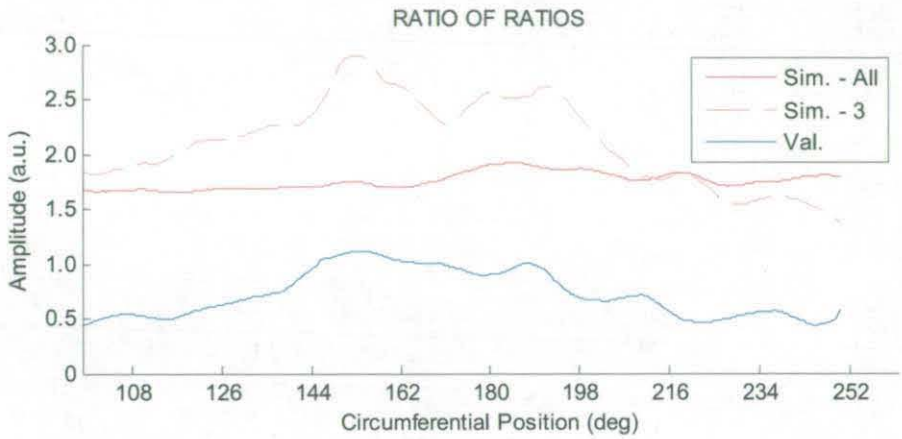

Figure 5.44 - Comparative plot of empirical and simulated ratio of ratios distributions.

This chapter has detailed the protocols used for simulation and validation experiments, specifically providing details with respect to the choice of tissue optical properties and assumptions for simulation and the choice of light sources and detection schemes for validation. The results to all the experiments of this investigation have been distilled and presented, with emphasis on comparative results for simulation and validation experiments.

6 DISCUSSION

This chapter contains an in-depth discussion of all experiments performed in this investigation. The areas which warrant further research and development, as suggested by the discussion, are also detailed. Specifically, improvements are suggested for the following areas:

- Modifications to the validation platform in order to improve the quality of empirical data produced
- The development of a proprietary MC simulation engine specific to this application, in order to allow a much higher efficiency in the simulation process
- The implementation of MRI scans to generate or validate models for simulation
- A series of potential future experiments pertaining to the platform of this investigation.

6.1 EMPIRICAL VALIDATION PLATFORM

Empirical experiments showed a series of limiting factors and intrinsic tradeoffs in the platform, along with possible countermeasures for these. The light source head and finger support structure proved to be a limiting factor throughout, essentially constraining measurements of empirical distributions to approximately 90° - 270° with respect to light-source position. The imaging solution brought a significant improvement in the characterisation of responses with respect to the ring sensor solution by providing a much higher number of distribution samples. Responses from all cameras demonstrated the high degree of DC characterisation by showing a high correlation between channels and manifesting drops in intensity corresponding to blood vessels.

Data captured in 8 bit yielded barely recognisable PPG signals as a consequence of lack of definition in terms of intensity levels. Light source intensities were set in such a way as to bring the highest DC values of transmitted light as close as possible to sensor saturation as a potential solution to this issue. In the case of the 8 bit camera, the tradeoffs for achieving this were the use of a higher number of LEDs per wavelength at the expense of broadening the light source beam profile. This option was discarded in subsequent experiments with the 10 bit and 12 bit cameras in order to maintain a more quantifiable light source definition and a closer similarity to the light source characteristics in simulation. PPG signals extracted from the 10 bit camera proved reliable throughout all positions, showing no quantisation effects and demonstrating no need for smoothing. An increase in camera bit-rate was reflected in the smoothness of extracted PPG signals and the ability to reduce the virtual detector window size.

Working in the near-saturation region of the camera sensors meant increasing frame exposure times at the expense of lower frame rates and subsequently poorer time characterisation of PPG signals, or conversely, recording data individually for each light source wavelength at the expense of loss of correlation between datasets with respect to wavelength. The use of low frame rates meant forfeiture of the option to approximate the dynamic responses through smoothing and the ability to perform reliable visual assessment of PPG signal qualities. The first recording session with the 12 bit camera, which was performed at 15 fps per wavelength, yielded PPG

signals without the characteristic dichrotic notch and was therefore difficult to assess. However, the resultant ratio of ratios distribution demonstrated a high accuracy at ±0.2, thus reflecting the time correlation of the opto-physiological responses. The 10 bit camera recording session was performed at 40 fps, which was made possible by performing individual recording passes for each wavelength. The PPG signals were consistently clean but these could not be guaranteed to be taken at times when physiological conditions were identical, and the resultant ratio of ratios distribution shows a notable variation of ±0.4, exacerbated by the presence of an offset between wavelength responses. An attempt was made towards ensuring closer physiological response correlation in the second 12 bit recording session by decreasing the duration of measurements to 3 seconds for each position and each wavelength.

The use of RCLEDs as the light source demonstrated an increased sensitivity to optical coupling between the source and the probed tissue in comparison to the use of standard LEDs. This resulted in the presence of significant signal corruption from motion artefact. Attempts at reducing this effect consisted of increasing light source housing pressure, which yielded a slight improvement in signal quality but resulted in increased obstruction from the housing in lateral positions. Despite signal corruption, ratio of ratios distributions under RCLED illumination proved to be stable within an acceptable range. The presence of distributions from several recording passes at different hand positions yielded a higher stability in comparison to that yielded by the clean signals recorded in the 10 bit session with standard LEDs.

In terms of subject repeatability, the statistical analysis of ratios indicates an even distribution of dynamic signal strength but suggests a tendency for stronger signals in the vicinity of ± 40° locations at either side of the 180° mark. Analysis of ratio of ratios (R) distributions in Figure 5.26 shows a relatively flat response centred around R=1.6 for all subjects. A significant decay of R values is evident at the lateral positions of distributions (90° - 108° and 252° - 270°), reflecting the increased sensitivity to light source coupling artefact at positions closest to the light source housing. An average inter-quartile variation of ±0.25 in R values suggests the presence of an arterio-venous coupling effect demonstrated in previous oximetry work carried out in the research group, which would be aggravated by venous pooling due to hand height and relatively high pressure introduced by the finger support structure.

A significant increase can be expected in the specificity of acquired distributions from improvements in the hardware setup. These include a more ergonomically designed finger support structure for minimisation of probe coupling motion artefact and homogeneisation of pressures on subject fingers, and a stricter experimental protocol in terms of subject cardiovascular stabilisation. Nevertheless, the results suggest that an adequate design for a novel probe would include several sensors at arbitrary positions within the circumferential range 180° ±60° to allow for the selection of the cleanest signals through the use of cross-correlative analysis. Such an arrangement would also allow a preferential selection of signals from positions with the highest signal-to-noise ratio. Additionally, motion artefact cancellation in two axes of motion can potentially be implemented with detectors at orthogonal positions.

6.1.1 Future Work

Out of the two hardware solutions investigated for empirical validation, the imaging solution provided the greatest spatial characterisation and flexibility. A ring sensor with a higher spatial characterisation than that of the one used in this investigation would potentially provide analogue signals with minimal distortion due to motion artefact. Nevertheless, the trade-off between signal quality and spatial characterisation means that an imaging solution with proper minimisation of motion artefact is likely to provide a greater amount of intensity distribution information at comparable overall signal quality.

The imaging platform would benefit from the following improvements: Firstly, the current rotating platform relied on manual operation. By motorising the rotation of the camera, the recording process would benefit from an increased capturing speed. Secondly, the light source is statically mounted on the platform. Further experimentation would benefit from a controlled means of light source placement within a specific range of positions. Also, the implementation of pressure cuffs as a means of constraining the motion of and controlling the pressure on the probed finger would yield a far greater control of experimental conditions. Finally, motion artefact due to variations in the optical coupling between the light source and the probing tissue proved to be a significant issue. The light source mounting therefore requires an improved design to minimise this effect.

6.2 MONTE CARLO SIMULATION PLATFORM

The limitations posed by the use of OptiCAD make it essential to develop an open-source MC engine in a flexible and efficient programming language such as C++. A proprietary engine specific to the application presented in this research project would inherently remove the bottlenecks and unnecessary steps found in the current implementation. An open-source solution would allow the possibility of distributed computing, the ongoing optimisation of the platform, and the development of new features. This section contains a discussion of the implementation of a MC engine, of potential new features for the platform, and of work that has been done towards both of these areas during the course of this research project.

6.2.1 Voxel-Based Model Handling

Implementations of MC simulation for optical propagation in human tissue of arbitrary geometries generally use what can be referred to as a voxel-based approach to ray tracing, where a voxel is the smallest element of a digital representation of a solid, much like a pixel is for a digital image. A voxel-based approach can be found in other research projects utilising MC simulation in arbitrary geometries[65].

A series of function libraries have been developed towards the implementation of such an engine. The first of these provides a voxel-based approach to the storage of arbitrary geometries to an arbitrary level of precision. Essentially, a model is split into data structures representing a $1mm^3$ space. Each of these is empty if they correspond to empty space, labelled with a reference to a global structure containing relevant information of the layer that they represent, if they represent a complete portion of the tissue. If a data structure represents any combination of empty space and any of the tissue types in the model, it is subdivided into substructures until each individual substructure represents a homogeneous part of the model, or until the specified level of precision is reached, as illustrated in Figure 6.1. This methodology for the handling of geometrical models of solids provides intrinsic compression, the ability to store models of any size and any relevant data provided that enough data storage is available, and it provides an infrastructure for the parallel execution of ray traces.

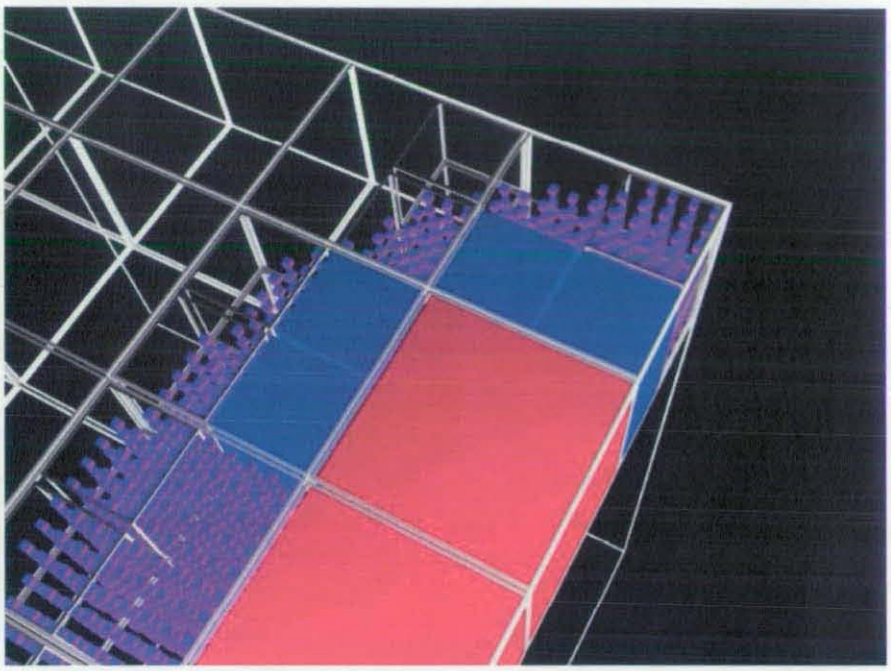

Figure 6.1 – Illustration of cell-based approach to geometric model storage and handling.

A second function library that was developed converts a faceted model such as the one used in this project into a voxel model of arbitrary geometry and stores it using the previous library. As such, it provides an interface between the two geometric modelling modalities. Faceted models provide certain advantages over solid voxel models since software platforms such as 3D Studio MAX, and open-source algorithms that allow creation and extensive manipulation of 3D faceted models are widely available. The function works by determining the intersection of every edge of every facet in the model with a plane perpendicular to longitudinal axis of the finger at every interval specified according to the desired level of accuracy. Perimeters are defined at each plane for each of the layers of the model, and these perimeters are filled. This process results in 2D slices of the model that resemble the DICOM images output in medical imaging techniques such as MRI scanners, as shown in Figure 6.2. At this stage, a workable voxel model has been generated.

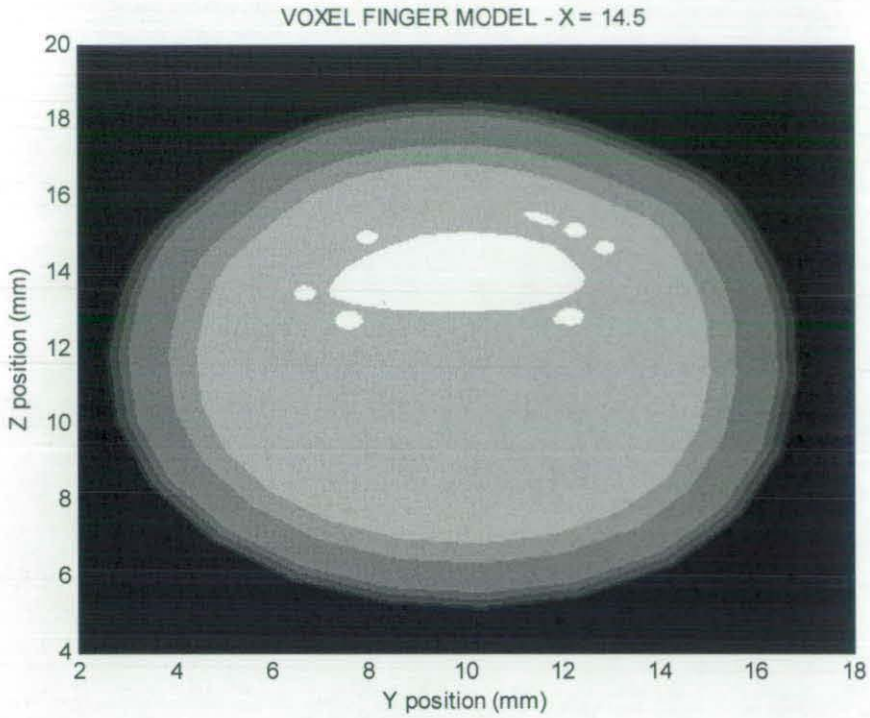

Figure 6.2 – Cross-section of voxel-based version converted from faceted finger model used in this project.

6.2.2 MRI Scan Model Implementation

MC simulation in this project was performed on a generic model of an adult finger; therefore, the degree of correspondence between this model and the real finger of the subject that was submitted to empirical measurements is largely unknown. This research would consequently greatly benefit from an accurate measure of the internal makeup of the tissue bed in question. A preliminary experiment was performed using an MRI scanner to produce cross-sectional images of an adult male finger, an image of which can be seen in Figure 6.3.

Figure 6.3 – DICOM image from MRI scan of adult male hand performed in Glenfield Hospital, University Hospital of Leicester, UK.

The resultant data shows that the MRI does not provide sufficient information to distinguish, for instance, specific skin layers. Nevertheless, information gathered from MRI scans of low resolution can still be used to determine the major dimensions and positions of internal structures such as blood vessels. The use of such scans requires the use of algorithms for delimitation of tissue types and subsequent generation of voxel-based models, which in turn suggests studies on the relationship between normalised MRI scan intensities and macroscopic optical properties. One such method has been developed for segmentation and reconstruction of cortical surfaces from medical scans[66].

6.2.3 Experiments and Settings

Simulations were performed using the diffusion approximation for all layers of the model. However, it is well known that the diffusion approximation is not valid at source-detector separations less than approximately one reduced mean free path ($1/(\mu_s+\mu_a)$) and in tissues with low albedo ($\mu_s'/(\mu_s'+\mu_a)$)[67,68]. A more accurate approach requires the use of a hybrid method that employs anisotropic scattering for selected layers in simulation. Additionally, a more accurate methodology should include modelling of melanin concentration in the dermis.

The rate of data production in the current MC simulation platform poses a significant limitation. Any experiment that could elucidate potential ways to increase the efficiency of ray tracing is therefore justified. One such experiment would be to perform a series of comparative simulations to determine the relationship between ray traces resulting from three-dimensional arbitrary geometry and a corresponding two-dimensional simulation of a specific cross-section of the full geometry. If little geometrical variation is expected with respect to a change in cross-section, as is the case with a finger, it may be possible to simplify the simulation to two dimensions while still maintaining the precise nature of results resulting from an arbitrary geometry. Another feature that should be considered is the geometric manipulation of certain components of the model—specifically the veins—according to expected physiological reponses prior to MC modelling.

Due to the limitations of the simulation platform, data were generated for a single set of scattering coefficients at a single light source position. In order to increase the validity of the virtual environment, a series of ray traces should be performed for a range of light source positions. Additionally, the virtual definition of the light source was limited to a near-point source with lambertian distribution. Characterisation of responses with respect to light source beam parameters would be advantageous as an expansion of the capabilities of the platform. A relatively simple approach to this consists of performing larger ray traces for a light source with the widest possible viewing angle (180°) and subsequent scaling of ray intensities according to the desired beam profile.

It is clear that the accuracy of coefficients plays an important part in the applicability of this platform. One of the difficulties encountered in studies of tissue optical properties arises when trying to determine these *in-vivo*. In the context of this project, there is a need for full relational reviews of optical properties in which coefficients are given certain ranges with respect to relevant physiological parameters such as perfusion. As the availability and accuracy of these coefficients increases, so will the convergence of the results from this platform. As experimental settings of this sort are improved, it is possible that inverse Monte Carlo techniques of arbitrary geometries could be used to determine increasingly accurate in-vivo optical properties of biological tissues.

6.3 ITERATIVE ANALYSIS

The simulated data used in iterative analysis consisted of sets of traced rays using 633nm and 850nm reduced scattering coefficients. Static and dynamic distributions generated from the 10 bit and 12 bit validation experiments were used as the reference empirical sets for the analysis. The process demonstrated that a threshold number of passes on the iteration of coefficients was necessary for a proper convergence. The threshold was determined to be 20 passes. Results show that constraining coefficients serves to elucidate those that have the greatest effect in the correlation of distributions. Constrained analysis also provides a measure of correlation when individually unconstrained coefficients converge to values to the corresponding ones in unconstrained analysis. However, a true measure of correlation depends on both a high distribution correlation and on the convergence of coefficients within their corresponding ranges when unconstrained.

Empirical data sets from validation experiments utilising the 10 bit camera yielded high correlations and adequate convergence in the DC distributions and coefficients. Analysis of 12 bit empirical data is performed under the erroneous assumption that the macroscopic optical coefficients of all tissue types at 633nm and 850nm are essentially identical to those at 650nm and 870nm respectively. The invalidity of this assumption is supported by the corresponding results. However, these results reinforce the convergence that is evident in the iterative analysis of the 10 bit empirical data, which was generated under light source wavelengths corresponding to those of simulation. IR distributions demonstrated a consistently poorer correlation than red distributions for both validation sets, an effect which is in line with the fact that IR scattering coefficients were approximated due to their lack of availability in relevant tissue optics literature.

Due to the lack of precise knowledge of dynamic optical properties with respect to tissue type, constraining the iterative analysis on AC distributions is not easily done, currently relying on a series of educated guesses. We can expect to encounter the following dynamic phenomena:

- Pulsatilities below 0.2-0.4
- A higher pulsatility in arteries than in veins.

- A higher pulsatility in dermal plexus (DPS, DPP) layers of the skin than in other skin layers
- A similar pulsatility in the separate dermis layers.
- Lower pulsatility in the epidermis layer with respect to dermis layers

It is possible, although unlikely that macroscopic pulsatility coefficients are zero for any given tissue type, due to the fact that all tissues are perfused with blood and are therefore submitted to the arterial blood pulse wave.

Iterative analysis results suggest a tendency towards improved convergence for increases in the accuracy of empirical measurements and simulation settings, followed by an increased ability to establish and enhance heuristics of dynamic phenomena.

6.4 CONTRIBUTIONS TO KNOWLEDGE

This research project has yielded an engineering model for the opto-physiology of PPG and pulse oximetry. The model is an interpolation between the simplistic Beer-Lambert description of PPG and the mathematically rigorous RTT, and it provides increased characterisation in terms of parameters such as light source, sensor position and multilayer optical properties while maintaining a relatively high level of applicability. Additionally, it illustrates a successive approximation approach to the design of such models.

Several novel physiological measurement modalities for photoplethysmography and pulse oximetry have been developed and investigated. These have shown the capacity to map optical responses in a human finger in two dimensions to a high accuracy and great potential for improvement of characterisation with respect to increases in equipment sensitivity and improvements in hardware design.

Finally, the research methods employed in the investigation of the hardware and software components of the platform and of how these can yield quantitative models is a novel approach with great potential for application in the development of bio-monitoring devices with improved sensitivity and reliability. The approach is likely to grow in use in sync with increases in available tissue optics knowledge.

7 CONCLUSIONS

Experimental results show that the opto-physiological modelling platform is capable of providing data that are not available empirically. The validity of such data is a function of the quality of convergence achieved when correlating empirical measurements with the corresponding data from the simulation environment. The quality of convergence depends on both the quality of empirical data and the accuracy of tissue optical properties used in simulation. Finally, the quality of empirical data is defined by both the quality of acquired signals and the degree to which the full range of physiological responses is captured in these.

7.1 MONTE CARLO SIMULATION

OptiCAD was used as a prototype for a MC engine in order to perform a feasibility study in the least possible amount of time. Unfortunately, its limitations have proven to be a hindrance even at these early stages of platform development. Firstly, the software is closed source and is protected by a hardware key, which poses several problems. Processing power applied to MC simulation is limited to that of a single workstation and its rate of data output is severely limited as a consequence. Also, the data output of OptiCAD is an ASCII text file, which poses a bottleneck when importing the data into MATLAB. Finally, the output data does not include information pertaining to the medium in which ray segments are contained. A significant amount of reverse engineering was necessary to overcome this issue.

Due to the limitations of the simulation platform, only a single set of MC ray traces was considered, representing the propagation of light under illumination from a light source with two wavelengths, placed at the standard position of transmittance pulse oximetry probes. Consequently, the capacity for analysis of the platform is limited. The lack of specific tissue optical properties in the literature meant a lower reliability in resultant simulations.

7.2 EMPIRICAL MEASUREMENTS

As a contact modality employing analogue electronics, and given that the noise in the electronic circuitry was minimised, the photodiode solution to characterisation of intensity distributions demonstrated a notable capability to characterise transmitted intensities. Its weakness was in the spatial characterisation of distributions, due to the inherent difficulty of adapting an array of point photodiodes to optically couple with the probing tissue, whilst containing elements large enough to counteract motion artefact. The latter is not addressed in the scope of this research project.

Conversely, the employment of an imaging device, which is a non-contact digital solution, demonstrates a weakness in terms of intensity characterisation due to the quantisation that results from its internal digitisation and due to motion artefact from variations in optical coupling from the light source. Direct coupling and geometric constraints proved to be a limiting factor in both contact and non-contact validation solutions, essentially reducing the validity of empirical distributions to approximately 90° - 270° with respect to light-source position. Nevertheless, the imaging solution has the capacity to provide reliable two-dimensional responses

Validation experiments as reported show a lack of coherence as a result of the wide variety of hardware arrangements tested. Constriction inflicted by the support structure used to stabilise the subject's finger is present, although it is hard to quantify. Furthermore, all the validation experiments documented in this thesis gave way to important issues and subsequent improvements with respect to the experimental protocol. The results show that a significantly higher quality can be achieved in the empirical characterisation of optical responses around the circumference of a finger.

Comparison of empirical measurements using standard LEDs and resonant cavity LEDs suggests that the latter have an increased sensitivity to motion artefact. However, empirical measurements from RCLEDs demonstrate a high stability with respect to static intensity responses and ratio of ratios distributions. Their narrow spectral bandwidth is additional justification for their use in future research.

7.3 ITERATIVE ANALYSIS

Iterative curve fitting results demonstrated a meaningful correlation with expected values. Distributions corresponding to red illumination demonstrated a consistently higher stability in coefficient convergence and curve fitting quality than IR distributions, an effect which is in line with the fact that IR scattering coefficients were approximated due to their lack of availability in relevant tissue optics literature. Also, static intensity distributions scored higher in correlations, thus reflecting the loss of quality inherent in the process of dynamic signal extraction, coupled with regular equipment and experimental errors. Coefficients for blood vessels consistently converged poorer than others, an effect which is in line with the fact that the diffusion approximation does not hold for tissues with low albedo.

It is concluded that using the complete platform of this project, the validity of the absorption, and subsequently, the pulsatility coefficients to which the curve fitting algorithms converge, will increase in proportion to increases in the accuracy of empirical measurements and scattering coefficients. The degree to which these coefficients are valid is reflected by the stability of the coefficient convergence during iterative analysis. Finally, the results indicate that this approach to opto-physiological modelling warrants further research.

REFERENCES

[1] Kamal AA, Harness JB, Irving G, Mearns AJ, "Skin photoplethysmography--a review", *Comput. Methods Programs Biomed.*, 28:4, 257-269,1989.

[2] Hertzman AB, "Photoelectric plethysmography of the fingers and toes in man", *Prec. Soc. Exp. Biol. Med.*, 37, 529-534, 1937.

[3] Dombe F, "Spectrophotometric device for the in-vivo determination of oxyhaemoglobin", France Patent No:815244, 1936.

[4] Samuels J, "Spectroscopic apparatus, particularly for medical use", United Kingdom Patent No:515310, 1939.

[5] Millikan GA, "Oxygen Meter", United States Patent No:2358992, 1944.

[6] Smaller B, "Multi-unit, single scale oximeter", United States Patent No:2423855, 1947.

[7] Aoyagi T, "Pulse oximetry: its invention, theory, and future", *J. Anesth.*, 17, 259–266, 2003.

[8] Runciman WB, Webb RK, Barker L, Currie M, "The Australian Incident Monitoring Study. The pulse oximeter: applications and limitations--an analysis of 2000 incident reports", *Anaesth. Intensive Care*, 21:5, 543-550, 1993.

[9] Sigurdsson GH, McAteer E, "Morbidity and mortality associated with anaesthesia," *Acta Anaesthesiol. Scand.*, 40:8 Pt 2, 1057-1063, 1996.

[10] Kamat V, "Pulse Oximetry", *Indian J. Anaesth.*, 46:4, 261-268, 2002.

[11] The Oregon Vein Center – Venous anatomy and physiology, http://www.oregonveincenter.com/level.itml/icOid/21, [accessed 02/07/2006]

[12] Irvine WM, Pollack JB, "Infrared optical properties of water and ice spheres", *Icarus*, 8, 324-360, 1968.

[13] Melanosome absorption coefficient – Oregon Medical Laser Center website, http://omlc.ogi.edu/spectra/melanin/mua.html, [accessed 21/05/2007]

[14] Moyle J.T.B., *Principles and Practice Series: Pulse Oximetry*, London: BMJ Books, 1998.

[15] Chan FCD, "Non-invasive Venous Oximetry through Venous Blood Volume Modulation", Doctoral Thesis, Loughborough University, Loughborugh, UK, 2002.

[16] Mannheimer P, Casciani J, Fein M, Nierlich S, "Wavelength selection for low saturation pulse oximetry", *IEEE Trans. Biomed. Eng.*, 44:3, 148-158, 1997.

[17] Wray S, Cope M, Delpy DT, Wyatt JS, Reynolds EOR, "Characterization of the near infrared absorption spectra of cytochrome aa3 and haemoglobin for the non-invasive monitoring of cerebral oxygenation", *Biochimica et Biophsica Acta*, 933, 184-192, 1988.

[18] Wood EH, "Apparatus for determining percentage oxygen-saturation in blood", United States Patent No:2706927, 1955.

[19] Mendelson Y, "Pulse oximetry: theory and applications for noninvasive monitoring", *Clin. Chem.*, 38, 1602–1607, 1992.

[20] Jubran, A, "Pulse oximetry," *Intensive Care Med.*, 30, 2017-2020, 2004.

[21] Mendelson, Y and Ochs, BD, "Noninvasive Pulse Oximetry Utilizing Skin Reflectance Photoplethysmography", *IEEE Trans. Biomed. Eng.*, 35:10, 798-805, 1988.

[22] Zonios G, Shankar U, Iyer VK., "Pulse oximetry theory and calibration for low saturations", *IEEE Trans. Biomed. Eng.*, 51:5, 818-822, 2004.

[23] Sahni R, Gupta A, Ohira-Kist K, Rosen TS, "Motion resistant pulse oximetry in neonates", *Arch. Dis. Child Fetal Nenatal Ed.*, 88, F505-F508, 2003.

[24] Hayes M, Smith P, "A new method for pulse oximetry possessing inherent insensitivity to artifact", *IEEE Trans. Biomed. Eng.*, 48:4, 452-460, 2001.

[25] Hayes M, Smith P, "Artifact reduction in photoplethysmography", *Appl. Opt.*, 37:31, 7437-7446, 1998.

[26] Rheineck-Leyssius AT, Kalkman CJ, "Influence of Pulse Oximeter Settings on the Frequency of Alarms and Detection of Hypoxemia", *J. Clin. Monit.*, 14, 151-156, 1998.

[27] Hayes M, "Artefact Reduction in Photoplethysmography", Doctoral Thesis, Loughborough University, Loughborough, UK, 1998.

[28] Poets CF, Stebbens VA, "Detection of movement artifact in recorded pulse oximeter saturation", *Eur .J. Pediatr.*, 156, 808-811, 1997.

[29] Barker SJ, "The Effect of Motion on the Accuracy of Six Motion-Resistant Pulse Oximeters." *Anesthesiology*, 95, A587, 2001.

[30] Huch A, Huch R, Konig V, Neuman MR, Parker D, Yount J, Lubbers D, "Limitations of Pulse Oximetry", *The Lancet*, 1, 357-358, 1988.

[31] Beek JF, Blokland P, Posthumus P, Aalders M, Pickering JW, Sterenborg HJCM, van Gemert MJC, "*In vitro* double-integrating-sphere optical properties of tissues between 630 and 1064 nm." *Phys. Med. Biol.*, 42, 2255-2261, 1997.

[32] Flock ST, Jacques SL, Wilson BC, Star WM, van Gemert MJ, "Optical properties of Intralipid: a phantom medium for light propagation studies", *Lasers Surg. Med.*, 12:5, 510-519, 1992.

[33] Edrich T, Flaig M, Knitza R, Rall G, "Pulse oximetry: An improved *in-vitro* model that reduces blood flow-related artifacts", *IEEE Trans. Biomed. Eng.*, 47:3, 338-343, 2000.

[34] Mendelson Y, McGinn MJ. "Skin reflectance pulse oximetry: in vivo measurements from the forearm and calf.", *J. Clin. Monit.* 7:7-t2, 1991.

[35] Sherebrin MH, Sherebrin RZ, "Frequency analysis of the peripheral pulse wave detected in the finger with a photoplethysmogram", *IEEE Trans. Biomed. Eng.*, 37:3, 313-317, 1990.

[36] Bhattacharya J, Kanjilal PP, Muralidhar V, "Analysis and characterization of photo-plethysmographic signal", *IEEE Trans. Biomed. Eng.*, 48:1, 5-11, 2001.

[37] Hong Enriquez R, Sautie Castellanos M, Falcon Rodriuez J, Hernandez Caceres JL, "Analysis of the photoplethysmographic signal by means of the decomposition in principal components", *Physiol. Meas.*, 23, N17-N29, 2002.

[38] Addison PS, Watson JN, "A novel time–frequency-based 3D Lissajous figure method and its application to the determination of oxygen saturation from the photoplethysmogram", *Meas. Sci. Technol.*, 15, L15-L18, 2004.

[39] Coetzee FM, Elghazzawi Z, "Noise-resistant pulse oximetry using a synthetic reference signal", *IEEE Trans. Biomed. Eng.*, 47:8, 1018-1026, 2000.

[40] Kyriacou PA, Moye AR, Choi DM, Langford RM, Jones DP, "Investigation of the human oesophagus as a new monitoring site for blood oxygen saturation", *Physiol. Meas.*, 22:1, 223-232, 2001.

[41] Wood LB, Asada HH, "Noise cancellation model validation for reduced motion artifact wearable PPG sensors using MEMS accelerometers," *Proc. Of*

the Annual International Conference of the IEEE Engineering in Medicine and Biology Society. IEEE Engineering in Medicine and Biology Society, 1, 3525-3528.

[42] Franceschini MA, Gratton E, Fantini S, "Noninvasive optical method of measuring tissue and arterial saturation: an application to absolute pulse oximetry of the brain." *Optics Letters*, 24:12, 829-831, 1999.

[43] Pinto Lima A, Beelen P, Bakker J, "Use of a perhipheral perfusion index derived from the pulse oximetry signal as a noninvasive indicator of perfusion", *Crit. Care Med.*, 30:6, 1210-1213, 2002.

[44] Prahl SA, Keijzer M, Jacques SL, Welch AJ, "A Monte Carlo model of light propagation in tissue", *SPIE Proceedings of Dosimetry of Laser Radiation in Medicine and Biology*, IS 5, 102-111, 1989.

[45] Marble DR, Burns DH, Cheung PW, "Diffusion-based model of pulse oximetry: *in vitro* and *in vivo* comparisons," *Appl. Opt.* 33, 1279-1285, 1994.

[46] Koyama T, Iwasaki A, Ogoshi Y, Okada E, "Practical and adequate approach to modeling light propagation in an adult head with low scattering regions by use of diffusion theory", *Appl. Opt.*, 44:11, 2094-2103, 2005.

[47] Heiskala J, Nissila I, Neuvonen T, "Modeling anisotropic light propagation in a realistic model of the human head", *Appl. Opt.*, 44:11, 2049-2057, 2005.

[48] D. Y. Churmakov, I. V. Meglinski, D. A. Greenhalgh, "Influence of refractive index matching on the photon diffuse reflectance", *Phys. Med. Biol.* 47, 4271-4285, 2002.

[49] Tuchin VV, *Tissue Optics: Light Scattering Methods and Instruments for Medical Diagnosis*, SPIE Tutorial Texts in Optical Engineering, Bellingham: SPIE Press, TT38, 2000.

[50] Tuchin V, Utz S, Yaroslavsky I, "Tissue optics, light distribution, and spectroscopy", *Opt. Eng.*, 33, 3178-3187, 1994.

[51] Roggan A., Friebel M., Dorschel K., Hahn A. Muller G., "Optical properties of circulating human blood in the wavelength range 400-2500 nm", *J. Biomed. Opt.* 4, 1 , 36-46, 1999.

[52] Lopez M, Hofer H, et. al., "Spectral reflectance and responsivity of Ge- and InGaAs-photodiodes in the near-infrared: measurement and model." *Appl. Opt.*, 46:29, 7337-7344, 2007.

[53] Svaasand LO, Gomer CJ. "Optics in tissue." In: Muller GJ, Sliney DH (eds) *Dosimetry of laser radiation in medicine and biology*, Vol. IS-5. Bellingham: SPIE Optical Engineering, 114-132, 1990.

[54] J. F. de Boer, T. E. Milner, M. J. C. van Gemert, and J. S. Nelson, "Two-dimensional birefringence imaging in biological tissue by polarization-sensitive optical coherence tomography" *Opt. Lett.*, 22, 934-936, 1997.

[55] Ishimaru A. *Wave propagation and scattering in random media*. New York: Academic Press, 1978.

[56] Patterson MS, Wilson BC, Wyman DR, "The Propagation of Optical Radiation in Tissue I. Models of Radiation Transport and their Application", *Lasers in Medical Science*, 6, 155-168, 1991.

[57] Chandrasekhar S, *Radiative Transfer*, New York: Dover, 1960.

[58] Chen B, Stamnes K, Stamnes JJ, "Validity of the diffusion approximation in bio-optical imaging.", *Appl. Opt.*, 40:34, 6356-6366, 2001.

[59] Delpy DT, Cope M, van der Zee P, Arridge S, Wray S, Wyatt J, "Estimation of optical pathlength through tissue from direct time of flight measurement", *Phys. Med. Biol.* 33, 12,1433-1442, 1988.

[60] Hiraoka M, Firbank M, Essenpreis M, Cope M, Arridge SR, van der Zee P, Delpy DT, "A Monte Carlo investigation of optical pathlength in inhomogeneous tissue and its application to near-infrared spectroscopy", *Phys. Med. Biol.* 38, 1859-1876, 1993.

[61] Tuchin VV, Utz S, Yaroslavsky I, "Tissue optics, light distribution and spectroscopy", *Opt. Eng.*, 33:10, 3178-3187, 1994.

[62] Sobol I, "The distribution of points in a cube and the accurate evaluation of integrals (in Russian)", *Zh. Vychisl. Mat. i Mat. Phys.* 7, 784–802, 1967.

[63] Bashkatov A, Genina E, Kochubey V, Tuchin V, "Optical properties of human skin subcutaneous and mucous tissues in the wavelength range from 400 to 2000 nm", *J. Phys. D: Appl. Phys.* 38, 2543-2555, 2005.

[64] Ugnell A, Oberg P, "The optical properties of the cochlear bone", *Med. Eng. Phys.* 19, 630-636, 1997.

[65] Dale AM, Fischl B, Sereno MI, "Cortical Surface-Based Analysis I. Segmentation and Surface Reconstruction", *NeuroImage*, 9:2, 179-194, 1999.

[66] Boas DA, Culver JP, Stott JJ, Dunn AK, "Three dimensional Monte Carlo code for photon migration through complex heterogeneous media including the adult human head", *Optics Express*, 10:3, 159-169, 2001.

[67] F. Bevilacqua and C. Depeursinge, "Monte Carlo study of diffuse reflectance at source-detector separations close to one transport mean free path," *J. Opt. Soc. Am.*, A16:12, 2935-2945, 1999.

[68] S. T. Flock, M. S. Patterson, B. C. Wilson, and D. R. Wyman, "Monte Carlo Modeling of Light Propagation in Highly Scattering Tissues - I: Model Predictions and Comparison with Diffusion Theory," *IEEE Trans. Biomed. Eng.* 36:12, 1162-1168, 1989.

APPENDICES

The following appendices have been included:

I. LabVIEW front panel and block diagram for the virtual instrument developed for the control of the Inspecta-5 frame grabber (Mikrotron, Germany) and communications with a range of cameras via the CameraLink serial interface.

II. LabVIEW front panel and block diagram for the virtual instrument developed for the control of the DISCO4 PPG board (Dialog Devices, UK) and USB data acquisition device NI-DAQ M-6015 (National Instruments, USA).

III. Graphical user interface for OptiCAD software (OptiCAD Corporation, USA).

IV. Diagram of fixed and variable inputs for Monte Carlo simulation and post-processing functions.

I. LABVIEW APPLICATION FOR FRAME GRABBER

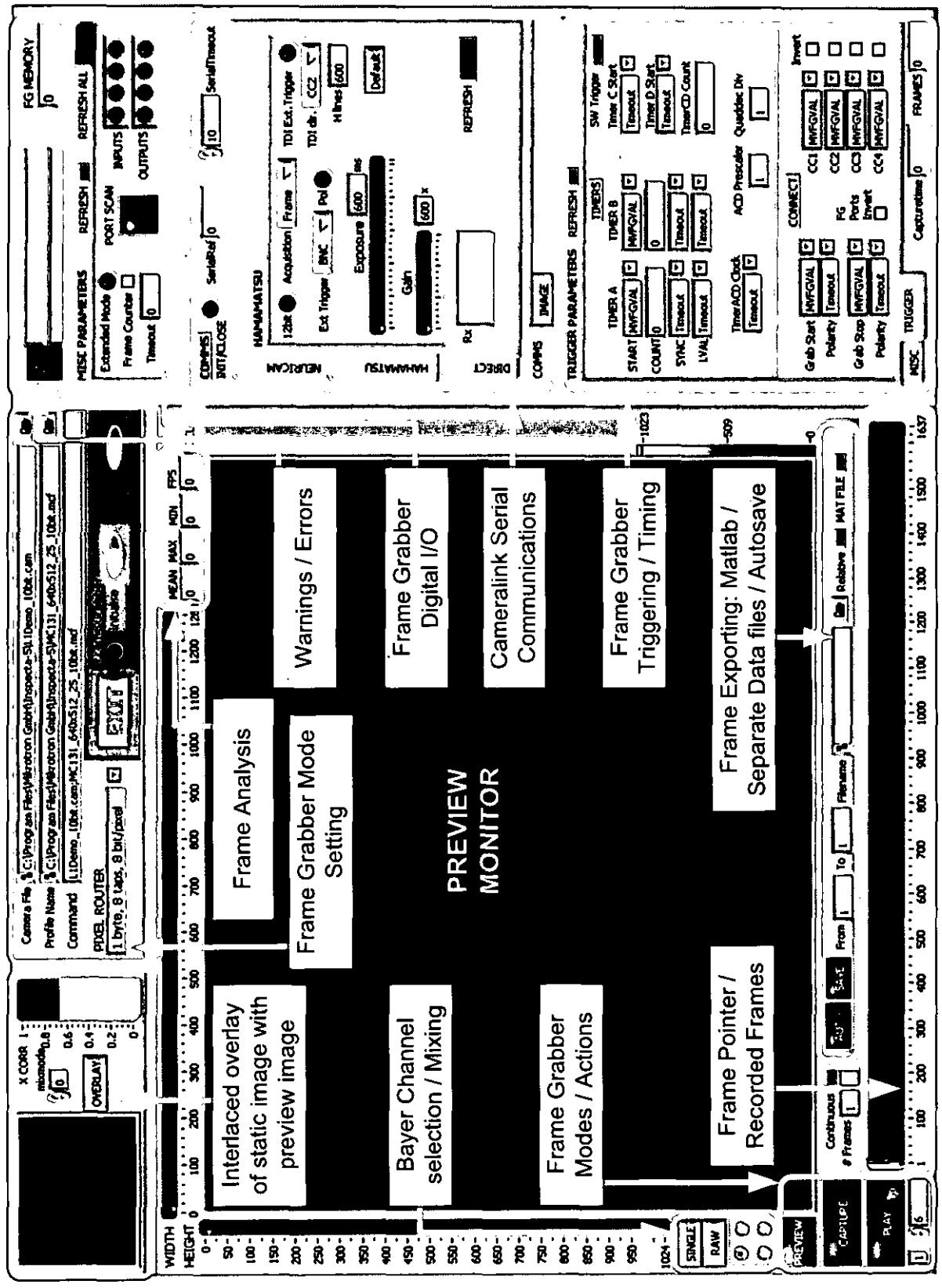

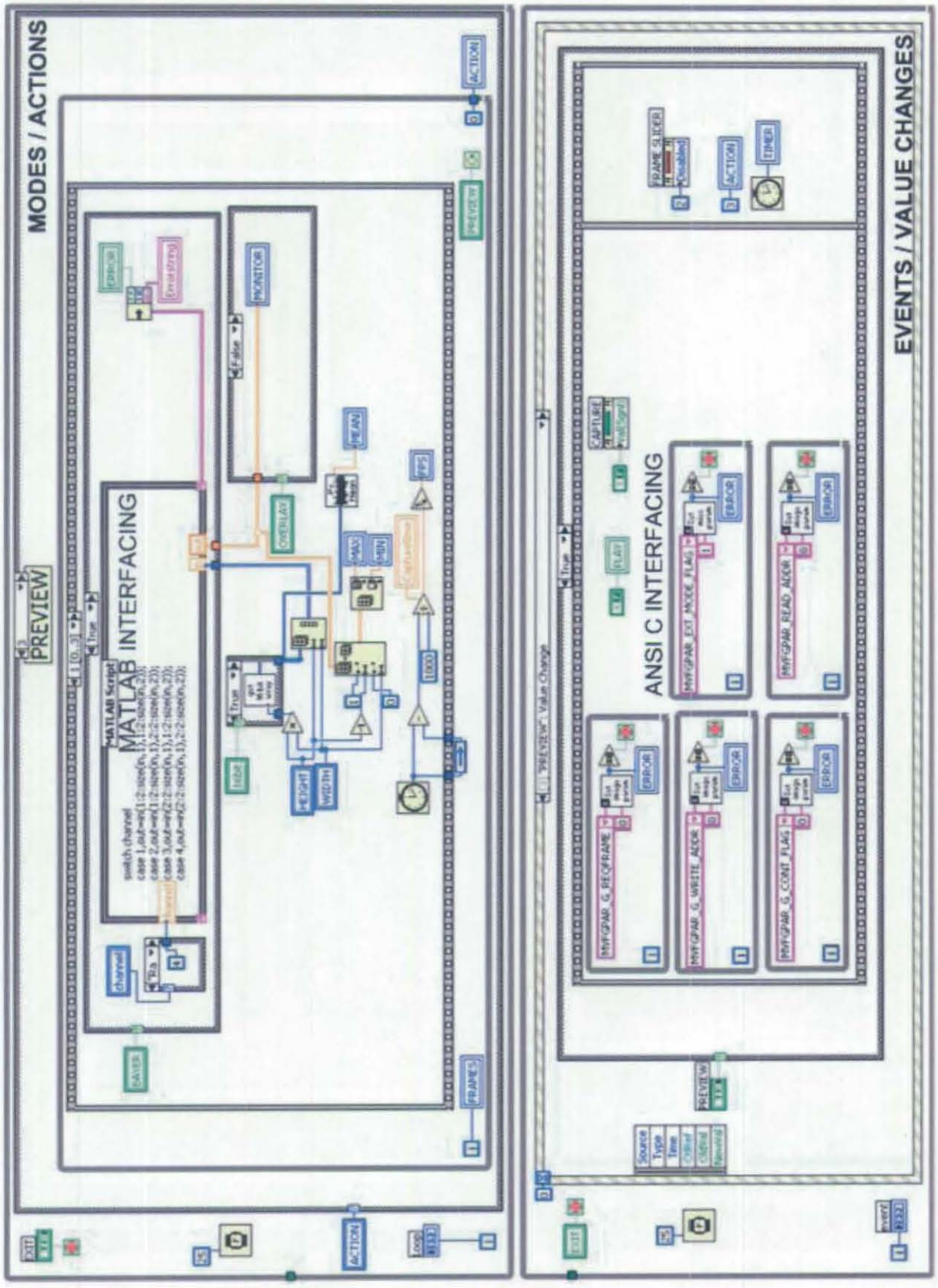
MODES / ACTIONS
PREVIEW
MATLAB Script
MATLAB INTERFACING
switch channel
case 1,out=in(1:2:size(in,1),1:2:size(in,2));
case 2,out=in(1:2:size(in,1),2:2:size(in,2));
case 3,out=in(2:2:size(in,1),1:2:size(in,2));
case 4,out=in(2:2:size(in,1),2:2:size(in,2));
Channel
Ts
ERROR
ErrorStatus
MONITOR
False
True
OVERLAY
MEAN
MAX
MIN
FPS
1000
HEIGHT
WIDTH
IMAGE
FRAME
ACTION
EXIT
STOP
EVENTS / VALUE CHANGES
"PREVIEW": Value Change
ANSI C INTERFACING
CAPTURE
PLAY
MWFGRAB_EXT_MODE_FLAG
MWFGRAB_READ_ADDR
MWFGRAB_G_REQFRAME
MWFGRAB_G_WRITE_ADDR
MWFGRAB_G_CONT_FLAG
ERROR
FRAME SLIDER
Enabled
ACTION
TIMER
PREVIEW
Source
Type
Time
Offset
Channel
Newval
EXIT
Error

II. LABVIEW APPLICATION FOR DISCO4 PPG BOARD

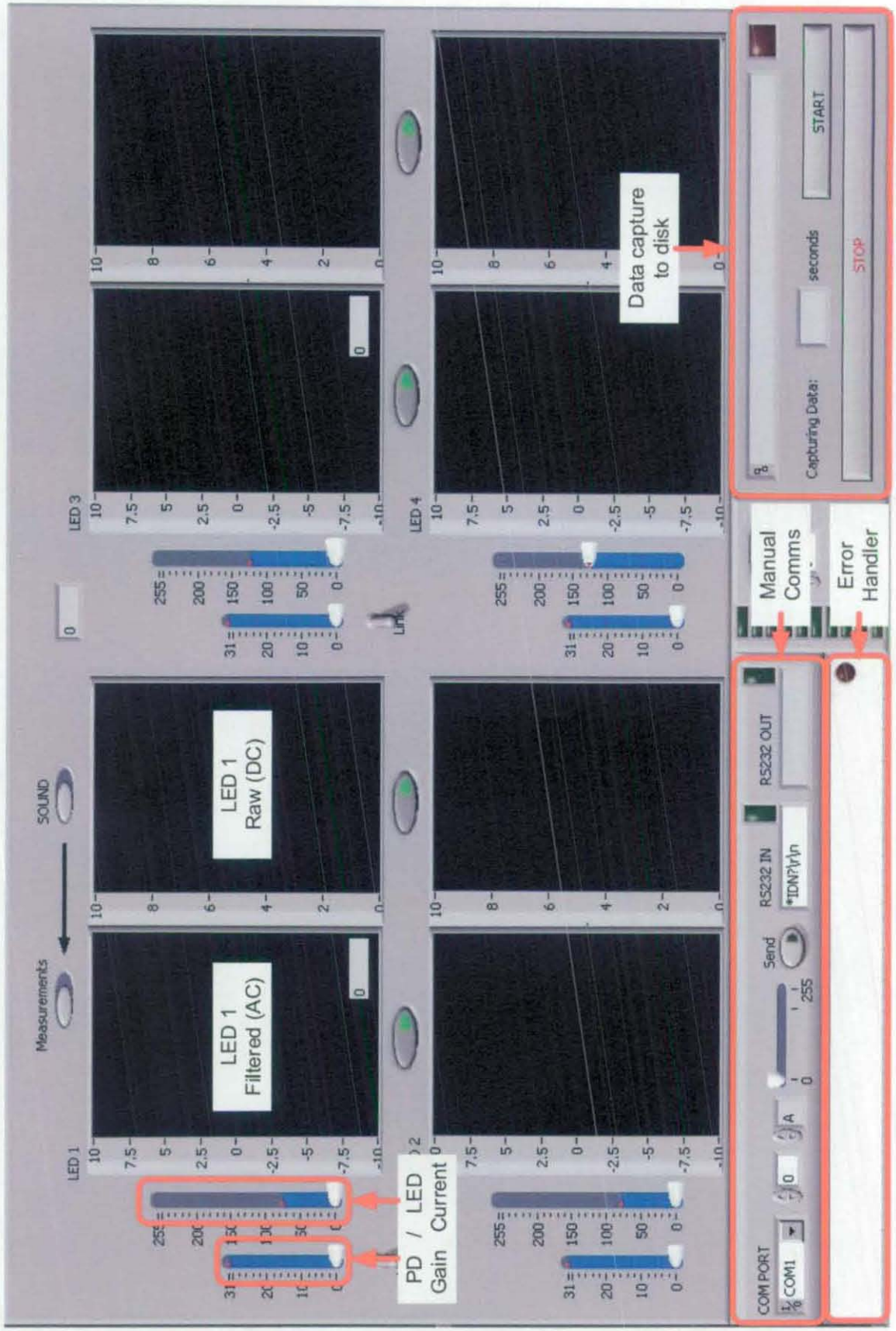

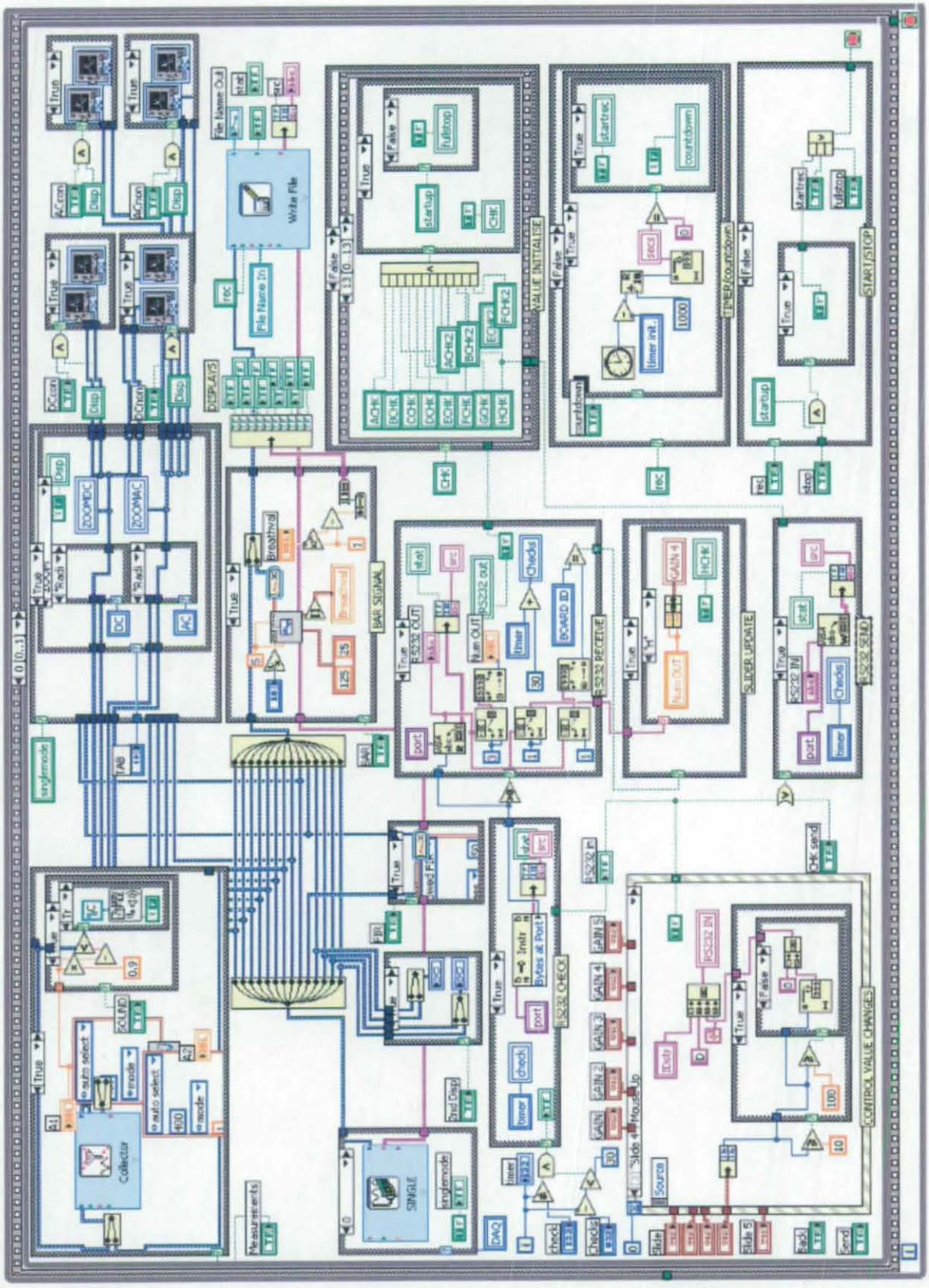
START/STOP
CONTROL VALUE CHANGES
VALUE INITIALISE
TIMER/countdown
SLIDER UPDATE
BAR SIGNAL
RS232 SEND
RS232 RECEIVE
RS232 CHECK
RS232 OUT
RS232 IN
DISPLAYS
SINGLE
Collector
Write File
File Name In
File Name Out
startstop
countdown
timer int.
Measurements
Slide Source

III. GRAPHICAL USER INTERFACE OF OPTICAD SOFTWARE

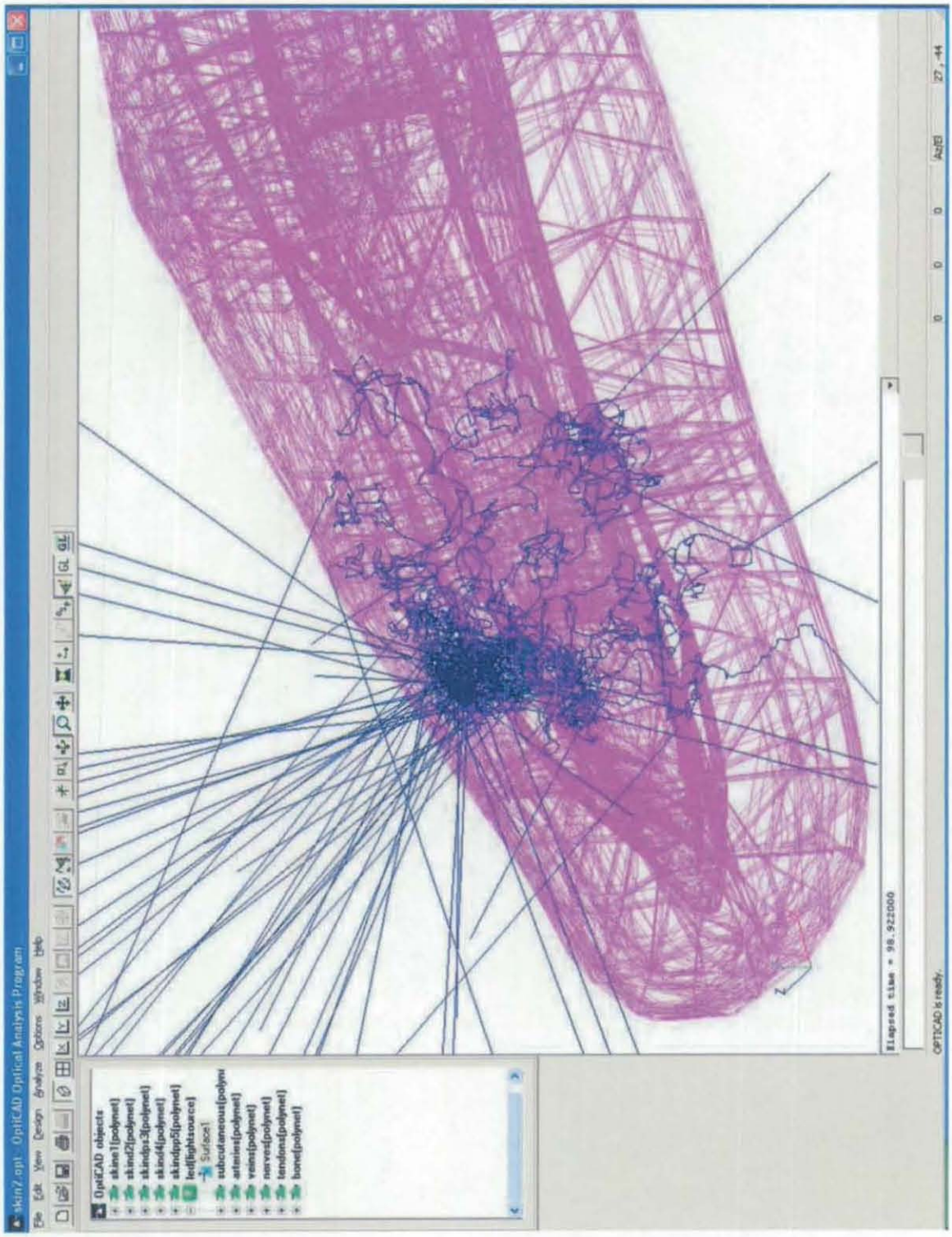

IV. DIAGRAM OF MONTE CARLO INPUT PARAMETERS